Control of Proton Beam Self-Modulation for AWAKE via Initial Beam Parameters

Master's Thesis

Samuel S. Wyler

Abstract

Plasma wakefield acceleration is a promising concept in the development of a new type of electron accelerators for high-energy physics experiments. The Advanced Wakefield Experiment AWAKE is based on this concept and has been, following the first successful proof of concept Run, under continuous and carefully planned development. In the future Run 2c, the experimental setup will consist of two plasma sources in which the highly relativistic proton driver bunch will undergo seeded self-modulation in the first plasma source, and electron acceleration will be performed in the second. Self-modulation is governed by transverse wakefields which have their origin in the self-modulation instability (SMI). At AWAKE, SMI can be controlled by either laser or electron seeding, which provides a wakefield peak that defines the phase of the fields and that of the emerging micro-bunch train. Consecutive bunches appear in the periodicity given by the plasma frequency such that they coherently drive the longitudinal wakefields. When laser seeding is applied, the part of the bunch in front of the seeding does not travel through plasma. For a successful application of laser seeding, this unmodulated front must not undergo self-modulation in the second plasma source. This front part will have a transverse bunch size of about $500\,\mu m$ when arriving at the second plasma source.

I studied in this thesis the self-modulation of proton beams of different transverse sizes. In the experiment the transverse proton beam sizes at the plasma entrance are measured by a code I developed which provides a description of the proton beam envelope. This characterisation of the proton beam is used to determine the parameter space of the numeric simulations. A detailed explanation of the code and propositions for noise reduction are given in this work.

In this thesis for the first time the self-modulation growth rate of beams with transverse sizes larger than in the baseline design will be compared. It will be demonstrated through experiment that a proton beam with a transverse size of $\sim560\,\mu m$ and a length of $\sim6.7\,cm$, focused at the plasma entrance, does not self-modulate in front of the bunch centre. This beam size corresponds, when laser seeding is applied, to the size of the unmodulated front at the second plasma source in Run 2c. These important results indicate that laser seeding could be possible in Run 2c.

Before this work, comparisons of experimental results with numeric simulations have only been carried out for beam sizes according to the baseline design. I will show that the simulations performed with a quasi-static PIC code show good qualitative agreement with the experiment when comparing the micro-bunch train structure for a larger beam after seeded self-modulation. It is therefore shown that numerical simulations remain also for larger beams an important tool to discover and understand trends and phenomena.

Additionally, I will show a previously unseen band-like radial structure that has been observed in the transverse projections of the beams. This radial structure is observed in numerical simulations after letting the bunch propagate through 10 m of plasma and is further enhanced as the beam size is increased. This could be used for future self-modulation diagnostics.

Résumé

Dans le domaine de la physique des hautes énergies, l'accélération par plasma wakefields se positionne comme un concept nouveau et innovant pour le développement des nouveaux accélérateurs d'électrons. L'expérience AWAKE (Advanced Wakefield Experiment) est basée sur ce principe et a fait l'objet d'un constant développement suivant le succès de la validation du concept. Dans le futur cycle 2c, le dispositif expérimental sera composé de deux cellules de plasma, dans lesquels le faisceau de protons hautement relativistes subira une auto-modulation dans la première cellule et les électrons seront accélérés dans la seconde. L'auto-modulation est régie par des wakefields transversaux qui trouvent leur origine dans l'instabilité d'auto-modulation (SMI). Chez AWAKE, l'instabilité d'auto-modulation peut être contrôlée par seeding d'un laser ou d'électrons. C'est ce qui permet l'obtention d'un pic de wakefield définissant la phase des champs et du train de micro-bunches émergeant. Des bunches consécutifs apparaissent à la même fréquence que le plasma, de sorte qu'elles entraînent de manière cohérente les wakefields longitudinaux. Lorsqu'un seeding par laser est appliqué, la partie du bunch située devant le seeding ne traverse pas de plasma. Pour une application réussie de seeding par laser, ce front non modulé ne doit pas subir d'auto-modulation dans la deuxième cellule de plasma. Cette partie du front aura un faisceau d'une taille transversale d'environ 500 µm en arrivant à la deuxième cellule.

Dans cette thèse seront présentées des simulations numériques et des études expérimentales des faisceaux de protons de différentes tailles transversales. Dans l'expérience, ces tailles sont mesurées et calculée par un code, écrit par l'auteur, qui fournit une description de l'enveloppe du faisceau. Les caractéristiques du faisceau de protons permettent alors d'établir les paramètres nécessaires pour les simulations numériques. Une explication détaillée du code est donnée dans ce travail, ainsi que des propositions pour la réduction du bruit de fond.

Cette thèse traitera pour la première fois de la comparaison du taux de croissance de l'auto-modulation des faisceaux de tailles transversales plus grandes que définit dans la conception de base. Il sera expérimentalement démontré qu'un faisceau de proton de taille transversale de $\sim$560 µm et une longueur de $\sim$6.7 cm, focalisé à l'entrée du plasma, ne s'auto-module pas devant le centre du faisceau. Lorsque seeding par laser est appliqué, cette taille de faisceau correspond à la taille du faisceau du front non modulé au niveau de la deuxième cellule du plasma dans le cycle 2c. Ces nouveaux résultats d'une importance non négligeable indiquent que seeding par laser pourrait être possible dans le cycle 2c.

Les simulations réalisées à l'aide d'un code PIC quasi-statique sont qualitativement en accord avec l'expérience, lorsque l'on compare, après l'auto-modulation par seeding, la structure des trains micro-bunches pour les grands faisceaux. Avant ce travail, seules des comparaisons, pour des tailles de faisceau conformes à la conception de base, avaient été

effectuées. Il a donc été démontré que les simulations numériques restent, aussi pour des faisceaux plus grands, un outil. De plus, une nouvelle structure radiale, jamais observée auparavant, a été découverte dans les projections transversales des faisceaux. Cette dernière est observée dans les simulations numériques après avoir laissé le faisceau se propager à travers $10\,\mathrm{m}$ de plasma et se trouve renforcée avec l'augmentation de la taille du faisceau. Ainsi, elle pourrait être utilisée dans de futurs diagnostics d'auto-modulation.

Acknowledgements

This Master's thesis marks the end of my graduate studies at EPFL, but not of my learning nor of my discoveries. Nevertheless, this seems to be the right moment to thank the people who have stood by me and supported me during this time.

A big thank you goes to my family who have always been very understanding during stressful periods. My mother who wanted to have the most difficult physical phenomenons explained in simple words, my father who taught me never to forget the practical despite all the theory and my sister with whom I share great mutual respect for our different paths in life.

Joanna, as always, your input has been as valuable as the time we spend together. Thank you for your support when I need it and for your patience when you need it.

The flat-sharing community in Crissier and its many residents have created many wonderful memories for me during my time as a student. Nowadays, we are all going different ways, but nevertheless I thank Gabriel and Zora for reading through my thesis, and Pierre for making the abstract comprehensible in French. Thank you Alix for your continued patience with my French. Thank you Matthias for our wonderful love-hate relationship. All those not mentioned by name, I hope you understand that this acknowledgement is already quite long for a Master's thesis.
Those that I love, know that I love them.

Thanks are also due to Prof Mike Seidel from PSI and EPFL for assessing this thesis, Dr Tatiana Pieloni, my supervisor at EPFL who helped to place me at AWAKE at my wish and Dr Edda Gschwendtner who agreed. Finally, Dr Patric Muggli, who in addition to his work as Leader of the Future Accelerators Group at the Max Planck Institute, also acted as my supervisor at CERN.

Many thanks to Dr John Farmer for many pleasant and very productive discussions at all hours of the day and night. I thank Dr Giovanni Zevi Della Porta for his patience helping me in the control room at all times while being an excellent technical experiment coordinator, Dr Livio Verra for his help with the plasma experiments, and Dr Vittorio Bencini for the straightforward collaboration in the development of the new beam optics. Also thanks to Dr Francesco Maria Velotti, Jan Pucek, Dr Eugenio Senes, Dr Michele Bergamaschi, Tatiana Nechaeva, Dr Lucas Ranc, and the whole AWAKE Collaboration as well as the SPS team.

Lausanne, the 8th of July, 2022 Samuel S. Wyler

Contents

1 Introduction

The *Advanced Wakefield Experiment* (AWAKE) is a unique electron acceleration experiment at the forefront of research. It was originally designed as a proof of concept experiment.[1, 2] These expectations were fulfilled when, in 2018, it was successfully demonstrated that a seeded self-modulated proton bunch can generate plasma wakefields able to accelerate electrons from 19 MeV to 2 GeV.[3]

Nowadays, one part of the research relates to a better understanding of the general physical phenomena that occur in the context of the experiment. The main effort, however, relates to the further development of the concept to obtain a resulting electron beam with even higher acceleration energies and higher quality, suitable for particle physics experiments.[4]

The time-line of the experiment is divided into so-called runs, each of which pursues specific scientific goals. In the current Run 2a, so-called *electron seeded self-modulation* (eSSM) is the principle focus of investigation.[5–7] The goal of Run 2b will be the demonstration of stabilisation of micro-bunches when implementing a plasma density step.[8] A big step not only in terms of leading physics but also concerning the setup is then planned for Run 2c. The existing setup, in particular the 10 m long plasma source (vapour source), is to be expanded with a second plasma source of the same length but with different properties and a second electron beam system. With this new setup, AWAKE will try to show that electron acceleration with gradients of $(0.5 \text{ to } 1)\,\text{GeV/m}$ – reaching even higher energies – and the preservation of the electron beam emittance are possible.[4, 8]

This thesis both describes the finalised tool for proton beam characterisation and presents the first of a series of results which will serve as a basis for strategic decisions in Run 2c.

The work is structured in three interconnected parts:

1. Determination of the proton beam parameters by measurements at AWAKE.

2. Numerical simulations of seeded self-modulation with various transverse sizes of the proton bunch.

3. Experimental results corresponding to the numerical simulations in the seeded case and additional results without seeding.

1.1 The Advanced Wakefield Experiment (AWAKE)

In this first section the reader shall obtain general information about AWAKE which helps to contextualise the experiment in the framework of accelerator research. A motivation and a reasoning of what makes AWAKE special will be given.

1.1.1 AWAKE as Part of the Bigger Picture

The *Large Hadron Collider* (LHC), built and operated at CERN, is currently the accelerator reaching the world's highest collision energies. In numbers, the LHC consists of a 27 km long ring equipped with 9593 magnets, of which the superconducting magnets need to be cooled down to 1.9 K to reach their superconducting state. The research and development (R&D) costs of the LHC including injectors and tests are estimated to be about 3756 MCHF.[9, 10] The power consumption of the LHC (including experiments) is about 600 GWh per year which is about half of CERN's total power consumption (1.3 TWh per year).[9, 11, 12] The presentation of these numbers intends to quantify "huge" machines in accelerator or high energy physics, and to illustrate the commitment that the construction of such machines requires from decision-makers. On the output side the LHC continues to provide scientifically ground-breaking results such as the observation of the Higgs boson in 2012, which can be seen as a flagship result that was awarded 2013 with a Nobel Prize.[13–15]

Before being injected into the LHC, hadrons run through multiple pre-accelerators. Once injected and after further acceleration in the LHC, proton energies of 6.5 TeV and a collision energy of 13 TeV were achieved in the LHC Run 2 (2015-2018).[16] While writing this thesis for the first time collision energies of 13.6 TeV have been reached.[17]

Nowadays, there are only two main accelerator types used to reach high output energies: *circular accelerators* and *linear accelerators* (LINACs). In both types either radio frequency (RF) cavities or microwave technology is used to accelerate particles. However, these techniques are physically restricted to an acceleration gradient of about 100 MeV/m.[18, 19] The energy output of a LINAC is therefore simply linearly linked to its length. Therefore, to reach higher energies larger machines are necessary.

In the case of a circular accelerator the limitations are due to another phenomenon which is much related with the above example of power consumption. The phenomenon is called *synchrotron radiation* P_{rad}, which scales as $P_{rad} \propto \frac{\gamma^4}{r^2}$.[1] Here $\gamma = \frac{E}{mc^2}$ is the Lorentz factor and r denotes the radius of the particle trajectory. In particular electrons, which are almost 2000 times lighter than protons, "suffer" under the γ^4 when following non-linear trajectories at high energies. The smaller the radius of the circle, the higher the radiation.[19]

In the case of electron or positron circular accelerators, at a certain particle energy the beam losses become higher than the maximum energy which can be provided by the acceleration structures. This limitation can be mitigated by further increasing the radii of circular machines. Nonetheless, we have seen above that pushing to larger machines is associated with massive R&D, construction and maintenance costs.

---

[1]Lecture notes "Introduction to particle accelerators" given by *Prof Mike Seidel* and *Dr Tatiana Pieloni* at EPFL, Lausanne.

The approach taken by AWAKE is of a different nature. The concept is rooted in research on alternative acceleration techniques which have stronger acceleration gradients orders of magnitude greater than $100\,\mathrm{MeV/m}$. This enables higher energies in linear machines without increasing the machine size.

The most promising concepts use plasma wakefields which create a sort of micro-cavity of the size of the plasma wavelength with strong electric field gradients. One can imagine these wakefields as waves on which the particles accelerate ("surf"). The beam creating these wakefields is called driver beam, the beam that undergoes acceleration is called witness beam. Machines with electrons as witness beam are of particular interest in this context since electrons undergo high synchrotron losses during acceleration in circular machines. Acceleration in a linear machine with higher acceleration gradients than found in today's machines are therefore key to reach higher energies. In particle physics experiments electrons are of interest because they are leptons: elementary particles, in contrast to hadrons (for example protons and neutrons) that are composed of quarks.

The proposal that plasmas can sustain very high electric fields arose in the middle of the last century.[20] A bit later in the 1970s the idea of accelerating electrons in plasma was proposed for the first time.[21]

A question is how the plasma is excited. Studies, including experiments, which use electron or laser (driver) beams have been done.[21, 22] Successful proof of concept experiments have been conducted: At SLAC in 2006, the tail of an electron beam (which acts as driver and witness beam) crossing a $85\,\mathrm{cm}$ long plasma source showed an energy gain of more than $42\,\mathrm{GeV}$. This results in an acceleration gradient of $\approx 52\,\mathrm{GV/m}$.[23] The downside of this approach is the difficulty to scale it up.[23] Also, the relative energy load compared to protons is lower and their provision as driver more problematic. Using protons would be advantageous.

AWAKE follows the proton driver approach. This means that the energy of a proton beam is transmitted through plasma wakefields to an electron beam. In 2009, the idea of a proton-driven wakefield accelerator experiment at CERN took shape.[2]

For an efficient excitation of the plasma, the driver bunches need to be of the length of the plasma wavelength.[24] This requirement cannot be fulfilled by CERN's *Super Proton Synchrotron* (SPS) which was designated to provide the proton beam to AWAKE. However, looking into plasma physics many different types of instabilities are known – one of them, the *self-modulation instability* (SMI) helps to circumvent this issue.

The self-modulation instability is crucial for AWAKE and was in the previous years the main subject of research. SMI is in fact the instability which allows the plasma bunch, initially about (6 to 12) cm long, to modulate (split) into so called micro-bunches spaced by the plasma wavelength. In this way the "too long" proton beam can be used as driver beam. As the name suggests, this modulation is governed by instability. To control this instability the short pulsed high energy laser is not only used to ionise the plasma but also provides with its front at a defined position in the bunch a sharp edge where the creation of plasma wakefield starts. This abrupt start of ionisation inside the proton (p^+) bunch leads to a seeding of self modulation, with the result of *seeded self-modulation* (SSM). The

sharp edge is called *relativistic ionisation front* (RIF).

1.1.2   Review of the General AWAKE Setup

The Advanced Wakefield Experiment is situated in the former *CERN Neutrinos to Gran Sasso* CNGS tunnel which was decommissioned in 2012.[25] After decommissioning, the final part ($\approx 80\,\mathrm{m}$) of the $\approx 810\,\mathrm{m}$ long transfer line between SPS and the future AWAKE experimental area were modified to satisfy the requirements of AWAKE. The installing the new experiment it was successfully commissioned in 2016.[26]

AWAKE is a complex experiment (Fig.1.1). It contains three different beam lines which need to be synchronised and merged before entering the vapour source (plasma source). The laser beam ionises the rubidium vapour in the vapour source into a plasma. The proton beam acts as driver beam and creates the driving wakefields which accelerate the electrons provided by the electron beam line. Since the general setup only changed minimally, parts of the following may be similar to the setup explanation of the specialisation work report written by the author.[19]
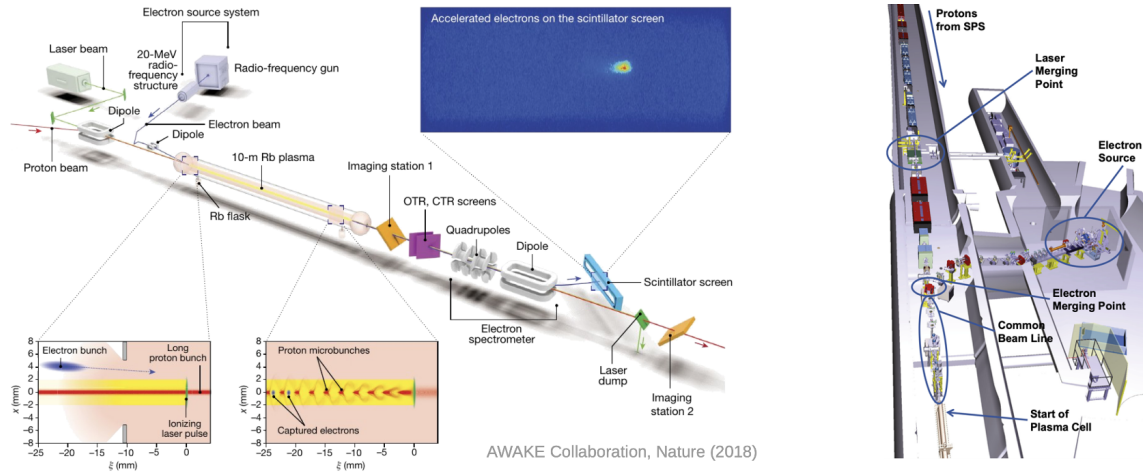
Figure 1.1: Schematic representation of current experimental setup (*lhs*). CAD drawing facing along SPS (*rhs*). Schematic drawing pointing out some important diagnostics and visualisation of the shape of the proton beam depending on its position. Images from [3, 27].

Proton Beam Line   The proton beam is the wakefield driving beam at AWAKE. The proton consist of a single bunch. This is why the word bunch and beam are often used synonymously. During a running experiment including the proton beam provided by SPS, access to the experimental area is restricted for radiation reasons. In this mode all controls and real time data analysis comes together in the *AWAKE control room* (ACC). The proton beam line and its diagnostics will be described in detail in chapter 2.

Electron Beam Line   The electron beam line is fully controlled by ACC as it is an AWAKE internal beam line. The electron source is a laser illuminated cathode. The source laser is derived from the main laser beam line which simplifies synchronisation. The electron repetition rate is set to $10\,\mathrm{Hz}$ if the trigger is not in SPS mode (no synchronisation with SPS and no proton beam). Electrons are accelerated in a 2.5 cell long RF-gun and

boosted in a 30 cell travelling wave structure with a constant field gradient of 15 MV/m. The resulting electron beam has a single bunch energy of about 20 MeV.[27, 28] The beam is shaped along the beam transfer line by quadrupoles. With the help of 10 kickers shot-to-shot position jitters are reduced to 100 μm. The transverse size of the beam when entering the plasma needs to be ≤ 250 μm.[27, 28]

Together with some diagnostic BPMs, two emittance measurement stations are placed along the beam line as well as a fast current transformer and a Faraday cup. The time-synchronisation is done with a streak camera.[27, 28]

Laser beam line   At AWAKE a Fibre/Ti:Sapphire with a wavelength of $\lambda_0 = (780\pm5)$ nm is used to provide a short high energy pulse of $\tau_0 = 120$ fs pulse length and $E_{max} = 450$ mJ. Only part of the beam is used for plasma ionisation. A part is derived and modified to illuminate the electron source, another part propagates in parallel to the main beam line, on a virtual beam (or diagnostic beam line) line for diagnostics and a final part is used as a position marker in the plasma experiments. The position of the marker is controlled by an additional so-called air transition distance. The focal size of the laser is $r_l = 1$ mm and the envelope is characterised by a Rayleigh length of $Z_r = 5$ m.[27, 29] The effectively ionised plasma has at the plasma entrance a radius of 1.5 mm and at the exit 1 mm.[30] Multiple laser beam dumps are placed along the common beam line to protect screens from the high energy beam.

Plasma Source   Also called a vapour source, the vapour source has a length of about 10 m and a diameter of 4 cm. Rubidium (Rb) can flow from two reservoirs into the vapour source where it is ionised by the high energy laser pulse. Rubidium occurs in nature as $^{85}_{37}$Rb (72 %) $^{87}_{37}$Rb (28 %); the latter is slightly radioactive. The temperature range of the Rb in the plasma source is (150 to 230) °C with a uniformity of $\delta T/T > 0.1$ %.[29]

For rubidium the first (4.177 eV) and second (27.28 eV) ionisation energies are far away from each other. The laser intensity is optimised such that it can be assumed that in the absence of a proton beam the plasma ion density is equal to the plasma electron density ($n_{ion} \simeq n_e = n_0$).[29]

At both ends of the vapour source so called expansion volumes are installed where the Rb condenses. This helps, in addition to shutter, to reduce Rb leaking. In this transition region a plasma density gradient appears; its properties influence the experiment critically.[29, 30]

Diagnostics   For imaging plasma diagnostics two image stations (IS), each consisting of a *CORE* and *HALO* camera, are available (c.f. section 2). Furthermore, two streak cameras provide time resolved images of the beams before and after the vapour source.

Data Acquisition and Trigger System   For the data acquisition (DAQ) a *PCI eXtensions for Instrumentation* Architecture, also called PXI architecture, is used. Now a transition period with a change to a BI DAQ is ongoing. All information obtained by sensors, cameras, triggers and so on is stored in compressed files of h5 architecture and written to CERN's AFS system. Later on, these files are copied to the EOS system where
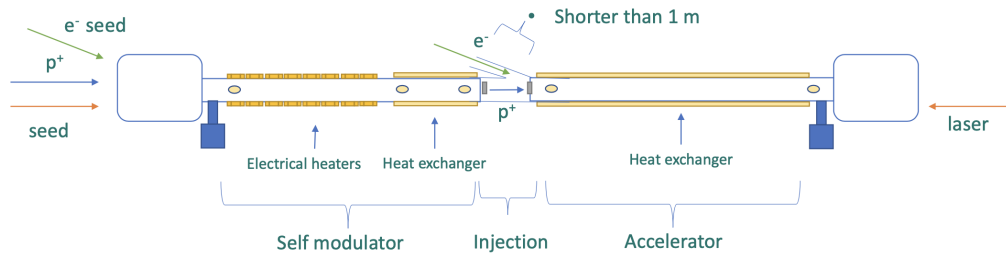
Figure 1.2: Schematic representation of experimental setup for Run 2c. Image taken from [34].

they are more easily accessed. When running in proton mode, the internal laser trigger of AWAKE is tuned to the SPS extraction trigger. From then on, all triggering at AWAKE is relative to the laser trigger system.

1.2 Physics Program of Run 2c

After Run 2a and Run 2b, Run 2c will involve the next major setup change for AWAKE. By dismantling the existing facility, space will be created for a second vapour source (plasma source) and a second electron beam line. The dismantling is planned for the years 2025/2026 and the commissioning in 2028.[8] If this run is successful, the next step is to demonstrate the scalability of the experiment before it can finally find its place in high energy physics experiments.

In this new setup, electron acceleration is performed in two plasma sources. The first plasma source (self-modulator or self-modulation stage) modulates the proton (p^+) bunch. The seeding is done either by the electron beam (studies for this are done in the current Run 2a) or a short-pulsed high-intensity laser beam which produces a relativistic ionisation front (RIF). The second plasma source is called the acceleration stage. In this stage, energy is transferred from the now-modulated p^+ bunch to the electrons that are to be accelerated. The latter are injected directly into the acceleration stage as shown in Fig.1.2. While the ionised laser beam propagates with the p^+ bunch in the first stage, it does so against the general propagation direction in the second plasma source.

The motivation for this two-stage concept lies in the problem that during evolution *self-modulation* (SM) the acceleration of electrons has been shown to be ineffective. One reason for this is effects arising when the electron bunch crosses the plasma density gradient at the entrance of the plasma source.[30, 31]

Also, and more important, it has been found that during the self-modulation the phase velocity of the wakefields is less than the speed of light.[32] Numerical simulations show however that once the self-modulation instability (SMI) reaches saturation (i.e., the micro-bunch structure is fully developed), the phase velocity approaches that of the p^+ bunch.[33] These two issues are mitigated by the use of a two-stage concept.

1.3   Motivation of this Thesis in Relation to Run 2c

In the case of RIF (laser) seeding, in the plasma source the front part of the proton bunch remains un-modulated. This is because the RIF position must be at most $(-2$ to $-1.8)\sigma_t$ in front of the bunch[2] centre if seeding is to be achieved.[35] This front-part therefore does not propagate through the plasma which was first ionised by the RIF, but through rubidium (Rb) vapour. During this propagation the transverse beam size increases from about $(180$ to $200)\,\mu m$ to about $(490$ to $540)\,\mu m$ assuming the beam parameters in Tab.2.1 (where the more focused beam diverges more at the same emittance).

The crucial question is what happens to this front-bunch part in the second plasma source (acceleration stage). Because of the reversed laser propagation direction, the front-bunch will not experience any seeding due to the RIF used to ionise the second plasma source. A possible SM would therefore have to take place through the SMI. If a modulation takes place, the resulting wakefields can disturb the following micro-bunch train, and in the worst case destroy it. In this case, the seeding in the first plasma source could be done with the electron beam (eSSM) instead of with the RIF. Therefore, the RIF could be placed further ahead of the bunch since it no longer needs to seed the self-modulation. In this case the entire bunch would travel through plasma, would undergo adiabatic focusing by the plasma and would not spread out. However, eSSM turns out to be more difficult to put into practice.

Let us return to the question of what happens to the unmodulated bunch-front in the case of RIF seeding. We know that due to the transverse magnification of the beam, the charge density decreases. From linear plasma theory we also know that the SMI (not seeded) depends on the proton bunch charge density. This has recently been confirmed experimentally also for the seeded case.[5] The smaller the charge density, the slower the evolution of the self-modulation along the propagation of the bunch but also in the bunch.

To mimic the situation of the front-bunch entering the second plasma source, a first approach is to consider the SMI behaviour of larger proton bunches in the existing experiment (Tab.1.1). In this way, the charge density is reduced – this is what is done in this work. To even better imitate the situation in the future Run 2c, the waist position of a standard beam would have to be placed about $11\,m$ upstream of the plasma entrance. In this case, at the iris not only the bunch charge density would correspond to what we expect to have in Run 2c, but also the divergence of the beam, see Tab.1.1. The bunch divergence would be larger; it has been shown in numerical simulations that a higher divergence inhibits SMI more.[3]

	Lower charge density	Larger Spread	Both
Growth rate reduction	*Demonstrated in thesis*	*Assumed*	*Assumed*

Table 1.1: Simplified situation description of the approach demonstrating RIF seeding feasibility for future Run 2c.

To characterise the transverse beam sizes of the new beams used at AWAKE, a proton

---

[2]This study used a standard beam according to the baseline design with a population of 3×10^{11} p$^+$ and a bunch length of $\sigma_t = 250\,ps$. Bunch length and population are therefore comparable to the situation in this work.

[3]Based on *private communication, July, 2022* with *Dr John Farmer* about unpubl. studies showing this.

beam characterisation code is used. The entire code was written by the author. However, its development started before this Master's thesis.

1.4   Structure of the Work and Findings

This thesis considers for the first time the unseeded self-modulation growth rate of enlarged beams of non-baseline design. The transverse beam sizes we have at hand in the experiment are ∼330 µm and ∼560 µm.[4] For the same transverse beam sizes the laser-seeded case was also considered. Numerical simulations were performed and compared with experimental results. Additionally, in the quasi-static particle-in-cell simulations transverse beam sizes up to 1000 µm were considered. In the transverse projections of these larger beams a kind of band structure was found which has not previously been observed. These results will be shown together with an analysis of the corresponding phase space after 10 m propagation through plasma.

Note that the following chapter is dedicated to the proton beam characterisation. Although this work started in the author's specialisation work semester, various optimisations and analyses were carried out during the thesis. This service work lays a foundation for a more complete description of the experiments carried out at AWAKE. It is hoped that this code will also be used in the future, thus this chapter helps to explain the code. All other chapters are entirely dedicated to new physics and the tools used to find and understand the results.

---

[4]The development of the new SPS optics needed to provide these new beams with new characteristics is from the work of *Dr Vittorio Bencini* and *Dr Francesco Maria Velotti.*

2 Proton Beam Characterisation

The *Super Proton Synchroton* (SPS) at CERN provides the proton beam to AWAKE. The SPS is also the last pre-accelerator before proton injection in the *Large Hadron Collider* (LHC). The *Proton Synchrotron* (PS), the *Proton Synchrotron Booster* (PSB) and a linear accelerator (LINAC4) are pre-accelerators to SPS. The different accelerator complexes therefore work as a chain of acceleration steps providing particles of increasing energy. The SPS works in supercycles (duration of about 1 min). AWAKE receives one to two proton extractions per cycle.

The proton beam parameters of the original 2017 baseline design of AWAKE are presented in Tab.2.1. Since then, some modifications were made, meaning that the bunch length can nowadays be compressed to about half of the original length. It is important to note that experiments are often carried out within a certain parameter range.

Parameter	Unit	Baseline 2017
Particles per bunch	$1 \times 10^{11}\,\mathrm{p}^+$	3
Charge per bunch	nC	48.07
Momentum	GeV/c	400
Momentum spread (1σ)	GeV/c	± 0.035
Lorentz factor γ		426.3
Bunch length (1σ)	cm	12
Bunch duration (1σ)	ps	400
Transverse bunch size at waist (1σ)	µm	200 ± 20
β function at waist	m	4.9
Norm. emittance	mm mrad	3.5

Table 2.1: Baseline proton beam parameters from 2017 of a baseline design beam for electron acceleration.[26] Note that in spring 2022 a compressed bunch of ∼7 cm length was used.

2.1 Introduction to the Proton Beam Characterisation

The proton beam characterisation is a project that was started during the author's specialisation work in the previous semester.[19] For this purpose, a PYTHON code was developed which characterises the proton beam based on transverse size measurements at different cameras along a distance of about 25 m. The determined parameters are a cornerstone for this thesis.

During the work for this thesis, the code was refined and further automated. For example, certain results are now published live in the *AWAKE control room* (ACC). Possible systematic error sources were identified, a short analysis of the available screens

was performed, filtering/data-smoothing methods were analysed and position and size jitter results are also made available as output. In addition, the ability to fit saturated images has been developed. At the same time, it turned out that due to the real beam shape (which is not perfectly Gaussian), this cannot be used.

The proton beam characterisation is done on a daily basis to verify the proton beam provided by SPS. This is especially of importance for this thesis where beams provided by new SPS optics are used for plasma experiments. These new optics enable SPS to provide new, transversely larger proton beams, for which, however, there have been no studies up to this work. A previous study was carried out for the standard proton beam, but its analytical approach differs fundamentally from our method.[36]

The proton beam (bunch) parameters we are interested in are the *waist position*[1] $(z_{x,0}, z_{y,0})$, the *beam size at the waist* $(\sigma_{x,0}, \sigma_{y,0})$ and the *normalised emittance* $(\epsilon_{n,x}, \epsilon_{n,y})$. Knowing that in all previous accelerators lower order magnets act mainly in the x or y – plane it is natural to consider only these two planes as a first simplification. Note that a beam with a tilted ellipse-like shape would be ill-represented by this approach. The advantage of this approach is the simplicity and clean separation along two axes. Further parameters can be derived from the three mentioned above: of interest are the β function at the waist $(\beta_{x,0}, \beta_{y,0})$, the beam size at the plasma entrance $(\sigma_{x,i}, \sigma_{y,i})$ and the beam divergence $(\varsigma_x, \varsigma_y)$.

After passing the last magnet of the transfer line, the proton beam travels in a drift space at AWAKE (as long as no plasma experiments are carried out). Here the beam can be described by the *envelope equation*, which is a hyperbola:

$$\sigma_x(z) = \sqrt{(\sigma_{x,0})^2 + \frac{\epsilon_x^2}{\sigma_{x,0}^2}(z - z_{x,0})^2} \tag{2.1}$$

Note that an equivalent equation is valid in the y direction.
These equations each have three unknowns, therefore, knowing the (transverse) beam size σ_x at three independent positions let us find the three unknowns exactly. The requirement of independence comes from the fact that under the condition of $(z - z_0)^2 >> \frac{\sigma_0^4}{\epsilon_n^2}$, Eq.(2.1) can be written as linear equation:

$$\sigma(z) \approx \frac{\epsilon}{\sigma_0}(z - z_0) \tag{2.2}$$

where the x-axis index has been omitted. Therefore, two beam sizes measured far enough away from the waist z_0 tend to lay on a straight line. In accelerator physics, the above-mentioned condition for linearity is reflected in the β function at the waist, which is defined as:

$$\beta_0 = \sigma_0^2/\epsilon \tag{2.3}$$

To improve the fitting process we define in the code the beam divergence $(\varsigma_x, \varsigma_y)$ as $\varsigma = \epsilon/\sigma_0$ and substitute ς into Eq.(2.1) which has the advantage that the second term

---

[1]Depending on the author the waist position is also often called the focal point.

under the root only contains two instead of three unknown parameters:

$$\sigma(z) = \sqrt{\sigma_0^2 + \varsigma^2(z - z_0)^2} \qquad (2.4)$$

Finally, note that the normalised emittance (which we are interested in) is not the same as the standard emittance in Eq.(2.1). The emittance of a beam, except for a few exceptions, does not change while the beam travels in the synchrotron as long as there is no longitudinal acceleration. However, the value of the standard emittance decreases when the beam is accelerated, since it gains momentum in the longitudinal direction. This is why the emittance is normalised by multiplying it with the relativistic gamma factor γ and the relativistic beta β_{rel} of the beam:

$$\epsilon_n = \beta_{rel}\gamma\epsilon \qquad (2.5)$$

Corrigendum In Eq.(2.1) the beam dispersion is not taken into account. The presented equation describes only the betatron (transverse) beam size. The dispersive share is only equals to zero at the beam waist and from there increases linearly with the position z. From MADX simulations[2] it is known that for the baseline design beam (target transverse size of $200\,\mu m$) the dispersive part of the beam size is in both planes small, even negligible. In the stronger affected x-direction the dispersion is responsible $12\,m$ after the waist position for about $80\,\mu m$ of the beam size. However, for the new $560\,\mu m$ large beam the dispersive part makes about $370\,\mu m$ of the total beam size at the same position (again provided by MADX simulations). Along the y-axis the dispersion remains negligible for all considered beam. Correcting the dispersion along the x-axis influences the values found for the normalised emittance and the β function at the waist. An overview over the dispersion of the three beams is given in the appendix in Fig.A.4.

The dispersion remains unimplemented in the proton beam characterisation code. However, it only takes a few steps to subtract the dispersive part from the measured beam sizes at the cameras. The dispersion cannot be measured by the setup presented in this work, therefore, this information needs to be provided from simulations. What in consequence leads to a mixing of MADX simulations and experiment.

2.2   Review of the Technical Setup

Multiple diagnostics instruments such as *Beam Position Monitors* (BPMs) or *Beam Loss Monitors* (BLMs) are installed at or in the vicinity of AWAKE.[26] Since we are interested in the determination of the transverse beam (bunch) size, we focus here on imaging diagnostics. *Beam Observation TVs* (BTVs) are used to determine the transverse projections of the proton bunch. They fall under the category of invasive beam size diagnostics, since they capture the light emitted by screens when the proton beam crosses these screens. In addition to the BTVs, two so-called *Image Stations* IS1 and IS2 are available. The camera as well as the data acquisition system is constantly under modification. Here we focus on the latest setup. In any case, references [19, 26, 37, 38] may be of interest to the reader to

---

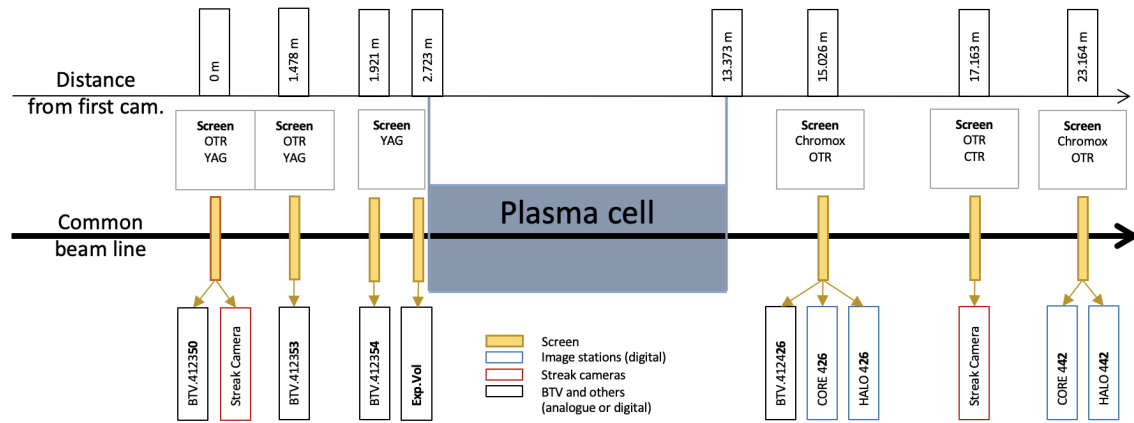[2]Performed and provided by *Dr Vittorio Bencini.*

Figure 2.1: Schematic overview of the cameras implemented in the code of the p^+ characterisation. The positions of the streak cameras are shown in red.

better understand the original setup.

2.2.1 Cameras and Calibration

To better understand the camera naming, it is necessary to go back to the beginnings of AWAKE.[37, 38] The BTVs were originally all equipped with standardised analogue cameras, while the image stations (IS) are AWAKE specific and were equipped with digital cameras from the beginning.

For the current setup, however, BTV50 was upgraded to a digital camera with a better resolution.

IS1 is also a special case. It shares both a screen and filter choice with BTV426. This means that when using an OTR screen, only one of the two cameras can be used optimally. Ideally, this is IS1 because of its better resolution.

The two image stations each consist of a CORE and a HALO camera, whereby only the CORE cameras are used for beam characterisation. Consider Fig.2.1 to better understand the positioning of these cameras. With the developed code we can analyse the beam sizes at seven camera systems simultaneously. For different reasons only three were used during the first run of 2022, and four during the second. Consider Tab.2.2 to get an overview.

For most cameras, the pixel-to-metric calibration was checked (sometimes several times) and renewed when cameras were replaced. An incorrect calibration value is the most direct source of potential systematic error.

For the calibration, a screen illumination can be switched on, which makes reference-engravings on the CHROMOX and YAG screens visible. These lines, which extend horizontally and vertically over a large area of the screen, have well-defined distances between each other. The calibration is found by counting the number of pixels between them. The screen lies at an angle of 45° to the transverse plane of the proton beam propagation direction, so it is impossible to obtain a uniformly focused image. Along one axis, the pixel calibration remains ambiguous. To take this into account, the calibration is averaged over the largest possible range. In the case of IS2, the difference between

the counted pixels between the two extremities is for example about 2.6 %. This effect is negligible for us, especially since the beam is mostly centred. The values listed in Tab.2.2 are those determined by the author for BTV50 and 26, as well as for IS1 and IS2.

The camera BTV53 is another special case: on the one hand it is the only camera always in use that is not digital and has the smallest number of pixels. On the other hand, (precisely because of the small number of pixels) an additional magnification optic is installed. This means that the engravings are no longer visible, and no verification can be done. This is especially problematic because BTV53 and BTV50 are very close together in a highly non-linear part of the beam envelope and thus influence the beam envelope much more than IS2, for example.

Camera	Pos z [m]	Px	Calib. [µm/px]	Screens	Used
BTV.412**350**	0 m	1920×1200	14.18, 14.35	OTR/YAG	yes
BTV.412**353**	1.478 m	400×300	28.9, 30.6	OTR/YAG	yes
BTV.412**354**	1.921 m	1280×1024	37.0, 37.0	YAG	no
ExpVol	2.68325 m	1920×1200	33.0, 33.0	YAG	no
BTV.412**426**	15.026 m	400×300	113.2, 125.98	OTR/Chromox	no
IS1 Core	15.026 m	1200×1600	44.98, 45.89	OTR/Chromox	yes
IS2 Core	23.164 m	1600×1200	41.1, 40.35	OTR/Chromox	yes.

Table 2.2: Cameras implemented in the beam characterisation code. Note that the first camera acts as origin for the position z.

2.2.2 Screens

Thin metallic screens are a necessary tool to image the transverse profile of particle beams. The beam crosses the screen which leads to emission of photons. Depending on the screen type, this emission is based on different physical processes.

Screens used at AWAKE can be roughly put into two categories: *Scintillator* screens and *Optical Transition Radiation* (OTR) screens. The latter have the advantage that they emit light instantaneously and in a delta-like peak. This is a key property for their use in the time-resolved streak camera system. On the downside, for a normal camera the trigger delay needs to be highly precise. Since the light pulse is so short it is not possible to use the exposure time to prevent saturation of the camera sensor. Consequently, well matching filters are absolutely necessary. Scintillator screens in comparison have a much longer photon emission time-span.[3] Also, the light yield is higher. The underlying physical processes are explained in the next paragraphs.

Optical Transition Radiation OTR screens at AWAKE are 0.3 mm thick silver coated silicon plates (SiAg). The concept of OTR was first presented in 1945.[39] It is to a certain extent related to Cherenkov radiation. OTR however occurs when a charged particle passes through an inhomogeneous media. A possibility for a detailed explanation is to use the *image-charge method* (also called *method of images*) which originates from electrostatics.[40]

Let q be a charge (for example a proton) moving towards the screen which could be

---

[3]Lecture notes "Particle detection" (PHYS-440) given by *Guido Haefeli* at EPFL, Lausanne.

seen as a conductive plane, and which is the reason for inhomogeneity. Then, by positioning an image charge $-q$ at the correct position (in our case mirrored on other side of the plane) the plane can be replaced by this charge $-q$. If this is done correctly, the electric field on the side of the plane where q is remains the same. Obviously, we can now let both charges move towards each other as long as their respective distances to the now imaginary plane remain equal. At some point these two charges will meet, (i.e., when the screen is hit) and from our point of view the charges seem to be annihilated. This leads to the emitted transition radiation.

Indeed, this is a simplification of the actual physical processes taking place. Nevertheless, it gives a feeling where OTR is coming from and it also is used by Ginzburg who wrote the original paper about transition radiation.[41, 42] Furthermore OTR is not radiated uniformly but has an angular distribution which is cone-like with an angle between normal vector and cone of $\theta \approx 2\gamma$, where gamma is the Lorentz factor of the particle.

Scintillator Light   Scintillator light is emitted by $1\,\mathrm{mm}$ thick CHROMOX (Al_2O_3:CrO_2) screens at AWAKE. It is defined as the light that is emitted when ionising radiation pushes the electrons of the screen material into an excited state. This means electrons are shifted from their ground state in the valence band into the conduction band. When falling back to the ground state they emit photons in the visible spectrum. It has been found that the rise time τ_r and decay time τ_d both follow exponential functions. Therefore, the photon emission I can be written as $I(t) = I_0 \left(e^{\frac{-t}{\tau_d}} - e^{\frac{-t}{\tau_r}} \right)$.[43] The decay time τ_r is actually long enough that camera saturation can be avoided by choosing adequate delay and exposure times (of the order of tenth of micro seconds) in the camera setup at AWAKE.

On the downside we have shown that the measured beam size of a p^+ bunch measured by CHROMOX screens is larger than by OTR. Indeed it was already shown in [44] that a bigger beam size measurement is expected. But our actual measured sizes exceed these values. The poor resolution of the CHROMOX screens might be the reason for this. For this reason, CHROMOX screens are not used for beam size measurements in this sub-project.

A recently installed new screen type is a Yttrium-Aluminium-Garnet (YAG) screen. This new scintillator screen type should have a more similar resolution to OTR while benefiting from a higher light yield.[42] However, this higher yield is problematic – the screen itself saturates when used with protons and is not suitable for use.

2.2.3   Resolution

The camera resolution is easy to determine compared to the resolution of the screens. As previously discussed in [45], the resolution is given by the size of two pixels. This approach can be justified by the fact that we measure a distance, so it makes sense to define the smallest measurable distance separating two points as the resolution. These are two pixels.

Certain considerations about the estimated (screen) resolution were made in [37, 45] and it is not clear to what extent this is still valid. In 2017, in [44] the screen resolution was considered separately from the camera resolution. However, conclusive studies on today's screen resolutions are lacking.

Only OTR type screens are used for the beam characterisation. The screen resolution is therefore the same at all measurement stations. Since the camera resolution changes from camera to camera, the measured beam size is corrected according to the engineering formula $\sigma_{corr} = \sqrt{(\sigma_{meas}^2 - p^2)}$, where p is the pixel size.[4]

2.2.4   Filters

After new filters were installed in Run1 2022 specifically for beam characterisation, BTV50, 53, 26 and IS1 have filters that allow the transmission of $10\,\%$, $1\,\%$ or $0.1\,\%$ of light (OD1, OD2 and OD3). For IS2, instead of an OD1, it has an OD4 filter.

It should also be noted that both image stations have a light-splitter installed which distributes the emitted photons to the CORE and HALO cameras. This means that the CORE cameras we use receive only $8\,\%$ of the total light, while the HALO cameras receive $92\,\%$.[46] At both stations in general no filter is used for measurements because of this signal weakness. The weakest signal is found at the CORE camera of IS2.

To obtain the best possible signal when using OTR light, a precisely matched filter is vital. This is because the signal duration is much shorter than the smallest possible exposure time of the cameras used.

If the beam characterisation results are to be improved without resorting to sophisticated methods as Hafych *et al.* did in [36], the filter gradations have to be refined. Another solution could be to evaluate an enlarged filter wheel with gradations from OD0.2 to OD0.4 with 10-15 slots. This should also be feasible from a cost-benefit point of view.

2.3   Review of the Code

The development of the Python code used for the proton beam characterisation started during the specialisation work prior to this thesis. During the thesis it has been refined, and some functionalities have been added. The entire code has been written by the author. It was a conscious choice to develop a code simpler in its approach and faster in its execution than it was done by Hafych *et al.* Such a code is easier to adapt to the changing conditions at AWAKE, it can be executed on a daily base and provide almost in real-time results.

The code consists of two classes: one called EVENT and a second EVENT_SET which contain the EVENTS. Already at an early stage of the development, it became evident that one single event does not provide a clean enough signal to determine the beam parameters from it. This is why EVENT_SET exists, in which the beam parameters are found with a statistical approach. This works under the assumption that for given settings the shot-to-shot stability is high enough that individual events can be compared. The class EVENT_SET processes events in the following way:

1. The events stored in h5 data format are read from EOS [47] and excluded if they are corrupted. The user can choose for which cameras data should be loaded for

---

[4]Based on *private communication, spring 2022* with *Dr John Farmer* and *Dr Giovanni Zevi Della Porta.*

analysis. Since the AWAKE setup is constantly evolving, the setup in which the data was acquired must also be defined (version 0 for 2021 runs, version 1 for 2022 runs). Furthermore, it can be specified for each camera if the BI or PXI data acquisition system is in use. After loading the data an initial noise reduction treatment takes place; the images are subtracted by the mean of some no-beam images. This reduces hot-pixel errors. In addition to the raw camera images, meta-data of the camera systems setup is acquired.

2. In a next step the "usefulness" of all loaded events is tested, meaning, if the cameras were able to catch the p^+ bunch. This is done by taking the standard deviation of the images and comparing them to a defined threshold. So-called empty events are excluded.

3. The region of interest is found through filtering out single hot-pixels that arise from secondary particles, by pre-cropping and applying a 2D Gaussian convolution to all images. Then the centre of the bunch can be determined by taking the pixel with the highest count. Note that convolution is used for this step only; in later stages the centred and cropped version of the original image is used. Finally, the pixels are converted to the metric units.

4. After cropping the images, another background noise reduction takes place. The mean pixel count of all pixels laying outside the cropped region is calculated for each camera and subtracted from the images. This seems to be the most efficient method of noise reduction, without using a statistically sophisticated noise treatment. The origin of the background noise is explained in section 2.5.1.

5. Now the 2D images are ready to be converted into 1D arrays along the x and y axes. By default, a projection of and a cut along the two axes are taken. If some of the centre pixels have been saturated the user can choose to ignore these pixels. The applicability of this is discussed in section 2.5.2). Having non-saturated images at hand it is in most cases sensible to use the projection instead of cuts through the centre to increase the signal-to-noise ratio. However, both options are available.

6. In the next step a Gaussian is fit to the signal for each event along both axes (c.f. section B.2). For the fitting, PYTHON's SCIPY curve fit method is used with initial parameters as described in section B.2. This method uses the Levenberg-Marquardt algorithm to do a non-linear least-squares fitting. The maximum number of cycles is enlarged to 80,000. Especially in the case of low signal-to-noise ratio, it can be helpful to increase the tolerance of the sum of squares to stop the algorithm before overfitting, as this would fit the noise.

7. The user can now choose which cameras should be used to fit the envelope; at least three are necessary. Again, the previously mentioned curve fit method is applied to fit Eq.(2.4). We set as initial parameters the baseline parameters. The maximum number of cycles is again enlarged to 80,000. First of all, the envelope equation is fit to each individual event – here the error on the beam size found during the Gaussian fitting is given as sigma (inverse of the weight) to the curve fit method. However, we are most interested in the average parameters of the event set. For this the average of the beam sizes at each camera is taken and the envelope is fit to these values. In

this case the sigma of each average beam size is given by the standard deviation of the set of beam sizes of each camera that has been averaged.

The reader may agree this simple approach is easier to understand mathematically. The beam size, found by fitting a Gaussian curve of event i at camera j along axis k can be denoted as $\sigma_{i,j,k}$. The corresponding error (standard deviation of the parameter $\sigma_{i,j,k}$) is called $\sigma_{i,j,k}^{err}$. Then:

- **For the individual envelope parameters:** Let $M_{i,k}(\sigma_{i,1,k}, \ldots, \sigma_{i,n,k})$ be the curve fit method which finds the beam parameters of an individual event i given n cameras. Here the error associated with each $\sigma_{i,j,k}$ is obviously given by $\sigma_{i,j,k}^{err}$.

- **For the average envelope parameters:** Let the average beam size of camera j along axis k and its corresponding error be:

$$\sigma_{j,k} = \frac{1}{m} \sum_{i=1}^{m} \sigma_{i,j,k}$$

$$\sigma_{j,k}^{err} = \sqrt{\frac{1}{m} \sum_{i=1}^{m} (\sigma_{i,j,k} - \sigma_{j,k})^2} \tag{2.6}$$

  where m denotes the number of events. Then let $M_k(\sigma_{1,k}, \ldots, \sigma_{n,k})$ be the curve fit method with corresponding curve fit sigmas/weights $\sigma_{j,k}^{err}$.

  Other approaches have been tested, for example taking the degree of saturation inversely as weight or defining $\sigma_{j,k}^{err} = \frac{1}{m} \sum_{i=1}^{m} \sigma_{i,j,k}^{err}$

8. After having performed both fits, events with too a large fitting error on the parameters of interest are excluded. It is also possible to exclude events providing multiple non-physical parameters, for example beam sizes that are too small.

9. In a final step the results are prepared. The following outputs are available:

   - A plot of the region of interest of each camera with noise subtracted.

   - A plot of each camera along the x and y axes showing the projection or cut through the centre of the region of interest with the corresponding Gaussian curve fit to the signal.

   - A plot showing the beam size measured by each camera in sequential events in the xy – plane.

   - A plot showing the beam position and size jitter from event to event measured by each camera in a xy – plane with its origin at the average beam position. The points are sequentially colour-coded to identify eventual beam steering.

   - A plot showing the average beam envelope Eq.(2.4) along x and y over the distance of interest. The individual envelopes are shown as semi-transparent lines. Furthermore, positions of the cameras and their averaged beam size measurements are shown on the same plot, see Fig.2.2.

   - A summary plot showing the individual and average results of the beam size, β function, emittance and waist position.

   - A *.txt file with all above numerical results as well as some meta data.

Cross-Fitting In addition to the error provided by default by the PYTHON curve-fitting, a method that we call cross-fitting has been introduced to further quantify errors. The aim is to fit envelopes on non-average based inputs for the first three available cameras. Six more curve fittings are performed; each time the average beam size of one of the three cameras is summed with the positive or negative value of its standard deviation and then taken as input. The extreme maximum and minimum envelope values give the shaded area on the envelope plots. In addition, a second error estimate of beam size at waist, divergence and waist position is available.

2.3.1 Additional Features

In addition to the code structure discussed above, some further noise reduction methods have been implemented. However, with the time available for this (side) project a physical justification is hard to give and would spread into the domain of signal processing. Nevertheless, some general considerations will be presented here:

Savitzky-Golay Filter

In contrast to a 2D Gaussian convolution, which was used to find the bunch centre, the *Savitzky-Golay* S-G filter acts on the already projected profile. Let us have a closer look at what a S-G filter is doing since it seems to be mainly famous as signal smoothing method in chemistry but not in other domains – although the original paper was published by Savitzky and Golay in 1964.[48]

Let x_i with $i = 1, \ldots, n$ be a sequence of samples we would like to smooth. Furthermore, N is the order of the filter and $M = 2m + 1$ its window length. Then the S-G filter tries to fit with the least-square method a polynomial p of order N over a window of M points centred at $i = 0$ to the sample points x_i. The result of the centre of the window refers to the new smoothed sample $\tilde{x}_i$.

A general polynomial of order N can be written as:

$$p(i) = \sum_{k=0}^{N} a_k i^k \tag{2.7}$$

The optimal coefficients of this polynomial are found by minimising:

$$
\begin{aligned}
LS(N) &= \sum_{i=-M}^{M} \left(p(i) - x_i \right)^2 \\
&= \sum_{i=-M}^{M} \left(\sum_{k=0}^{N} a_k i^k - x_i \right)^2
\end{aligned}
\tag{2.8}
$$

Finally:

$$\tilde{x}_i = p(0) = a_0 \tag{2.9}$$

The filter window and therefore the centre point which is smoothed can now be shifted through all sample points. The borders remain either untreated, are ignored, or some other

treatment is applied. It can be shown that the same output can be found by applying a suitable discrete convolution.[49] Furthermore the S-G filter is equal to a moving average for $N = 0$ and $M = 3$. S-G filters are often preferred to others since they tend to preserve the width and height of peaks.[49] They act as low-pass filters without passing to Fourier space, they are therefore advantageous on non-periodic signals as we have one at hand.

Application to the case at hand The challenge when applying S-G filters is to chose an appropriate order and window length. To approximate the Gaussian curve at hand the bigger the filter window is, the bigger the order of the polynomial p needs to be. However, we want a sort of low-pass filter with high frequency denoising capacities. It is therefore sufficient to choose a low order, and a low window size of just a fraction of 1σ. Although the denoising capacities of S-G filters are very satisfactory, we need to have a high trust in the ability of the filter to maintain the σ of the Gaussian. We were neither able to find literature that could offer a clue, nor to find a rule and mathematical explanation based on which order and window size could be defined reliably enough. In the end the S-G is efficient but the σ depends too much on the chosen filter window for it to be applied.

Other Noise Reduction Methods during Post-processing

Two other methods[5] tested but not implemented are the following; convolution of two events and averaging of the projection of multiple events.

The first approach is computationally unfavourable but leads to very strong noise reduction. Strong boundary artefacts occur. The best results were achieved with a 2D convolution. The standard deviation found deviates from the expected theoretical value.

The second approach is similar to the post-processing applied to streak camera images of seeded micro-bunch trains. To avoid artificial enlargement of the beam size, the individual projections must be exactly aligned. This approach was also not pursued further for time reasons, but is considered the most promising.

2.4 Results

Up to this year a beam with one single transverse proton beam size has been used at AWAKE. Other beam parameters such as the bunch length (which cannot be determined by the tool presented here) or the beam population are subjects of changes inside a parameter range. The normalised emittance should in simplified theory not be affected by the beam optics and p^+ population. However, it has been shown in [36] and in the specialisation work of the author prior to this thesis [19] that a correlation between bunch population and beam size as well as between population and normalised emittance exist. Statistically, a larger population allows both parameters to increase.

Here the parameters of a standard beam – meaning a transverse beam size of about $200\,\mu\text{m}$ – and of two non-standard beams shall be established ($\sim330\,\mu\text{m}$ and $\sim560\,\mu\text{m}$).[6]

---

[5]Idea arisen after productive *private communication, May 2022* with *Matthias Minder*.

[6]The development of the new SPS optics needed to provide these new beams with new characteristics is from the work of *Dr Vittorio Bencini* and *Dr Francesco Maria Velotti*.

Parameter	Unit	200 µm	330 µm	560 µm	560 µm
Date	dd.mm	08.06	11.5	16.6	19.6
Numbers of events	#	51	12	15	14
Particles per bunch	$1 \times 10^{11}\,\mathrm{p}^+$	(2.8 ± 0.2)[7]	(2.83 ± 0.04)	(2.0 ± 0.2)[7]	(2.86 ± 0.03)
Charge per bunch	nC	(44.9 ± 3.3)	(45.3 ± 0.7)	(32.0 ± 3.3)	(45.8 ± 0.5)
Trans. size at waist $\sigma_{x,0}$	µm	(145 ± 40)	(330 ± 50)	(461 ± 20)	(494 ± 10)
Trans. size at waist $\sigma_{y,0}$	µm	(145 ± 40)	(315 ± 40)	(540 ± 20)	(558 ± 20)
Trans. size at iris $\sigma_{x,i}$	µm	(145 ± 40)	(332 ± 40)	(448 ± 10)	(495 ± 10)
Trans. size at iris $\sigma_{y,i}$	µm	(145 ± 30)	(325 ± 30)	(540 ± 20)	(590 ± 10)
Trans. divergence ς_x	rad/100	(4.0 ± 0.4)	(4.4 ± 0.9)	(5.5 ± 0.7)	(4.1 ± 0.5)
Trans. divergence ς_y	rad/100	(3.8 ± 0.3)	(2.9 ± 1.0)	(6.0 ± 0.7)	(4.0 ± 0.7)
Norm. emittance $\epsilon_{n,x}$	mm mrad	(2.5 ± 0.6)	(6.2 ± 0.8)	(10.4 ± 0.4)	(8.7 ± 0.1)
Norm. emittance $\epsilon_{n,y}$	mm mrad	(2.4 ± 0.5)	(3.8 ± 0.5)	(13.9 ± 0.4)	(9.5 ± 0.2)
β function at waist $\beta_{x,0}$	m	(3.6 ± 0.8)	(7.5 ± 1.0)	(8.0 ± 0.4)	(11.9 ± 0.2)
β function at waist $\beta_{y,0}$	m	(3.8 ± 0.8)	(11.0 ± 1.3)	(9.0 ± 0.3)	(14.0 ± 0.4)
Waist position $z_{x,0}$	m	(0.1 ± 0.1)	(0.8 ± 2.1)	(1.5 ± 0.9)	(-0.7 ± 0.7)
Waist position $z_{y,0}$	m	(0.2 ± 0.9)	(2.8 ± 2.3)	(0.0 ± 0.8)	(-4.9 ± 2.3)
Trans. size x BTV50	µm	(184 ± 4)	(365 ± 3)	(498 ± 5)	(501 ± 2)
Trans. size y BTV50	µm	(184 ± 4)	(352 ± 2)	(565 ± 6)	(565 ± 5)
Trans. size x BTV53	µm	(144 ± 20)	(342 ± 20)	(466 ± 6)	(494 ± 4)
Trans. size y BTV53	µm	(145 ± 20)	(336 ± 20)	(545 ± 7)	(576 ± 5)
Trans. size x IS1	µm	(530 ± 30)	(603 ± 30)	(743 ± 90)	(787 ± 70)
Trans. size y IS1	µm	(498 ± 20)	(417 ± 30)	(915 ± 80)	(941 ± 90)
Trans. size x IS2	µm	(735 ± 80)	n/a	n/a	(898 ± 130)
Trans. size y IS2	µm	(737 ± 60)	n/a	n/a	(1080 ± 140)
RMS pos. jitter x BTV50	µm	33.74	n/a	70.25	n/a
RMS pos. jitter y BTV50	µm	3.26	n/a	5.77	n/a
RMS pos. jitter x BTV53	µm	37.77	n/a	85.71	n/a
RMS pos. jitter y BTV53	µm	14.76	n/a	9.49	n/a
RMS pos. jitter x IS1	µm	62.54	n/a	202.94	n/a
RMS pos. jitter y IS1	µm	20.17	n/a	68.04	n/a
RMS pos. jitter x IS2	µm	117.43	n/a	n/a	n/a
RMS pos. jitter y IS2	µm	55.47	n/a	n/a	n/a

Table 2.3: Proton beam characterisation. Note that for all image station (IS) measurements the core cameras have been used. Where no jitter is provided, beam steering was executed during the measurement.

Corrigendum   In Tab.2.3 it is shown that for the 560 µm beam a normalised emittance of about 9 mm mrad is measured. Considering SPS where the proton beam is accelerated it is to say that this is a non-physical result. As mentioned before the dispersive part of the beam envelope is ignored. By subtracting the dispersion from the measured beam size before fitting the envelope equation the calculated normalised emittance would shrink. However, only the x-axis can be corrected in that way, since dispersion in y remains small. This would adjust the emittance value for the 330 µm beam in Tab.2.3. For the 560 µm beam the normalised emittance values are too high along both axes and correcting the dispersion wouldn't give a full explanation of the high norm. emittance measurements.

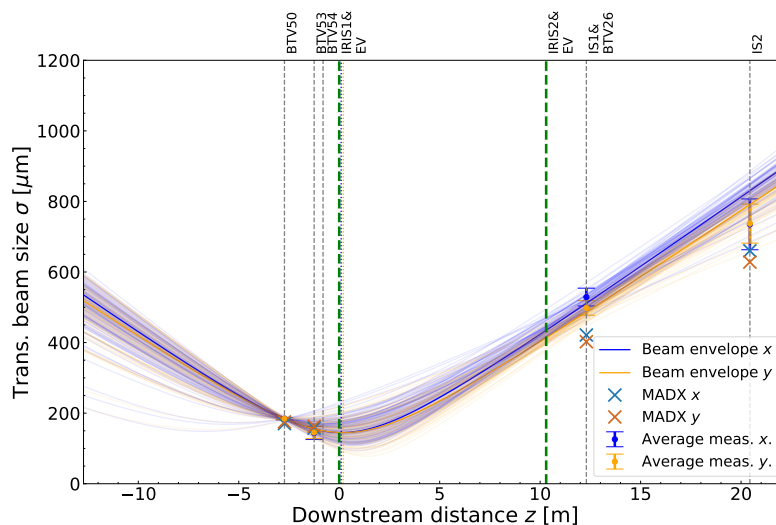### 2.4.1   Beam of 200 µm Transverse Size at Plasma Entrance

Figure 2.2: Transverse envelope of a beam with target $\sigma_{x,y} = 200$ µm at the iris.

This is the standard p^+ beam used at AWAKE. Although the bunch length is not directly measured by this code, we know that it is $\sigma_t \simeq 7$ cm. The actually measured beam size at the waist is smaller than expected by $\simeq 50$ µm. At the same time, these values are in accordance with the findings of Hafych *et al.* who found $\sigma_{x,0} = (130.0 \pm 6.5)$ µm and $\sigma_{y,0} = (140.0 \pm 7.0)$ µm.[36] Comparing the other parameters to the expectations of the baseline design (Tab.2.1) we also see that the β function and the norm. emittance are smaller (by about 1 m and 1 mm mrad). There is a weak $x - y$ asymmetry which was also seen in [36]. The position jitter shows a well-known and strong $x - y$ asymmetry; at BTV50 jitter is about ten times stronger along the x-axis, see Tab.2.3 and Fig.2.3. At the other cameras the factor reduces to two to three times. These results match in general with the results from the 2021 Autumn runs.

It is important to note that during Run 1 in 2022 a beam of a shape implying a waist position of $(5$ to $11)$ m upstream to the iris, a norm. emittance of $(1$ to $2)$ mm mrad and a beam size at the iris of $(220$ to $250)$ µm (and $(120$ to $150)$ µm at the waist) was found. A beam of this shape can only be fitted poorly since all beam sizes that are measured
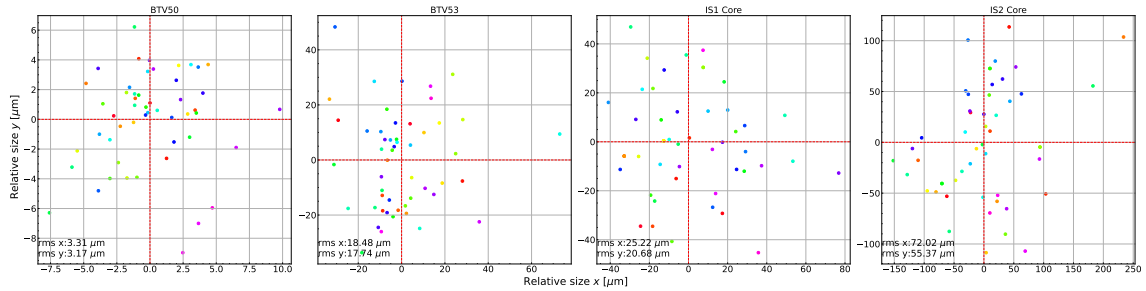
---

[7]For technical reasons, for this data set the p^+ population measurement was not working. No exact result is therefore available.
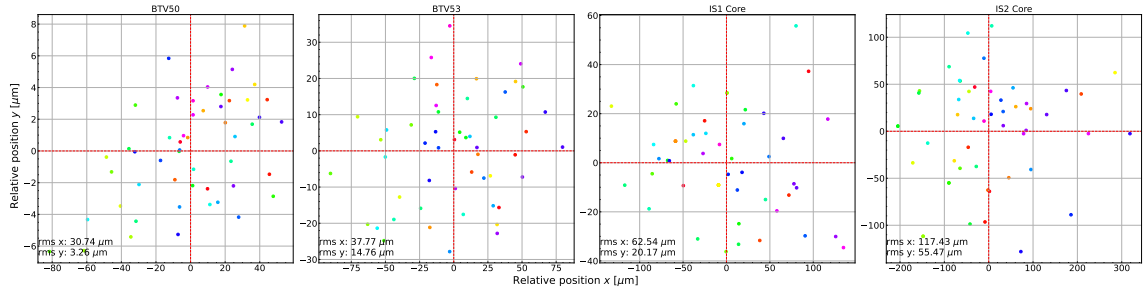
(a) Relative **position** jitter
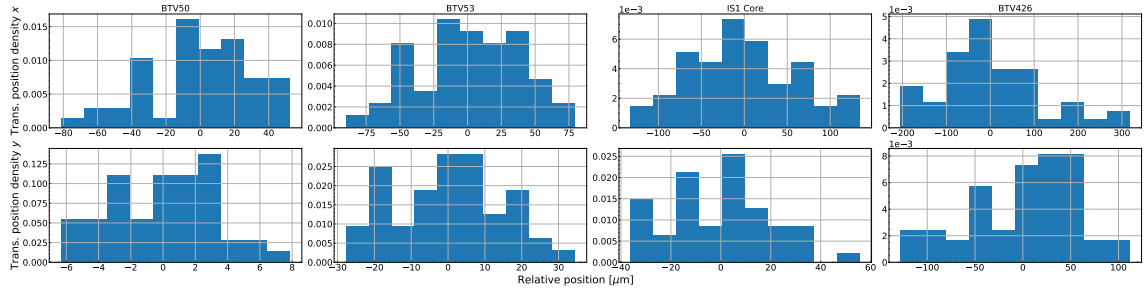
(b) Relative **position** jitter as histogram

(c) Relative transverse **beam size** jitter
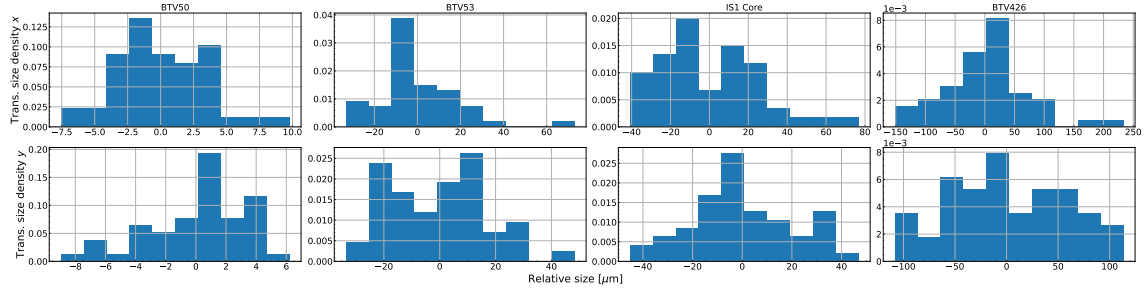
(d) Relative transverse **beam size** jitter as histogram

Figure 2.3: Summarised p^+ beam event-to-event jitter results of a beam with target transverse beam size at the plasma entrance of $200\,\mu\text{m}$. The origin is found by taking the average (red cross) of the absolute position or transverse size of the events. The points are sequentially rainbow colour-coded (red to violet), i.e., points of similar colour were time-wise close to each other.

tend to be dependent on each other, see Eq.(2.2). So, the results should be treated with care. This situation was mainly due to an about 60 µm bigger beam size measurement at BTV53 while the other cameras provided similar values as we have seen before. For reasons explained in section 2.2.1 no re-calibration was possible. The measurement taken in the same time period for the 330 µm beam, on the other hand, shows good agreement with MADX [8] simulations. In Run2 in 2022 this phenomenon disappeared. The origin of its occurrence is unclear.

The comprehensive visual summary of the standard characteristics is given in Fig.2.2. The plot shows the transverse envelope of a beam with target $\sigma_{x,y} = 200\,\mu$m at the iris. All such plots share the same description: blue and yellow main lines show the beam envelope based on average trans. size measurements in x and y; circular points indicate average beam size measured at cameras with standard deviation given; semi-transparent lines show envelopes of individual events; semi-transparent area obtained by cross-fitting (described in section 2.3); dotted vertical lines show the waist position; crosses denotes simulated values by MADX.

2.4.2   Beam of 330 µm Transverse Size at Plasma Entrance

Here, the beam provided by intermediary beam optics during the development of the 500 µm optics is presented. It shows a similar (angular) divergence to that of the standard beam. Due to the larger beam size at the waist, this leads to an increase of the norm. emittance. The agreement with MADX simulation is satisfying, and the strong $x - y$ asymmetry is supported by simulations. The y-axis envelope in Fig.2.4, however, also shows the high sensitivity on the BTV53 measurement when it comes to the determination of the beam parameters.
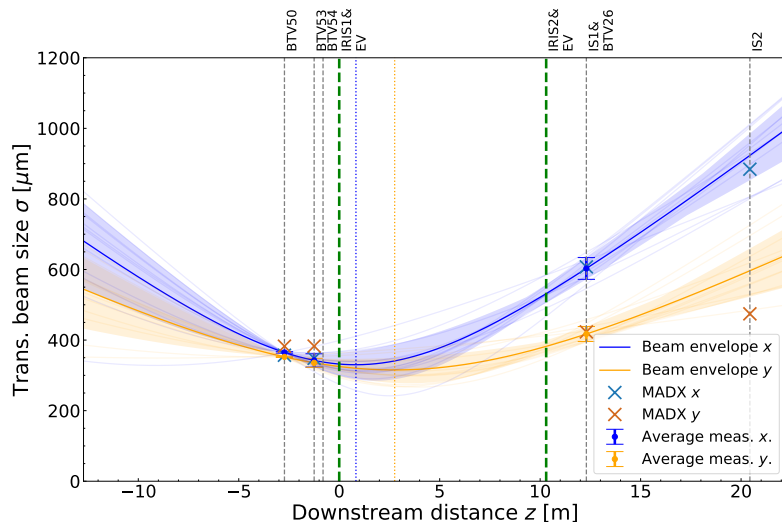

Figure 2.4: Transverse envelope of a beam with target $\sigma_{x,y} = 330\,\mu$m at the iris. See page 23 for further explanations.

---

[8]MAD stands for Methodical Accelerator Design. With MADX beam lines can be simulated. All MADX simulations were performed by *Dr Vittorio Bencini*.

2.4.3 Beam of 560 µm Transverse Size at Plasma Entrance

The beam envelope of a 560 µm beam at the plasma entrance is shown in Fig.2.5. Within the precision of the measurements the results are satisfying. It is important to note that the beam waist in y lays with (-4.9 ± 2.3) m rather far upstream the iris. Two beams of different populations are analysed and presented: $\sim 2 \times 10^{11}$ p+ and $\sim 2.86 \times 10^{11}$ p$^+$. The measured beam size at BTV50 does not depend on the beam population. At BTV53 and IS1 however the measured beam size is about 30 µm smaller. This ends up in a slightly smaller beam size at waist $(-5$ to $-6)$ %, but massive increase of the angular divergence and therefore also the emittance $(34$ to $50)$ %.
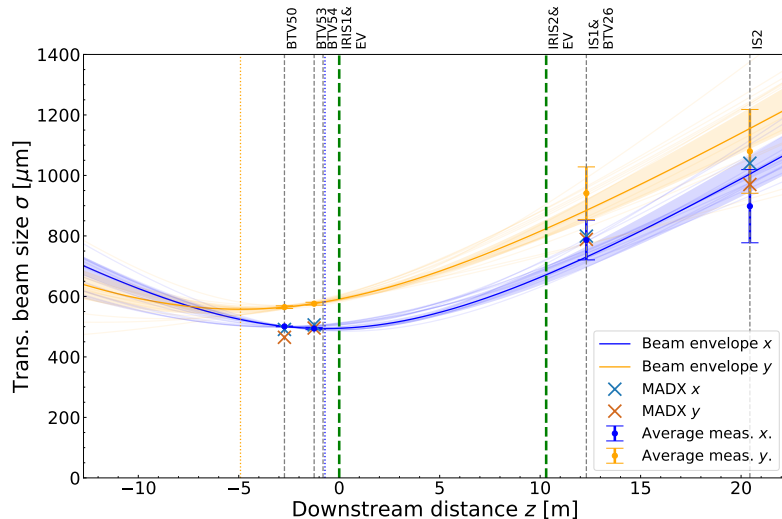

Figure 2.5: Transverse envelope of a beam with target $\sigma_{x,y} = 500$ µm at the iris. See page 23 for further explanations.

Especially when working with the higher populated beam $(\sim 2.86 \times 10^{11}$ p+) we were confronted with an issue already mentioned in section 2.2.4. We found ourselves in the situation where with the current filter configuration on BTV53 either the camera scratches on the saturation threshold, or, with the next stronger available filter $(+OD1)$ we only receive about 10 % of the signal. The signal-to-noise ratio decrease by up to a factor of ten and the signal becomes not only difficult to fit but provides specific to this case $(-16$ to $-17)$ % smaller beam sizes. As a results the calculated beam size at the waist is reduced by about 50 % along the x-axis. Looking at Fig.A.2 in the appendix shows clearly that this is physically wrong. Again, the sensitivity on BTV53 is demonstrated.

2.5 An Overview of Systematic Error Sources

The presented method follows a statistical approach and statistical errors can be quantified. The much more dangerous sources of errors are of a systematic nature. Some potential sources such as pixel calibration have been reviewed several times. Some are known and have been demonstrated and identified, such as the fact that even small relative deviations in beam size measurements between BTV50 and 53 have a large (in relation to e.g., IS2) influence on waist position (and thus beam size at waist) and the angular divergence, due to their proximity and critical position near the waist. Some others are discussed below.
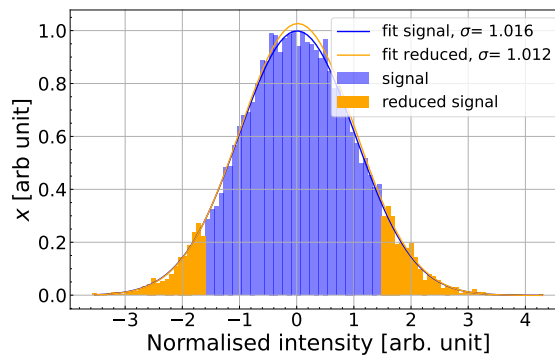
Figure 2.6: Simulated Gaussian fitting from only the winglets versus the entire signal on noise free but binned data points.

2.5.1 Secondary Particles

While discussing ways to increase the signal-to-noise ratio during the first run of 2022 approaches not only performed in post-processing but directly when measuring the signal were discussed. One hypothesis was that a big part of the noise could be due to secondary particles produced at the screens further upstream. This would mean that BTV50 (the first camera) would only see the little noise from secondary particles propagating with the beam coming from SPS. However, all further cameras would register at least a part of the secondary particles produces by scattering when the beam passed the previous screens.

This is a side story of this thesis, but it was worth to test it. It turned out that the signal becomes almost noise free when no screens are present upstream to the online measurement station. An example is given in Fig.A.1 in the appendix. Nevertheless, it has been decided to go on with the well-established measurement procedure. The beam characterisation measurements are meant to be made daily before the actual physics experiments to verify the properties of the proton beam and individual measurements per screen would take two to three times more time.

2.5.2 Beam Shape

Our model assumes the beam being perfectly bi-Gaussian in the transverse plane. Another corollary of this thesis is that this is only partially true – with unexpected influence on the results. With the motivation to exploit the existing setup as much as possible and to increase the signal-to-noise ratio, the possibility of performing Gauss fitting only on the non-saturated pixels (i.e., the Gauss winglets) was explored. On an artificial, noise-free but binned test sample this works without major limitations.

This is demonstrated in Fig.2.6. Taking an average over 1000 simulations, where each consists of 10,000 samples binned into 100 bins, the Gaussian standard deviation of the fitted reduced data is around 3 % smaller than that of the fitted full data. For the reduced data set the 40 center bins are masked. In the experiment, however, we find a massive increase of the measured beam size at high saturation; about 15 % for BTV426 and up to 100 % for BTV53.

This can be explained with a twofold bi-Gaussian model. Already in [36] it was

suggested that a better circumscription is possible if the beam is circumscribed by a core and halo part which are both Gaussian distributed but have potentially different waist positions, angular divergences and beam size at waist. If a camera is saturated, it will measure more of the lower amplitude portion of the beam, which could lead to a larger beam size. Further studies would be needed to provide a conclusive answer to this phenomenon and confirm this hypothesis.

2.6   Technical Discussion and Proposals

From a technical perspective, note that results provided by this code become better the higher the number of events that are used. However, on average about half of the initially recorded events are rejected. One part falls away because of SPS extraction issues, another because of wrong triggering and last but not least a part is lost because Gauss fitting becomes a challenge if the signal-to-noise ratio is weak. And, this is indeed often the case, depending on the beam size and beam population. If it is decided to improve the approach taken by this work, a big improvement can be made by installing a bigger filter wheel with finer gradations (see section 2.2.4). This is especially needed for BTV53 and would be advantageous for BTV50.

For IS1 and IS2 no filter is used in general and still little OTR light reaches the camera. The situation is worse for IS2. Changing the light splitter towards another splitting fraction is probably no option, so using IS2 HALO with removed mask might be a solution.

To ease the critical situation of BTV53, a change to a digital camera with higher resolution is suggested in addition to a finer filter gradation. This should have priority in the event of an improvement of the setup.

3 General Theory of Wakefields

In this chapter, which deals with the main issue – plasma wakefields –, the most basic physical notions are introduced. This chapter does not claim to be in any way complete or exhaustive. Rather, the concepts discussed here are intended to provide a better understanding of the results obtained.

The following section will introduce the origin of two basic forces being present when a charged particle bunch travels through vacuum. After this basic analysis, the situation of a beam travelling through plasma and the zeroth and first mode of the two stream instability will be discussed.

3.1 Beam Stabilising in Vacuum

To understand the forces on the beam particles mathematically, a beam travelling in a vacuum shall be considered first. Let us consider a long and thin relativistic beam of charged particles which are in the transverse plane symmetrically bi-Gaussian and in the longitudinal direction uniformly distributed over the length of the beam. All distributions are centred at the origin (x=0, y=0, z=0). Thanks to the symmetries introduced by such a beam it is useful to work as soon as possible in cylindrical coordinates ($\hat{\boldsymbol{e}}_r$, $\hat{\boldsymbol{e}}_\phi$, $\hat{\boldsymbol{e}}_z$).

3.1.1 Mathematical Description of the Resulting Lorentz Force

Remembering the Maxwell equations (MW):

$$\nabla \cdot \boldsymbol{E} = \frac{\rho}{\varepsilon_0} \tag{MW 1}$$

$$\nabla \wedge \boldsymbol{B} = \mu_0 \boldsymbol{J} + \mu_0 \varepsilon_0 \frac{\partial \boldsymbol{E}}{\partial t} \tag{MW 2}$$

$$\nabla \wedge \boldsymbol{E} = -\frac{\partial \boldsymbol{B}}{\partial t} \tag{MW 3}$$

$$\nabla \cdot \boldsymbol{B} = \boldsymbol{0} \tag{MW 4}$$

where,

- $\boldsymbol{E}(\boldsymbol{x})$ and $\boldsymbol{B}(\boldsymbol{x})$ are the electric and magnetic fields at position $\boldsymbol{x}$,

- $\rho(\boldsymbol{x})$ and $\boldsymbol{J}(\boldsymbol{x})$ are the charge and current densities at position $\boldsymbol{x}$,

- μ_0 is the magnetic permeability of the vacuum,

- ε_0 is the electric permittivity of the vacuum,

let us consider the magnetic field and electric field separated from each other.

Electric Field   The electric field acting on a particle at a distance r from the beam propagation axes z can be found considering electrostatics ($\boldsymbol{B} = \boldsymbol{0}$ and $\boldsymbol{J} = \boldsymbol{0}$). Then Maxwell (MW 2) and (MW 3) become:

$$0 = \frac{\partial \boldsymbol{E}}{\partial t} \qquad\qquad \nabla \wedge \boldsymbol{E} = \boldsymbol{0} \tag{3.1}$$

Applying Gauss's theorem we get the integral form of Maxwell (MW 1):

$$\nabla \cdot \boldsymbol{E} = \frac{\rho}{\varepsilon_0}$$
$$\int_V d^3x \, \nabla \cdot \boldsymbol{E} = \int_V d^3x \, \frac{\rho}{\varepsilon_0} \tag{3.2}$$
$$\oint_{\partial V} \boldsymbol{d\sigma} \cdot \boldsymbol{E} = \int_V d^3x \, \frac{\rho}{\varepsilon_0}$$

where V is the integration volume and ∂V its surface. Let us for this part assume that the beam length goes to infinity. Thanks to this we can work in cylindrical coordinates and with the corresponding symmetry we get:

$$2\int_A d\sigma_A \, E_z + Lr \int_0^{2\pi} d\phi \, E_r(r) = \frac{\pi L r^2 \bar{\rho}}{\varepsilon_0} \tag{3.3}$$

Here, the integral over top and bottom area A of the cylinder is equal to zero. The variable $\bar{\rho}$ denotes the average density in volume V. Finally solving for the radial electric field $E_r(r)$ one gets:

$$E_r(r) = \frac{1}{2}\frac{r\bar{\rho}}{\varepsilon_0} \tag{3.4}$$

Note that $E_r(r)$ can only be exactly determined in this way when the beam is assumed to be infinitely long, otherwise the electric field flux through A is not zero. However, for the long, thin beam at AWAKE where $\sigma_t \gg \sigma_\perp$ this is a good approximation. Note that $\sigma_t = \sigma_z/c$ is the bunch duration which is connected through the speed of light to the bunch length and $\sigma_\perp$ denotes the transverse bunch (beam) size.

Magnetic Field   Let us now come to the the magnetic field, which is induced by the beam current itself, at the same distance r from the axes as above: Let us consider the magnetostatics of the problem ($\boldsymbol{E} = \boldsymbol{0}, \rho = 0$).[1] Maxwell (MW 2) and (MW 3) then become

$$\nabla \wedge \boldsymbol{B} = \mu_0 \boldsymbol{J} \qquad\qquad 0 = \frac{\partial B}{\partial t} \tag{3.5}$$

---

[1]One may pose the question why ρ can be set to zero. The reason for this is that the charge only interacts with the Maxwell equation through the Gauss law, which is not of importance for the description of magnetostatics. The current density J on the other hand is not equal to zero.

Applying Stokes' theorem we get the integral form of the Maxwell (MW 2):

$$\nabla \wedge \boldsymbol{B} = \mu_0 \boldsymbol{J}$$
$$\oint_S \boldsymbol{d\sigma} \, \nabla \wedge \boldsymbol{B} = \mu_0 \oint_S d\boldsymbol{\sigma} \cdot \boldsymbol{J} \tag{3.6}$$
$$\oint_{\partial S} \boldsymbol{dl} \cdot \boldsymbol{B} = \mu_0 \oint_S d\boldsymbol{\sigma} \cdot \boldsymbol{J}$$

where S denotes the integration surface with boundary ∂S. Taking S equal to a slice of the cylinder with radius r we can further simplify the expression:

$$-r \int_0^{2\pi} d\phi \, B_\phi = \pi r^2 \mu_0 \bar{J}_z$$
$$-2\pi r B_\phi = \pi r^2 \mu_0 \bar{J}_z \tag{3.7}$$

Which can be solved to give

$$B_\phi(r) = -\frac{1}{2}\mu_0 r \bar{J}_z \tag{3.8}$$

where B_ϕ is the resulting magnetic field directed in $\hat{\boldsymbol{e}}_\phi$ and $\bar{J}_z$ the averaged beam current density flowing through S. We can also write the B field more generally, where $\boldsymbol{r}$ is not the radius of the cylinder but the arbitrary vector to the test particle. I denotes the total current flowing along in $\hat{\boldsymbol{e}}_z$:[2]

$$\boldsymbol{B(r)} = \frac{1}{2\pi}\mu_0 I \frac{\hat{\boldsymbol{e}}_z \wedge \boldsymbol{r}}{|\hat{\boldsymbol{e}}_z \wedge \boldsymbol{r}|^2} \tag{3.9}$$

We can write $\bar{J}_z$ as:

$$\bar{J}_z = q\bar{n}_b \beta c \tag{3.10}$$

where $\bar{n}_b$ is the average beam density in V, $\beta = \frac{v}{c}$ and v the speed of the beam ($\boldsymbol{\beta} = \beta\hat{\boldsymbol{e}}_z$). By putting (3.10) into (3.8) one gets:

$$B_\phi(r) = -\frac{1}{2}\mu_0 r q \bar{n}_b \beta c \tag{3.11}$$

Resulting Lorentz Force The Lorentz force acting on the test particles is therefore given by:

$$\begin{aligned}
\boldsymbol{F} &= q(\boldsymbol{E} + \boldsymbol{\beta}c \wedge \boldsymbol{B}) \\
&= q(E_r\hat{\boldsymbol{e}}_r + \beta c\hat{\boldsymbol{e}}_z \wedge B_\phi\hat{\boldsymbol{e}}_\phi) \\
&= q(E_r + \beta c B_\phi)\hat{\boldsymbol{e}}_r \\
&= q\left(\frac{1}{2}\frac{r\bar{\rho}}{\varepsilon_0} - \frac{1}{2}\beta^2 c^2 \mu_0 r q \bar{n}_b\right)\hat{\boldsymbol{e}}_r \\
&= q\left(\frac{1}{2}\frac{r\bar{\rho}}{\varepsilon_0} - \frac{1}{2}\beta^2\frac{r\bar{\rho}}{\varepsilon_0}\right)\hat{\boldsymbol{e}}_r \\
&= q\frac{1}{2}\frac{r\bar{\rho}}{\varepsilon_0}\left(1 - \beta^2\right)\hat{\boldsymbol{e}}_r
\end{aligned} \tag{3.12}$$

---

[2]The more general case as in the lecture notes of the course "Classical Electrodynamics" given by *Prof Joao Penedones* (and based on lecture notes of *Prof Rattazzi* and *Prof Shaposhnikov*) at EPFL, Lausanne.[50]

where we have used the relation between vacuum permeability and permittivity $c^2 = \frac{1}{\varepsilon_0 \mu_0}$ and defined the average charge density $\bar{\rho} = q\bar{n}_b$ where $\bar{n}_b$ is the average particle density the beam sub-region V. Remembering the definition of the Lorentz factor $\gamma = \frac{1}{\sqrt{1-\beta^2}}$ we find:[3]

$$\begin{aligned} F_r &= q\frac{1}{2\gamma^2}\frac{r\bar{\rho}}{\varepsilon_0} \\ &= q^2\frac{1}{2\gamma^2}\frac{r\bar{n}_b}{\varepsilon_0} \end{aligned} \qquad (3.13)$$

Therefore, the resulting Lorentz force cause a collimated beam to diverge inversely proportional to the square of the Lorentz factor. This means the more a given beam is relativistic the more it stabilises itself. The self-induced magnetic field of the beam compensates the diverging effect of the electric field the closer the velocity of the beam comes to the speed of light. A resting bunch of particles would undergo a coulomb explosion. Furthermore, we see that due to the q^2 term in (3.13) this property is independent of the beam particle charge sign.

However we should keep in mind that a beam will never be perfectly collimated. This means the transverse momenta of all particles will never be collectively equal to zero. Therefore, the final beam divergence is not only determined by the Lorentz force in Eq.(3.13) but also by the transverse momentum distribution.

Situation in the Beam Frame using Special Relativity   To finish the consideration of the Lorentz force acting on an off-axis particle let us change to the reference frame of the beam. Let K be the laboratory frame and K' the frame of the beam moving with $\boldsymbol{v} = v\hat{\boldsymbol{e}}_z = \frac{\beta_{rel}}{c}\hat{\boldsymbol{e}}_z$ with respect to K. We would expect that by using the field definitions Eq.(3.4) and (3.11) we have derived above, we will find that in the beam frame K' the transverse magnetic field goes to zero since the current density is not present. At the same time, the electric field needs to compensate this by becoming stronger.

From an analysis of the behaviour of the Maxwell tensor (also called field strength) $F_{\rho\mu}$ under a Lorentz transformation we can find the transformation rules of the electric and magnetic fields.[4] The fields are transformed as:

$$\begin{aligned} \boldsymbol{E'}_\parallel &= \boldsymbol{E}_\parallel \\ \boldsymbol{E'}_\perp &= \gamma(\boldsymbol{E}_\perp + c\boldsymbol{\beta} \wedge \boldsymbol{B}) \\ \boldsymbol{B'}_\parallel &= \boldsymbol{B}_\parallel \\ \boldsymbol{B'}_\perp &= \gamma\left(\boldsymbol{B}_\perp - \frac{1}{c}\boldsymbol{\beta} \wedge \boldsymbol{E}\right) \end{aligned} \qquad (3.14)$$

where the indices $\perp$ and $\parallel$ denote the transverse and longitudinal parts of the fields, respectively. Applying this to our case we get $\boldsymbol{E'}_\parallel = \boldsymbol{0}$ since the beam is infinitely long, and $\boldsymbol{B'}_\parallel = \boldsymbol{0}$.

---

[3]The same results without the derivation we performed here can be found in the book "Particle Accelerator Physics" by *Wiedemann*.[51]

[4]A detailed derivation would go beyond the scope of this work. More details can be found in the book "Classical Electrodynamics" by *Jackson*.[40]

By using Eq.(3.4) and (3.11) the transverse directed electric field is found:

$$
\begin{aligned}
\boldsymbol{E'}_\perp &= \gamma(\boldsymbol{E}_\perp + c\boldsymbol{\beta} \wedge \boldsymbol{B}) \\
&= \gamma(E_r + \beta c B_\phi)\boldsymbol{\hat{e}_r} \\
&= \gamma E_r(1 + \beta^2)
\end{aligned}
\tag{3.15}
$$

Using the same equations transverse magnetic field becomes in the beam frame K' as expected equal to zero:

$$
\begin{aligned}
\boldsymbol{B'}_\perp &= \gamma\left(\boldsymbol{B}_\perp - \frac{1}{c}\boldsymbol{\beta} \wedge \boldsymbol{E}\right) \\
&= \gamma\left(B_\phi + \frac{1}{c}\beta E_r\right)\boldsymbol{\hat{e}_r} \\
&= \gamma\left(-\frac{1}{2}\frac{r\bar{\rho}\beta}{\varepsilon_0 c} + \frac{1}{2}\frac{r\bar{\rho}\beta}{\varepsilon_0 c}\right)\boldsymbol{\hat{e}_\phi} \\
&= 0
\end{aligned}
\tag{3.16}
$$

This is indeed a very satisfying result with which to conclude the consideration of forces being present when an ideal, relativistic beam moves through vacuum.

The result in Eq.(3.13) shows how a relativistic particle beam stabilises itself. However, in the case of AWAKE the beam does not move in a vacuum but in a plasma. This means that due to the plasma electron response on the beam additional radial focusing and defocusing forces acts – this is the content of the next sections.

3.2 Beam-Plasma Interaction

The complete theory of plasma wakefields, their formation, behaviour and decay is far from trivial and involves a wide range of physics from plasma physics to special relativity and beam physics.

The plasma (angular) frequency (3.17) is probably the most central concept in the field of plasma wakefields. Its origin can be explained by thinking about a plasma initially at equilibrium which is affected by a small perturbation. By this perturbation the plasma electrons are pushed out of equilibrium. As a consequence, a restoring force acts on the plasma ions and electrons, pulling them back in equilibrium. Due to their little mass electrons undergo a strong acceleration towards their equilibrium position, but will obviously not abruptly stop once they arrive there. As an analogy, a pendulum which is deflected by a small angle and then kept free can be taken to help. The pendulum will overshoot its equilibrium position continue oscillating around it. In the same way a plasma electron will overshoot its equilibrium position, ultimately resulting in an oscillation. However, in a plasma there is not just one electron but many. This is why the resulting effect of a perturbation is of collective nature. The plasma frequency is the natural frequency at which plasma electrons "prefer" to oscillated. The frequency can for example be derived from a two-fluids model in which a small perturbation disturb the equilibrium.
Due to the mass difference between plasma electrons and plasma ions the latter undergo almost no acceleration and can be considered as static. At the same time, this is not always true, since for a perturbation of low frequency so-called acoustic ion waves can develop.

However, these are not relevant for AWAKE.

The plasma frequency Eq.(3.17) depends on the plasma electron density n_0, the elementary charge e and the electron mass m.

$$\omega_p = \sqrt{\frac{n_0 e^2}{m}} \tag{3.17}$$

In this chapter we assume that the plasma ion density is *initially* equal to the plasma electron density ($n_0 = n_{ion}$). This assumption can also be made for the experiment before the proton beam enters the plasma.[29]

Note also the definition of the plasma wave-number k_p Eq.(3.18) and some further "trivial" relations Eq.(3.19), where ω_p the angular frequency and c the speed of light:

$$k_p = \frac{\omega_p}{c} \tag{3.18}$$

$$\lambda_p = \frac{2\pi}{k_p}, \qquad f_p = \frac{\omega_p}{2\pi} \tag{3.19}$$

In the case of AWAKE, the small perturbation to the plasma is given by the proton beam which is under-dense with respect to the plasma, which will be discussed in the next section.

3.3 Self-Modulation Instability

Let us again first consider an unperturbed plasma. In this thermodynamic equilibrium state the plasma will be homogeneous (assuming an infinite plasma) and all the particle velocities are Maxwell distributed.[5] The free energy in this state will be zero and therefore external energy is necessary to excite plasma waves. However, as soon as the free energy becomes nonzero, be it through gravitational or electro-magnetic fields, density gradients or even just boundaries, a self-excitement of the plasma can occur.

Before this self-excitement but already in the presence of an external influence (like a force field) the plasma can be in an equilibrium state, but already a very small perturbation might be enough that this unstable equilibrium state leads towards another state in order to minimise the free energy of the plasma. The category of instabilities which describe a perturbation by a particle beam in relative movement to the plasma is called (two) stream instability.[53] The self-modulation instability is the zeroth mode of the the two stream instabilities.

The *self-modulation instability* (SMI) is the source of focusing and defocusing forces acting on the proton beam in the radial direction. It is, as the name implies, the reason why a relativistic and with respect to the plasma wavelength long and thin proton beam undergoes self-modulation in a cold plasma. SMI is based in its core on the basic plasma-beam interaction described in the previous chapter.

---

[5]Lecture notes "Introduction à la physique des Plasmas" given by *MER Stefano Alberti* at EPFL, Lausanne.[52]

We can consider the beam in the plasma in such a way that each proton is handled individually. This means we have as many electrostatic problems as we have protons in the beam, and as many Green functions could be found. Each proton therefore creates a plasma electron response. The collective effect of the plasma is given by superimposing all individual scalar potentials. If the beam is long and the distribution is not smooth, some of the plasma electron responses will be stronger and others weaker. All plasma electrons start oscillating and the strongest response will eventually define the phase of these oscillations – the SMI takes place. The electric fields created by the oscillating plasma electrons are called *transverse wakefields*. They are both focusing or defocusing.

The SMI is therefore characterised by a radial force whose amplitude oscillates along the beam's axis of propagation. This means that radial focusing and defocusing regions alternate along the proton beam. This ultimately leads to the creation of a so-called *micro-bunch structure*, which in return further amplify the transverse wakefields. Since the radial electric field is generated by the same proton bunch[6] as the one on which it acts, we speak of *self-modulation* (SM). The result of this self-modulation is a train of micro-bunches with a periodicity of the plasma wavelength Eq.(3.19). The emergence of the micro-bunch structure now also creates wakefields in the longitudinal direction. These *longitudinal wakefields* have one single phase and are the ones with which injected electrons can be accelerated.

Since this phenomenon arises from an instability it is difficult to characterise its starting point. The source that leads to the natural onset of the instability is mainly noise (spikes) in the proton beam distribution. Without this spikes and for a long beam as we have at AWAKE the plasma electrons are all collectivly pulled towards the proton beam but not excited in a high enough frequency as it is the case for sharp or noisy distribution. This case will be discussed below in the section about adiabatic focussing (3.6).

Since the noise, meaning some spikes in the beam distribution, varies from shot-to-shot, the micro-bunch train is not reproduced from shot-to-shot. The starting point of SMI varies and so does the phase of the bunch train. To overcome this problem, the onset of the modulation must be seeded (see next section). From a simulation point of view, it is highly nontrivial to simulate a phenomenon arising from noise, since a exact characterisation needs to be done.

As far as the growth of the SM is concerned, we are in a better position to do simulations and theoretical work, the latter at least if we are in the regime of linear theory. In a recently published paper it has been stated that the transverse (or radial) *wakefields* (electric fields) grow as follows.[5]

$$W_\perp(\zeta, z) = W_{\perp 0} e^{\Gamma(\zeta, z)z} \tag{3.20}$$

where $W_\perp$ is the transverse wakefield at position z and slice ζ with origin at the bunch centre, $W_{\perp 0}$ denotes the initial wakefield at $z = 0$, and Γ is called the *growth rate*.

---

[6]Note that a beam can in general consist of multiple bunches. However, also a single bunch can be a beam. While in the framework of characterising the protons coming from an accelerator we use the word *beam*, we use in the framework of plasma physics the word *bunch* with preference.

Radial Extent of the Micro-Bunch Train   For the linear regime, theoretical work to describe the radial extent as a function of the proton (p^+) bunch propagation distance z and the position within the bunch ζ has been done, for example by Schroeder *et al.* This allows us understand the growth of the micro-bunch train by SMI.[24, 32, 33, 54].

Let us assume a long proton bunch with a radial flat top bunch profile. Let $r_b = r_0 + r_1 r_0$ be the beam radius of a particle beam undergoing modulation. The initial beam size is given by $r_0 = r_b(z = 0, \zeta = 0)$. Then it has been shown in [32] that:

$$r_1 = \delta r \frac{3^{1/4}}{(8\pi)^{1/2}} \Gamma^{-1/2} e^\Gamma \cos\left(\frac{\pi}{12} - k_p \zeta - \frac{\Gamma}{\sqrt{3}}\right) \tag{3.21}$$

with the growth rate Γ:

$$\Gamma = \frac{3^{3/2}}{4} \left(\nu \frac{n_{b0} m}{n_0 m_b \gamma} k_p^3 |\zeta| z^2\right)^{1/3} \tag{3.22}$$

where m_b is the proton mass, m the electron mass, n_0 the unperturbed plasma density, k_p the plasma wave-number, $\delta r = \hat{r}(z = 0, \zeta)$ and $\nu = 4 I_2(k_p r_0) K_2(k_p r_0)$ is a term consisting of modified Bessel functions of first and second kind (both of second order).

However, for this work the exact equation is less of interest than some proportionality relation which can be derived from Eq.(3.21). This will allow us to embed our results in certain aspects of plasma wakefield theory.

In a first step Eq.(3.21) can be simplified by focusing on the maximal radial extent of the bunch. This is done by setting the cosine term equal to one. Let us define r_m according to this:

$$r_m = \delta r \frac{3^{1/4}}{(8\pi)^{1/2}} \Gamma^{-1/2} e^\Gamma \tag{3.23}$$

This expression describes the so-called *bunch envelope* on which will lie the focus of this work.

The growth rate remains unchanged and scales with bunch density as:

$$\Gamma \propto (n_{b0} \nu)^{1/3} \tag{3.24}$$

At first, one might think that a similarly simple relation could be found for the initial beam size, since for a constant bunch population, the density decreases with increasing beam size since $n_{b0} \propto 1/r^2$. Looking more closely at (3.22), we see however that ν depends on the initial beam size through the two modified Bessel functions. This further amplifies the effect of decreasing growth rate by increasing the transverse beam size.[7] In Fig. 3.1 this can analysed visually. The blue line shows the relative growth rate of SM in the linear regime with respect to the growth rate of a 200 μm beam (with ζ and z being fixed). The growth rate again given by (3.22) but *without* the combined Bessel factor ν shows less relative decrease when the initial beam size increases. Note that this curve follows (3.24).

---

[7]In the simulations and theory it is often assumed that the bunch is radially symmetric and it is correct to talk about the radial beam size. However, in reality the bunch will never be perfectly radial symmetric, therefore it is more correct to talk about the transverse beam size which might be split along the x- and y-axes.
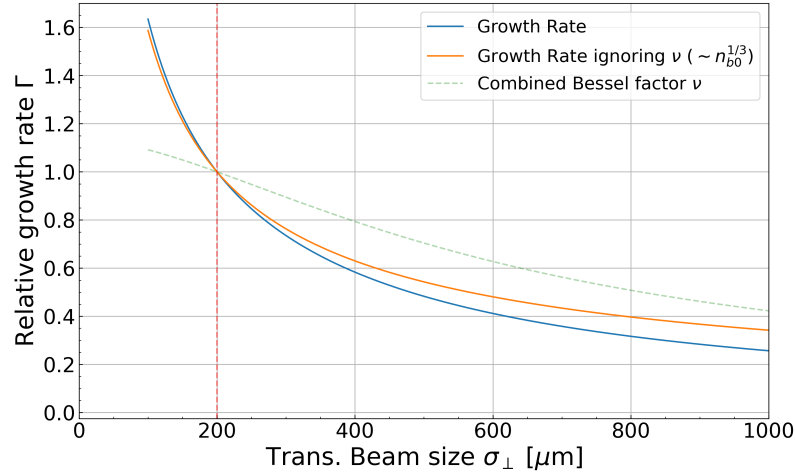
Figure 3.1: Comparison of the relative growth rate with respect to a bunch having a transverse size 200 µm at the plasma entrance. The green dashed line is not a growth rate but the combined Bessel factor ν also on a relative scale with respect to 200 µm. The positions ζ and z are kept fixed.

It is to note that this development can only be applied with caution to the experimental situation. First of all, the beam provided by SPS has not a radial flat top but a Rayleigh (in Cartesian coordinates bi-Gaussian) distribution and the linear regime might be left, depending on the chosen beam size, while the bunch moves through the plasma.

To conclude, it can be assumed based on linear theory that an increased p^+ bunch radius leads to a decrease of the growth rate according to the following approximated proportionality:

$$\Gamma \sim r_0^{-\frac{2}{3}} \tag{3.25}$$

3.4 Seeded Self-Modulation

To control SMI the self-modulation can be seeded. The means the start of the SMI process is controlled. In order to do this in the experiment the short pulsed laser is not only used to ionise the plasma but also provides with its front at a defined position in the bunch a sharp edge where the creation of plasma wakefield starts. This abrupt start of ionisation inside the p^+ bunch leads to a so-called seeding of self-modulation. The sharp edge is called a *relativistic ionisation front* (RIF). Thanks to seeding, the SM process, especially the phase, can be made reproducible from shot-to-shot, which is the basis for electron acceleration. This means that at a distance $\Delta\zeta$ after the RIF, either a micro-bunch or no micro-bunch (or something in between) can be found in each shot. It has been shown at AWAKE that with seeding the self-modulation phase is controlled and reproducible in a way that fits for electron acceleration from 19 MeV to 2 GeV.[3] Seeded SM also leads to a larger wakefield growth rate than in the SMI case.[5]

In the same paper it has been demonstrated that seeding is not only possible with the RIF but also with a preceding electron bunch. In addition, it was shown the growth rate and the amplitude of the wakefields can be controlled independently from each other through the charge of the proton bunch and the charge of the electron bunch.[5] In this experimental work it will be similarly demonstrated that the growth rate in the unseeded

case depends on the initial transverse bunch size.

3.5   Hose Instability

Hosing is a plasma instability that also occurs in AWAKE. It is the first mode of the two stream instabilities, while SMI represents the zeroth mode.[55, 56] Hosing can also often be attributed to a misalignment of the proton and/or laser beam. However, in theory it does not occur for a perfectly axis-symmetric p^+ bunch.[24] Hosing leads to a transverse displacement of the beam centroid (core) and thus disturbs the micro-bunch train. Visually the latter starts looking under hosing laterally warped. Hosing can be so strong that the micro-bunch train gets destroyed. Since SM is a feedback process, this also affects the wakefields which are disturbed as well.[57] There are also higher-mode two stream instabilities existing which can cause a filamentation of the micro-bunch train. However, thanks to chosen thin proton beam, they have an negligible effect on the micro-bunch train.

3.6   Adiabatic Focusing

The description of adiabatic focusing given here is of qualitative nature. A mathematically more rigorous and early study about adiabatic focusing can be found in [58]. Let the considered beam have again a transverse bi-Gaussian profile. The longitudinal distribution is Gaussian as well. No noise shall bias the distribution – the distribution are smooth. The beam is long, thin, relativistic which means that the length of this beam is much longer than the skin depth of the beam surrounding the plasma $\sigma_t \gg 1/ck_p$. The transverse size, on the other hand is comparable to the skin depth.[8]

The plasma the beam travels through is cold and over-dense with respect the beam density.

The beam propagating through the plasma can again be seen as a perturbation to the latter. Since the beam is much longer than the skin depth of the plasma, this perturbation is slow with respect to the plasma frequency ($\omega_p \gg \frac{\pi}{2\sigma_t}$). In the experiment the difference is one to two orders of magnitude.

As an analogy, we can imagine again a mathematical pendulum which has the natural frequency $w_0 = \frac{g}{l}$, where g is the acceleration due to gravity and l is the length of the string – the natural frequency of the pendulum corresponds to the plasma frequency. An "adiabatic" deflection of this pendulum means that its entire movement is guided and much slower than desired by the pendulum ($w_{adiab} \leq w_0$) and no excitation of a periodic motion takes place. To finish this analogy imagine the pendulum being on a large container vessel operated by the company *Adiabatic Shipping*. This large vessel may slowly role in heavy see and the pendulum will always follow the rolling motion. A smaller ship under the same circumstance will heavily rock and pitch – at much higher frequency. As a consequence the pendulum will be excited in way that it starts harmonically oscillating.[9]

---

[8]To be consistent throughout this work the beam length is denoted already in this section as σ_t, which has units of time and can be seen as a bunch duration. In the experiment the relativistic beam ($\beta_{rel} \simeq 1$) will be described in units of time as well. It therefore holds $\sigma_t = \sigma_z/c$.

[9]Obviously such ships cannot be part of the fleet of *Adiabatic Shipping*, since that would result in a

Therefore, *adiabatic* in the context of plasma physics means that there is an externally induced motion which is slower than the plasma oscillation frequency. A quantity that remains constant during an adiabatic process is called adiabatic invariant.

When the proton beam travels through the over-dense plasma a transverse focusing force acts on the beam. This effect is called adiabatic focusing because it is based on an adiabatic response of the plasma electrons to the beam particles.

In fact, the light plasma electrons are pulled, by the presence of the proton beam, towards the longitudinal beam axis while the plasma ions of larger mass can be considered almost immobile. The displaced plasma electrons lower the total charge density within the proton beam, which in turn weakens the electrostatic forces $p^+ - p^+$ within the beam. Or in other words: the displaced electrons partially compensate the proton beam charge, which in turn reduces the electric field component of the Lorentz force Eq.(3.13) of all off-axis protons in the vicinity of the beam. Since the current density of the beam and thus the magnetic field component is not changed by this, the Lorentz force can change its sign and have an overall focusing effect.

Adiabatic focussing does not stand in contradiction with SMI. Indeed, SMI can be seen as addition to adiabatic focusing where on top of the low frequency (adiabatic) focusing wakefield, also high frequent focusing and defocusing fields occur.

---

misleading company name.

4 Plasma Wakefield Simulations

4.1 Basic Notions about Plasma Wakefield Simulations

To simulate beam-plasma interactions multiple codes are available. *Fluide codes* treat the beam as a liquid and thus the framework of magnetohydrodynamics widely known in plasma physics is used. These codes are in general quick to execute but do not go beyond the linear or weakly non-linear regime.[59] An example is *VORPAL* or codes used in fusion physics. In *Particle-in-cell* (PIC) codes the beam and plasma are treated as a large number of macro-particles which deposit charge on a simulation grid. Based on this charge the electromagnetic fields are calculated. These codes are able to solve highly non-linear problems, but have the disadvantage of being very computational intensive.

To overcome the problem of computational intensity one can take advantage of the assumption that the beam and the plasma evolve on two different timescales separated by multiple orders of magnitude. This means that the beam-plasma interaction is calculated only in a small so-called simulation window (of the order of centimetres). The driver beam particles are not updated during this time. Only once this "sub-simulation" has finished are the driver beam particles updated to their new coordinates with corresponding momenta based on the electromagnetic fields previously calculated. A new sub-simulation is then started at the new, further downstream position. Here, the interactions are again calculated, with the output values of the previous sub-simulation as initial values. Such codes are called *quasi-static* PIC codes. Examples of codes are *Lcode*, *qv3d* and *Quick-PIC*.[60, 61] If however plasma and beam are treated equally (non-quasi-static approach) we talk about *Fully electromagnetic* PIC codes. Examples here are *OSIRIS*, *VLPL* and *WARP*.[59, 62]

4.2 Particle-in-Cell Codes

This section intends to give an understanding of what PIC codes are and how they work. Complicated mathematical descriptions, however, will be omitted since in this work such a code was applied but not developed. Supplementary information can be found in [61] by Pukhov.

A PIC code can be seen as a numerical plasma since in analogy to a real plasma it consists of individual particles which generate and "feel" electric and magnetic fields. In a *full* PIC code the Maxwell equations are solved and the positions and momenta of all the particles are updated at each time-step. Since a real particle bunch (in our case with a population of up to 3×10^{11} p^+) is too complex to be simulated one-by-one, a bunch of particles is substituted by one macro-particle which can move on the simulation grid. Like

this the number of particles to simulate is reduced while physical properties are preserved, even-though they are spatially averaged. This approach is therefore to a limited extent similar to the mean-field-theory used in statistical physics. We assign a weighting to each particle in order to have everywhere in the simulation, at least in the beginning, the same density of macro-particles.

Let us now understand how the Maxwell equations (page 27) are solved. By rewriting Maxwell (MW 2) and (MW 3) we directly see how the electric and magnetic fields evolve in time:

$$
\begin{aligned}
\mu_0 \varepsilon_0 \frac{\partial \boldsymbol{E}}{\partial t} &= -\mu_0 \boldsymbol{J} + \nabla \wedge \boldsymbol{B} \\
\frac{\partial \boldsymbol{B}}{\partial t} &= -\nabla \wedge \boldsymbol{E}
\end{aligned}
\tag{4.1}
$$

When using Maxwell (MW 1) and (MW 2) instead, the continuity equation can be found. The opposite way round this means that as long as the charge density satisfies the continuity equation then Gauss's law (MW 1) holds as well.[40] Therefore, (MW 1) no longer needs to be considered. Since there is no magnetic charge initially, (MW 4) remains true throughout the running simulation and can also be ignored.[61] The problem at hand is therefore reduced to Eq. set (4.1).

Another important feature of PIC codes is the ability of parallelisation.The reason why parallelisation is possible lays in the "locality" of the PIC algorithm which comes from the fact that the Maxwell equations have an absolute future and absolute past.[63] Indeed, while the simulation front moves through the simulation window at each step only information among the nearest neighbours is exchanged.

4.2.1 Quasi-Static PIC Code

As mentioned above Lcode is a quasi-static code who separates the fast timescale of the plasma and the slow timescale of the of the driver beam.[1] It is useful to introduce new variables for these two scales which will be used here after:

$$
\begin{aligned}
\tau &= t \\
\zeta &= z - ct
\end{aligned}
\tag{4.2}
$$

where t denotes the real time, τ the time of the driver (slow timescale), ζ the time of the plasma response (fast timescale), z the downstream position and c the speed of light respectively the speed of the driver. Note that, as here implied ζ can also be seen as a length scale (i.e., as the longitudinal position inside the bunch), connected to time through the speed of the beam. The same is true for τ which can actually be seen as the downstream position $z = c\tau$. Once the simulation over the simulation window governed by ζ is done, we can advance the driver with a large time-step in τ. Since the propagation of the fields is not modelled during this advance no data about radiation can directly be provided by a

---

[1]The conference proceeding paper by Pukhov [61] provides a very good overview over PIC codes and their working principle. The ideas in this section are based on this paper, however the equations are presented in more detail and in SI-convention instead of the cgs convention to provide uniformity in this work.

quasi-static PIC code. Let us write Eq.(4.1) in the times of Eq.(4.2) (neglecting the slow time τ):

$$\mu_0 \varepsilon_0 c \frac{\partial \boldsymbol{E}}{\partial \zeta} = \mu_0 \boldsymbol{J} - \nabla \wedge \boldsymbol{B}$$
$$c \frac{\partial \boldsymbol{B}}{\partial \zeta} = \nabla \wedge \boldsymbol{E}$$

(4.3)

The Magnetic Field   Now, the electromagnetic equations governing the quasi-static code shall be found: Taking the curl of Ampere's law (first equation in Eq.(4.3)) – remembering that spatial and time derivatives can be exchanged – one finds:

$$\mu_0 \varepsilon_0 c \frac{\partial}{\partial \zeta} (\nabla \wedge \boldsymbol{E}) = \mu_0 \nabla \wedge \boldsymbol{J} - \nabla(\nabla \wedge \boldsymbol{B})$$
$$= \mu_0 \nabla \wedge \boldsymbol{J} - \nabla \underbrace{(\nabla \cdot \boldsymbol{B})}_{=0 \text{ (MW 4)}} + \nabla^2 \boldsymbol{B}$$

(4.4)

Now, by taking the partial derivative with respect to ζ of the Faraday law (second equation in Eq.(4.3)) we can replace the curl of the electric field on the left-hand side of Eq.(4.4). The modified Faraday law from Eq.(4.3) is written as:

$$c \frac{\partial^2}{\partial \zeta^2} \boldsymbol{B} = \frac{\partial}{\partial \zeta} (\nabla \wedge \boldsymbol{E})$$

(4.5)

Putting (4.5) in (4.4) we find:

$$\nabla^2 \boldsymbol{B} = \frac{\partial^2}{\partial \zeta^2} \boldsymbol{B} - \mu_0 \nabla \wedge \boldsymbol{J}$$

(4.6)

And by focusing on the transverse direction of the B field only:

$$\nabla_\perp^2 \boldsymbol{B} = -\mu_0 \nabla \wedge \boldsymbol{J}$$

(4.7)

The Electric Field   In order to find the analogous relations for the electric field it is easiest to come back to Gauss's law (MW 1) on page 27. After taking the gradient of it and using Eq.(B.6) we get:

$$\nabla(\nabla \cdot \boldsymbol{E}) = \nabla \frac{\rho}{\varepsilon_0}$$
$$\nabla^2 \boldsymbol{E} + \nabla \wedge (\nabla \wedge \boldsymbol{E}) = \nabla \frac{\rho}{\varepsilon_0}$$

(4.8)

Which can be rewritten using Eq.(4.3) as:

$$
\begin{aligned}
\nabla^2 \boldsymbol{E} &= \frac{1}{\varepsilon_0}\nabla\rho - \nabla \wedge (\nabla \wedge \boldsymbol{E}) \\
&= \frac{1}{\varepsilon_0}\nabla\rho - \nabla \wedge \left(c\frac{\partial \boldsymbol{B}}{\partial \zeta}\right) \\
&= \frac{1}{\varepsilon_0}\nabla\rho - c\frac{\partial}{\partial \zeta}(\nabla \wedge \boldsymbol{B}) \\
&= \frac{1}{\varepsilon_0}\nabla\rho - c\frac{\partial}{\partial \zeta}\left(\mu_0 \boldsymbol{J} - \mu_0\varepsilon_0 c\frac{\partial}{\partial \zeta}\boldsymbol{E}\right) \\
&= \frac{1}{\varepsilon_0}\nabla\rho - \mu_0 c\frac{\partial}{\partial \zeta}\boldsymbol{J} + \frac{\partial^2}{\partial \zeta^2}\boldsymbol{E}
\end{aligned}
\tag{4.9}
$$

where we have used $c^2 = \frac{1}{\varepsilon_0\mu_0}$. Splitting this equation into a transverse and a longitudinal part we find the final result:

$$
\begin{aligned}
\nabla_\perp^2 \boldsymbol{E}_\perp &= \frac{1}{\varepsilon_0}\nabla_\perp\rho - \mu_0 c\frac{\partial}{\partial \zeta}\boldsymbol{J}_\perp \\
\nabla_\perp^2 E_\parallel &= \frac{1}{\varepsilon_0}\frac{\partial}{\partial \zeta}(\rho - \mu_0 c J_\parallel)
\end{aligned}
\tag{4.10}
$$

In a typical quasi-static PIC code the charge density and currents generated by the proton beam on the numerical grid are gathered and used as sources for equations (4.7) and (4.10). Then, a layer of plasma particles is generated and passed along the simulation window (from the beam front to its back) of the timescale ζ.

With help of the above quasi-static equations the corresponding fields are found. Once we arrive at the end of the simulation window all fields are gathered and the equation of motion for the beam particles in the calculated electromagnetic fields are found.[61] During the time-step $\delta\tau$ (large timescale) the beam particles are then pushed to their new positions and the updated momenta are assigned.

4.3 Simulation Setup

Before starting with simulations, the parameters space within which these are performed needs obviously to be defined. The framework conditions are given by the baseline parameters of the AWAKE experiment, the working conditions, and our scientific interest. The baseline parameters are cited in most of the papers published and are used for electron acceleration. In the experiment, for example, on a daily base working conditions with a lower plasma density are used to save rubidium. We define three parameter sets for which reproducibility and convergence of the simulations were tested, see Tab.4.1.

4.3.1 Particularities of Lcode

Throughout this and the following sections it may be useful to refer to Fig.4.1, which explains figuratively the concept of quasi-static PIC simulations and defines some parameter used in Lcode.
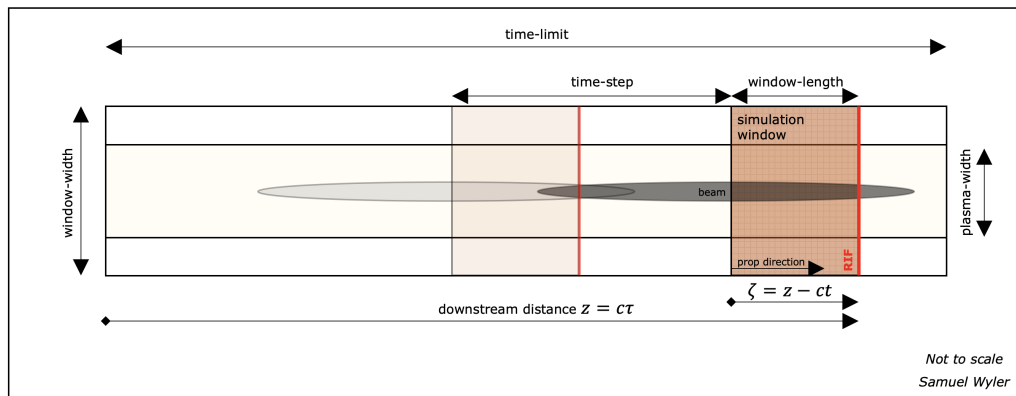
Figure 4.1: Drawing of the working principle of Lcode in the framework of the performed simulations. The *window-width* and *plasma-width* are the two important widths in Lcode. The first one defines the width over which the simulation grid is spread before the perfectly conducting walls begin. The second defines the width over which plasma-ions and -electrons are found. The *simulation window* (orange box) represent the "short timescale". At each time step $z_i = c\tau_i$ the simulations run from the red edge of the simulation window backwards the end. The red edge is in the experiment given by the relativistic ionisation front (*RIF*). Once the simulations at τ_i are done the beam particles are propagated forward by a time (or distance) defined by *time-step* to τ_{i+1} where the next simulation takes place. This procedure is repeated until the *time-limit* is reached.

Lcode is a free to use but not open-source code developed under the lead of Konstantin Lotov.[60] Lcode is designed as *2d3v* code, which means that it resolves two spatial dimension and three dimensions in momentum, or analogously, velocity space. Lcode works in either plane or axis-symmetric (cylindrical) geometry.[64] The code is quasi-static, and the calculation of the fields is therefore separated from the propagation of the beam particles as described in section 4.2.1. The plasma in front of the beam is considered as unperturbed and the walls are perfectly conducting.[2] The entire code deals with normalised quantities, see Tab.A.1 in the appendix. As mentioned Lcode has a wide range of setup options. The parameters used for the simulations are described in detail in Tab.4.1. Seeding as it is done in the experiment (section 3.4) is mimicked by an abrupt step from no-beam to having beam present.

4.3.2 Simulation Set Parameters

First of all, note that the initial proton beam (bunch) is created by an external PYTHON script and not by Lcode. Most of the parameters described in Tab.4.1 are needed to perform the initial beam creation. The lower part of the table then discusses the more technical values of how the simulations are performed.

Outputs Simulations done by Lcode have multiple available outputs. We are not interested in all of them and sort useful outputs into two categories: At first the longitudinal electric field $E_z(r_{ax})$, on-axis electron density $n_e(r_{ax})$ and on-axis beam charge density $\rho_b(r_{ax})$[3]. Then, a second category where the beam, meaning the important parameters of each macro-particle, per time-step is provided as output. The parameters given for macro-particle i at time-step τ_j are: The position ζ^i inside the simulation window at time-step τ_j,

---

[2]The Lcode manual [64] is available at https://lcode.info. Some papers related to Lcode are [60, 65, 66].
[3]In Lcode defined as *nb*.

Parameter	S-Set 1	S-Set 2	S-Set 3
Particles per bunch	3×10^{11}	2.83×10^{11}	3×10^{11}
Momentum [GeV/c]	400	400	400
Momentum spread (1σ) [GeV/c]	3.5×10^{-4}	3.5×10^{-4}	3.5×10^{-4}
Lorentz factor γ	426	426	426
Trans. bunch size σ [μm]	100-1000	150/320/560	200-900
Bunch length σ_z [cm]	7	7	12
Norm. emittance ϵ [mm mrad]	3.6	2.3/3.8/9.5	3.5
Waist position w.r.t. plasma entrance	0	0	0
Plasma density n_0 [1/m^3]	1×10^{20}	1×10^{20}	7×10^{20}
Ionisation Front [σ]	-1	-1.4/-1.4/-0.75	-1
Macro-particles	1×10^8	1×10^8	1×10^8
Space-step [k^{-1}]	0.005	0.01	0.01
Time-step [ω_p^{-1}]	100	100	100
Window length [k^{-1}]	600	600	1200
Window width [k^{-1}]	8	8	10

Table 4.1: Description: **S-Set1**: Standard experimental conditions; **S-Set2**: Parameters space to imitate experiment; **S-Set3**: Awake baseline design parameters for electron acceleration (trans. size scan). Refer to Fig.4.1 which provides a drawing of how the simulations are performed – including the parameter names.

the radial position r^i, the corresponding momenta p_z^i, p_r^i, p_a^i where the last is an auxiliary momentum necessary to do the conversion to Cartesian coordinates. Furthermore, the macro-particles' charge q^i, weighting w^i and particle identification number N^i are provided.

4.4 Pre- and Post-processing

Simply running a code is obviously not enough if we want to compare and analyse our simulations with the experiment. The initial beam creation is also described in this section.

4.4.1 Initial Beam Creation

The simulated beam is created by a PYTHON script[4]. The beam needs to be prepared in two dimensions in cylindrical coordinates.

It is helpful to recall some physical definitions. Let p_x (p_y) and p_z be the transverse and longitudinal momenta of a beam particle. The angle between these two quantities can be simplified if $p_z \gg p_x$: $x' = \arctan \frac{p_x}{p_z} \approx \frac{p_x}{p_z}$

Including relativity, the following development must be done:

$$
\begin{aligned}
p_x = mv_x = m\frac{dx}{dt} &= m\frac{dx}{dz}\frac{dz}{dt} \\
&= m_0 c\beta\gamma x'
\end{aligned}
\tag{4.11}
$$

where from the first to the second line we use that $\frac{dx}{dz} \approx \arctan(dx/dz) = x'$. Furthermore,

---

[4]The initial script was originally written by *Dr John Farmer* and was explained and made available to me in one of many *private communications, spring 2022*. I modified the script according to my requirements.

the relativistic γ factor has been added since the momentum is relativistic. Note that it is advantageous to see the step from line one to line two as going from a non-relativistic to a relativistic description with $m = m_0$ the rest mass. Considering $m \geq m_0$ instead can be misleading since the rest mass is an intrinsic property. A plot showing x versus x' is called trace-space.

When considering all individual particles together we can move to the statistical description of the beam. Here the definition of the emittance is of particular interest. The emittance is:[5]

$$\epsilon_x = \sqrt{(< x^2 >< x'^2 > - < xx' >^2)} \tag{4.12}$$

where the usual conventions are used:

$$\sigma_x^2 = < x^2 > = \frac{1}{N} \sum_{i=1}^{N} x_i^2 \tag{4.13}$$

$$\sigma_x'^2 = < x'^2 > = \frac{1}{N} \sum_{i=1}^{N} x_i'^2 \tag{4.14}$$

$$\sigma_{xx'} = < xx' > = \frac{1}{N} \sum_{i=1}^{N} x_i x_i' \tag{4.15}$$

Note that the last term in (4.12) becomes zero whenever position and angle are uncorrelated. This is the case at the waist of the beam. In this case:

$$\sigma_{x'} = \frac{\epsilon_x}{\sigma_x} \tag{4.16}$$

Now assume, that one would like to create a beam consisting of macro-particles but only statistical properties, such as the emittance, are given. For the following development we focus on the radial momenta of the particles. Assuming position and momentum are normally distributed one has: $p_r \sim \mathcal{N}(\mu_{p_x}, \sigma_{p_x}^2)$. According to Eq.(4.11) the momentum of the particle p_{x_i} is only up to an independent factor different from the angle x_i'. Therefore: $x_i' \sim \mathcal{N}(\mu_{x'}, \sigma_{x'}^2)$. Indeed, following the rules of transforming distributions we find the relation connecting the statistical property of the transverse momentum and the transverse angle[6]; the outcome is the sigma of the radial momentum distribution which is needed for the initial beam creation:

$$\begin{aligned} \sigma_{p_x} &= m_0 c \beta \gamma \frac{\epsilon_x}{\sigma_x} \\ &= m_0 c \beta \gamma \frac{\epsilon_{n,x}}{\beta \gamma \sigma_x} \\ &= \frac{\epsilon_{n,x}}{\sigma_x} m_0 c \end{aligned} \tag{4.17}$$

where Eq.(4.16) and Eq.(2.5) from chapter 2 have been used.

Finally the position distribution as well as the longitudinal momentum distribution needs to be discussed. The latter is likewise normally distributed with a sigma given by

---

[5]Definition taken from the lecture notes of "Introduction to particle accelerators" given by *Prof Mike Seidel* and *Dr Tatiana Pieloni* at EPFL, Lausanne. The emittance is sometimes also defined with an additional factor of 4 as it is done in the work of Buon.[67]

[6]See section B.1 in the appendix for the mathematical development.

the momentum spread σ_{p_z} which can be found in Tab.4.1. Therefore, $p_z \sim \mathcal{N}(E, \sigma_{p_z}^2)$, where $E = 400\,\text{GeV}$ and $\sigma_{p_z} = 3.5 \times 10^{-4}\,\text{GeV}$ is kept during the entire work. Note that these values need to be converted from eV to Lcode units by multiplying by $\left(\frac{e}{mc^2}\right)$.

Position Distribution   Finally, the distribution of the macro-particles' positions needs to be discussed. The radius is Rayleigh distributed; it can be shown that the normal vector $r = \sqrt{x^2 + y^2}$ of a two-dimensional normal distribution is Rayleigh distributed if the random variables $x \sim X$ and $y \sim Y$ are independent from each other.

Along the longitudinal direction for the position z a uniform distribution is chosen in order to have everywhere in the beam the same macro-particle density. To each macro-particle, however, a weight is assigned. This weight is defined according to the slice charge density in such a way that a weighted histogram of the z coordinates is truncated normal distributed and has a standard deviation corresponding to the bunch length σ_z.

Cut position   In the simulations done for this work the relativistic ionisation front (RIF) is mimicked by an abrupt start of having macro particles present. The position of this mimicking RIF is called the *cut position* and is given as the sigma position with respect of the beam length and beam centre. Furthermore, we define small gap between the start of the simulation window and start of the simulated beam. This gap is consistently chosen to be $1\,\text{k}_\text{p}^{-1}$.

4.4.2   Conversion to Cartesian Coordinates

Lcode is a two-dimensional code. For humans it is, however, often tedious to obtain a good understanding of the physics in two-dimensional cylindrical coordinates (r, z). It is more natural for us to look at plots or images which use Cartesian coordinates. Furthermore, when simulations are compared to the experiment, all measurements are a priori taken in Cartesian coordinates (and only then converted in another system).

In practice before converting the positions and momenta of the macro-particles to Cartesian coordinates, the set of particles is either up- or down-sampled. The up-sampling approach is well-justified, knowing that each macro-particle can be seen as a bunch of many real particles. The down-sampling on the other hand is, on desktop computer, a necessity to process the data.

However, random additional information is added when going to Cartesian coordinates. Consider the well-known equations to convert cylindrical coordinates into Cartesian coordinates:

$$\begin{aligned}
x^i &= r^i \cos \theta^i \\
y^i &= r^i \sin \theta^i \\
\zeta^i &= \zeta^i
\end{aligned} \tag{4.18}$$

The additional dimension arises from the θ used in Eq.(4.18). We use $\theta^i \sim \mathcal{U}_{[0,2\pi[}$. The

momenta need to be transformed as:

$$p_x^i = p_r^i \cos \theta^i + \frac{p_a^i}{r^i} \sin \theta^i$$
$$p_y^i = p_r^i \sin \theta^i - \frac{p_a^i}{r^i} \cos \theta^i \quad (4.19)$$
$$p_\zeta^i = p_\zeta^i$$

where p_r, p_z are the radial and longitudinal momenta, and p_a the third momentum perpendicular to the two others. In the convention of Lcode it needs to be normalised by r. It is also called auxiliary momentum.

4.4.3 Propagation in a Drift Space

After leaving the plasma the bunch travels in the experiment about $3.5\,\text{m}$ in a drift space before arriving at the streak camera. To reach image station 1 (IS1) this distance is $2\,\text{m}$ and for image station 2 (IS2) $10.14\,\text{m}$. When simulating the bunch, the same has to be done with the macro particles. The following procedure is used to do this:

$$x_{prop} = x_0 + v_x \Delta t$$
$$y_{prop} = y_0 + v_y \Delta t \quad (4.20)$$

where the coordinates with the index *0* denote the coordinates before propagation and x_{prop} and y_{prop} the propagated coordinates. The propagation time Δt as well as the propagation velocity v_x and v_y seen from the laboratory frame are found with Eq.(4.21). Here some special relativity theory, the proton mass m_p, the Lorentz factor γ and the particles transverse momenta are used:

$$\Delta t = \frac{\Delta s}{c\sqrt{1 - \frac{1}{\gamma^2}}} \qquad v_x = \frac{p_x}{m_p \gamma} \qquad v_y = \frac{p_y}{m_p \gamma} \qquad (4.21)$$

## 4.5 Convergence and Reproducibility

This section is dedicated to two types of studies that are conducted to find a reliable parameter space for all further results. In contrast to the well-known convergence studies, reproducibility studies must also be carried out in our case. These are necessary because the initial beam creation is not purely deterministic. In fact, the macro-particles in the initial beam are only distributed according to predefined statistical (macro-) distributions. However, the positions and momenta of individual particles inside these distributions are random. Two simulations with identical statistical setup may therefore lead to two different results. This difference can be of a magnitude that is relevant for us. This can also be put more in the context of the self-modulation instability. The unseeded SM grows from noise and is therefore highly sensitive to micro-distributions inside the proton bunch. In the performed simulations we are always in the seeded SMI regime since the proton beam noise is not characterised well enough to be simulated. Nevertheless, the growth of th SM can change from simulation to simulation even if the macro-statistical properties are kept the same. This is especially the case when the density of the macro-particles in the simulation

is too low. Therefore, the simulations are as well sensitive to micro-distribution inside the beam.

The output parameter that is used to verify the reproducibility is the longitudinal on-axis wakefield E_z; the parameters which are optimised are the number of macro-particles N, the grid-steps dr and dz, and the time-steps.

In order to verify the reproducibility of the results in the chosen parameter space the same simulation is run five to ten times with identical statistical properties. The corresponding result is shown in Fig.4.2a.

In order to verify the reproducibility at different positions in the simulation window, the latter is split into sub-ranges or slices of equal thickness of $\Delta\zeta = 6\,\mathrm{k_p^{-1}}$. Its position is given in σ_t with respect to the proton bunch centre. As before negative values indicates position ahead of the centre. For each slice of interest, a graph of the average maximum electric field E_z over all runs as a function of the bunch position z in the plasma is plotted (Fig.4.2b). The standard deviation of the maximum electric field as a function of the position z is shown as a shaded area. An example of this is shown in Fig.4.2b. This point
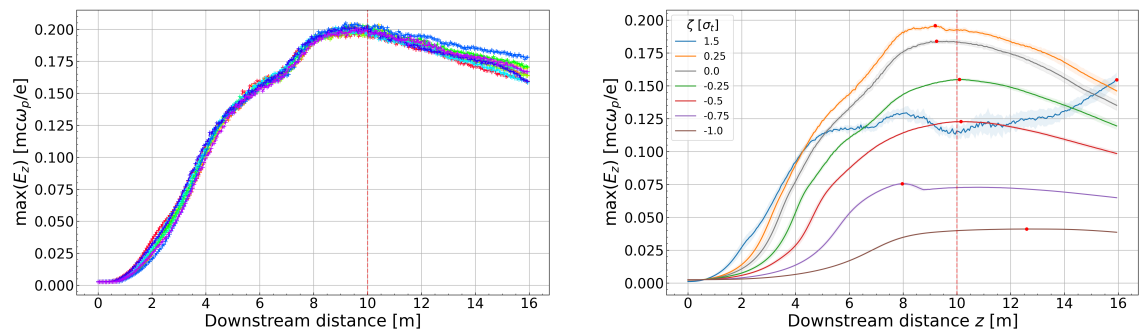
(a) Overall electric field maxima in the full simulation window as a function of the bunch position z in the plasma. In total ten simulations with statistically identical setup parameters are plotted.

(b) Mean electric field maxima in six narrow slices of interest in the simulation window. Shaded envelopes represent the standard deviation over ten simulations. Slice position σ_t with respect to the centre of the bunch. The maximum in each slice is marked with a red dot.

Figure 4.2: Reproducibility study with parameters **S-Set2** in Tab. 4.1 and A.2. The transverse beam size at the plasma entrance is set to $330\,\mu\mathrm{m}$. The red dashed line represents the end of the vapour cell in the experiment.

of maximum field is also called the *saturation point*. We will see in the results chapter in more detail the relationship between the initial transverse beam size and the position of saturation or the strength of the longitudinal electric field.

In Fig.4.3 the reproducibility of the largest beam in S-Set3 is shown. In general the reproducibility becomes worse with increasing beam size due to the reduced macro-particle density in the simulations. Here the most critical beam size of $900\,\mu\mathrm{m}$ is plotted. For the future work it is proposed to further increase the number of macro-particles in the simulation to obtain more reliable band-structure results, see section 6.4.3. The good reproducibility of S-Set 1 is presented over more than $30\,\mathrm{m}$ of simulation in Fig.4.4.

Concerning the convergence, parameter scans are performed and the convergence of the electric field E_z is verified. The order of convergence or reproducibility has not been
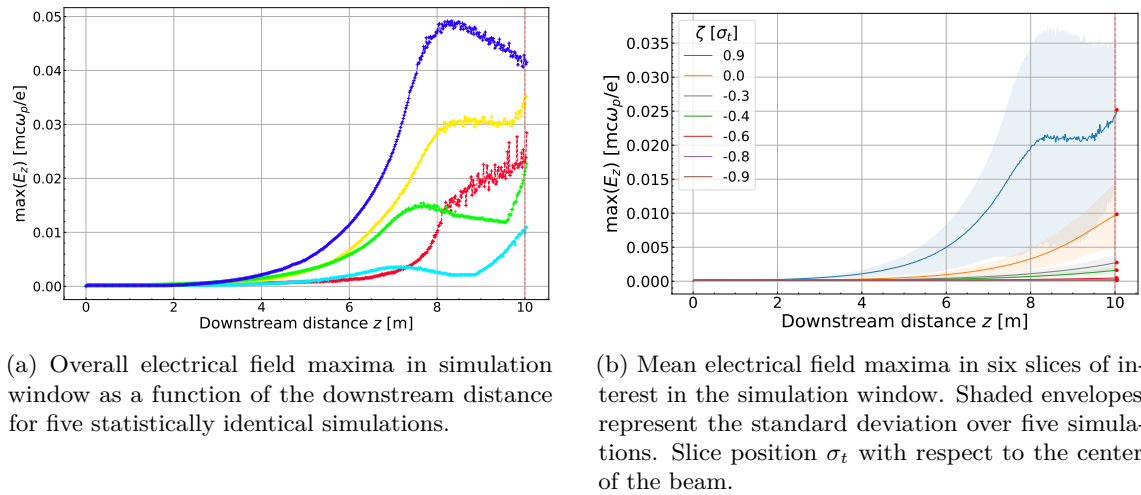
(a) Overall electrical field maxima in simulation window as a function of the downstream distance for five statistically identical simulations.

(b) Mean electrical field maxima in six slices of interest in the simulation window. Shaded envelopes represent the standard deviation over five simulations. Slice position σ_t with respect to the center of the beam.

Figure 4.3: Extended reproducibility study for a **S-Set 3** beam with $900\,\mu\mathrm{m}$ beam size at iris and $N = 1 \times 10^8$.

(a) Overall electrical field maxima in simulation window as a function of the downstream distance for five statistically identical simulations.

(b) Mean electrical field maxima in six slices of interest in the simulation window. Shaded envelopes represent the standard deviation over five simulations. Slice position σ_t with respect to the center of the beam.
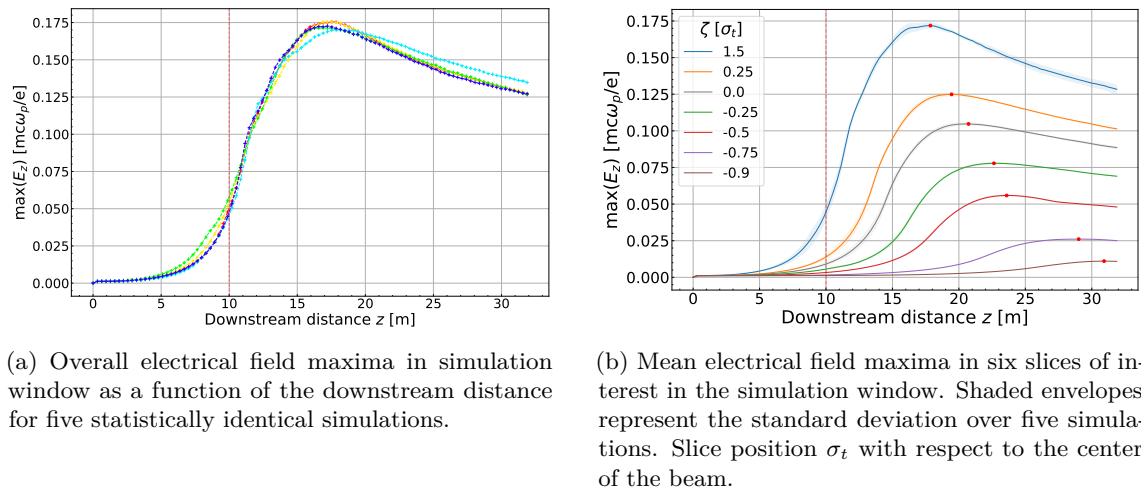
Figure 4.4: Extended reproducibility study for a **S-Set 1** beam with $1000\,\mu\mathrm{m}$ beam size at iris and $N = 1 \times 10^8$.

tested as it is not expected that convergence follows a simple function as a monomial or an exponential.

In order to understand the issue of reproducibility better, in Fig.4.5 convergence and reproducibility are shown together on on single plot. Again each line represents a slice in a given, short, ζ range. The mean of the maximum electric field E_z over all bunch positions z is found inside the slice and plotted as a function of the number of macro-particles N. The width of the shaded region is given by the standard deviation. Each set is repeated ten times with statistically identical input parameters.

A few things are interesting to see. First, it becomes clear that the overall highest electric field (saturation point) can be found somewhere in a slice in the range $\sigma_{t,max} \in [-0.25, 1.5]$. Second, the further we go in the front of the beam, the higher the reproducibility becomes (violet and brown line). The reproducibility of a slice close to the one where the saturation point is found, is only little affected by changing N (orange line). After the saturation point the reproducibility is again more strongly affected by N (blue line).
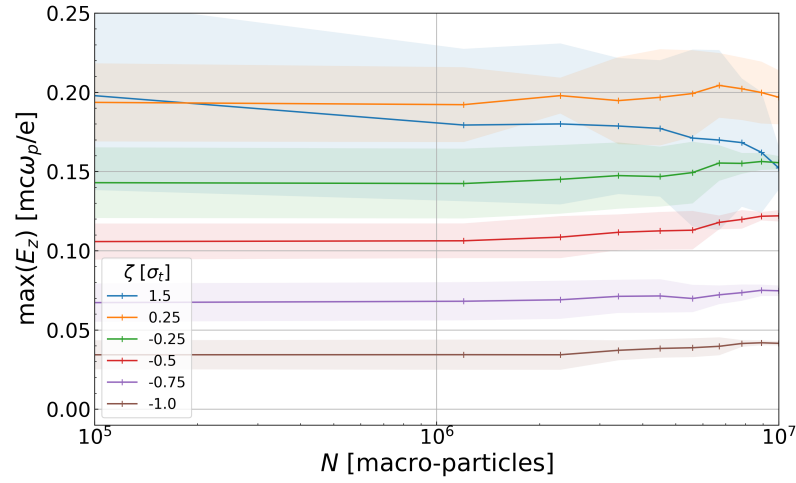
Figure 4.5: Convergence and reproducibility studied in one figure. Here ten sets of different numbers N of macro particles are simulated. Each set is repeated ten times to get a measure of the reproducible. Parameters are as described in **S-Set2** in Tab.4.1 ($330\,\mu m$ trans. beam size).

Finally, we see that for slices in front of the bunch centre there is no clear and simple convergence tendency with respect to N.

In a further benchmarking of Lcode, it would be interesting to choose even higher numbers of macro particles. However, in the framework of this thesis, the computational costs versus the outcome would have been out of proportion and not justifiable.

5 Experiment

In this chapter, the experimental setup for the plasma experiments conducted will be explained, as well as the streak camera system and some result analysis methods. Basic information about the different beamlines or the vapour source is given in section 1.1.2. Information about the image station cameras, which are also partly used for beam characterisation, can be found in section 2.2.1, with the only difference that for plasma experiments not only the CORE cameras but also the HALO cameras of the image stations are used. CORE and HALO cameras receive light from the same screen however the HALO cameras have a mask that covers the centre of the beam, making halo regions with lower signal intensity visible. For an overview of the placement of the image stations and the streak cameras, refer back to Fig.2.1.

5.1   Streak Camera

The streak camera used in the experiment is located between the two image stations at a distance of $3.5\,\text{m}$ from the end of the vapour source (plasma source). A streak camera takes time-resolved images of the signal generated when the p^+ bunch crosses the OTR screen. Time-resolved in this context means that the signal is spatially resolved along one axis and temporally resolved along a second; which results in a two-dimensional image. Since the p^+ bunch is highly relativistic and over a propagation distance of its own length only changes slowly, the temporal dimension can be converted into a spatial one ($\zeta = z_{streak} - ct$) where z_{streak} is the physical position of the streak camera.

The first component of a streak camera is a slit along the y-axis, in our case with a width (x-axis) of $20\,\mu\text{m}$ through which pass the photons emitted by the OTR screen. This width defines the spatial smearing of the final image. A second central component is the photocathode which converts the photons into electrons that are accelerated by an accelerating mesh in the streak-tube. Inside the tube a fast changing electric sweep field is applied by two electrodes and triggered by the arrival of the electrons. Electrons passing through the tube at different times experience a different electric field and are deflected differently along the x-axis – this enables high temporal resolution of the incoming signal. In a final step the electrons hit a phosphor screen which emits photons that can then be registered by a common camera sensor.[68]

To understand the orders of magnitude in the framework of AWAKE, let us consider the following. In the experiments conducted, the micro-bunch train due to the SMI or SSM is made visible by the streak camera; from theory we know that these micro-bunches occur periodically at a distance corresponding to the plasma wave length (see Eq.(3.17)).

Since we know that the bunch is relativistic ($\beta_{bunch} \simeq 1$), the frequency at which the micro-bunches cross the OTR screen is $\sim$(90 to 238) GHz, for a plasma electron density of $(1 \times 10^{14}$ to $7 \times 10^{14})$ cm^{-3}. These frequencies in turn correspond to a micro-bunch period of $\sim$(11 to 4.2) ps which defines the minimum requirement for the OTR screen and streak camera resolution. The temporal resolution of the OTR screen is assumed in [69] to be (0.2 to 2) ps, so it is appropriate to temporally resolve the micro-bunch structure. The streak camera used in AWAKE (Hamamatsu C10910-05) is also capable of providing this temporal resolution as was shown in [69].

When using the streak camera, different time-windows can be selected, we use a 1.134 ns (often called $\sim$1 ns window), 210 ps and a 73 ps window. The output is an image of 672 pixels along the y axis and 512 pixels along the time axis. The pixel-to-metric calibration along the spatial axis (y-axis) is 21.7 µm/px.[1] This would result in a final resolution range of $\sim$(0.14 to 2.2) ps, depending on the time-window. However, it turns out that when using a 1 ns time-window no micro-bunch structure is visible, although the micro-bunch period is $\sim$11 ps; see Fig.6.11b. It can thus be concluded that an increase of the time-window has negative consequences on the streak camera's time-resolution, probably due to a limitation of the sweep time.

5.2   Timing

In the AWAKE experiment, the different beams must be temporally tuned and spatially aligned. For this work, we have the advantage that one beam – the electron beam – is not used.

To regulate the position of the *relativistic ionisation front* (RIF) relative to the proton beam coming from SPS, a delay is defined between the SPS and AWAKE trigger.

Parallel to the RIF, a marker laser pulse is propagated, which can be delayed relative to the RIF. This distance between the RIF and the marker visible on the streak images can therefore be controlled and is always known, and it can also be sent without a "high-energy" RIF. Note, that the marker delay is purely physical and due to a so-called air-transition time, no electronic components contribute.

For each plasma experiment we take so-called *plasma OFF* streak images of the p^+ bunch, which means that the bunch propagates through the vapour source which becomes a drift space. Thereby we find the centre as well as the length and width of the p^+ bunch. This lets us calibrate the distance centre-to-marker and thus also centre-to-RIF distance. This reference measurement is necessary as the bunch length may vary from day to day. It is also assumed that the SPS-to-AWAKE trigger delay is subject to fluctuations that are significant for experiments. Based on these calibrations, the RIF position and the streak time-window position are determined during the experiment.

We distinguish two categories of experiments based on the assumed origin of self-modulation (SM) [35]:

---

[1]Based on *private communication, May, 2022* with *Dr Livio Verra.*

1. Modulation emerges from the self-modulation instability (SMI): The RIF is at $(-2.7$ to $-2.6)\,\sigma_t$ in front of the beam.

2. Modulation emerges from seeded self-modulation (SSM): The RIF is at $(-0.75$ to $-1.6)\,\sigma_t$ in front of the beam.

5.3 Analysis

5.3.1 Overlaying of Images

In the case of SSM, the signal density can be increased by overlaying streak camera images from several events. To do this however the individual images must be shifted to each other in such a way that the markers (and therefore also the RIF) of all images lie on top of each other. We do this by adding a padding in the length of the largest marker position difference to all images. Then we move them with respect to the marker positions. The so-called *waterfall* plots show the result of the image-shifting, see for example Fig.6.7.

The overlaid or sometimes also called stitched images are then created by summing all aligned single images together and dividing the resulting pixel intensity by the number of events present at that location. Thus, the average signal density along the time-axis is constant, although fewer events are summed at the ends of the streak image. The time-axis extents are found based on the calibration and the marker position.

5.3.2 Frequency and Phase of the Bunch Train

The easy way to understand if we are in the SMI or SSM regime is to look at the waterfall plots and to verify by eye if the micro-bunches of multiple events are in phase or not.

The more rigorous way is to find the frequency and the phase of the micro-bunch train of each event. The signal of interest consists in this case of a normalised projection onto the ζ-axis. The projection is only done over the core of the beam, the halo is ignored. To find frequency and phase, a Discrete Fourier Transform (DFT)[2] is applied. The DFT is defined as:

$$\hat{f}[m] = \sum_{n=0}^{N-1} f[n]e^{-i2\pi mn/N} \tag{5.1}$$

where $f[n]$ is the discrete signal, $\hat{f}[m]$ its transform, and N denotes the total number of samples.

However, by the definition of the DFT, Eq.(5.1), it is clear that the number of sample points of the transform is given by the number of points of the input. This presents us with the problem that if we want to find the modulation frequencies of different events that have frequencies close to each other, the frequency resolution may be too low. Pre-processing cannot add information to the signal, but we can make it more visible. For this reason, *zero-padding* is added to both sides of the signal to increase the total number of sample

---

[2]The Cooley-Tukey Fast Fourier Transform algorithm implemented in PYTHON's numpy package is used to calculate the DFT.

points.[3] By closer look at Eq.(5.1) one can see that the padding does not add to the sum, since $f[n_{padding}] = 0$. Indirectly, though, N, m and n change and so does the resolution of $\hat{f}$. The zero-padding can conclusively be seen as an interpolation of $\hat{f}$.[70]

Furthermore, to smooth the sharp change from original signal to zero-padding which can lead to artefacts in the DFT, the signal is convoluted with a Hanning window, also called Hann window.[71, 72] From the power spectrum then the frequency of the first harmonic is chosen for each event.

When comparing the phases, there is one detail to keep in mind[4]: the phases can only be compared between signals of the same frequency. If this is not the case, a comparison of the phases involuntarily no longer makes sense. If we take two sinusoidal functions of different frequencies but "in phase" at $t = 0$, at almost any other time the two signals are out of phase because the frequencies differ (due to the periodicity, single frequencies can also be in phase at other times). For this reason, the phases of the average frequency of all events are compared.

---

[3]The *zero-padding* approach is inspired by *private communication, May, 2022* with *Dr Livio Verra.*
[4]Inspired by *private communication, 10th of June 2022* with *Dr Patric Muggli.*

6 Results and Discussion

In this chapter, the results of the numerical simulations as well as of the experiment are presented.

The parameter of interest that is the common thread throughout the thesis is the transverse beam size of the proton (driver) beam at the plasma entrance (iris). All other parameters are kept constant wherever possible to allow comparison. Within the framework of AWAKE, this is the first time that plasma experiments have been carried out with a proton (p^+) beam of different sizes. As explained in detail in the introduction (section 1.2), these are the first important results that shed light on whether or not RIF is suitable in a future Run 2c.

For the execution of a future Run 2c it is key to understand the dependency of the growth rate on the transverse beam size. Under specific assumptions about the beam profile (e.g., flat-top radial profile) the growth rate in the linear-regime of self-modulation (SM) is analytically provided by theoretical work as shown in Eq.(3.22) in section 3.3. In the experiment many of these assumptions no longer hold. The transverse and longitudinal beam profiles are for example in a first approximation best described by Gaussian distributions before the beam enters the plasma. However, in the plasma the beam shape may change in a complicated way which is not describable by linear theory. Also, the SM may, depending on the p^+ bunch size, leave the regime described by linear theory. For these reasons theory can give very important hints but not a conclusive description of the experiment. Numerical simulations that can handle the non-linear wakefield regime are a better approximation if the parameter space is chosen carefully. Simulation allows us to discover, describe and understand trends and phenomena. Nevertheless, we need to keep in mind that they remain a simplification of the reality and do not a priori have to match the results of the experiment.

In addition to the key experimental results for this thesis, further studies based on simulations will be presented as well. It is for example shown that for a p^+ bunch of $\sigma_{y,i} \sim 560\,\mu m$ there is good agreement of the micro-bunch structure between the experiment and simulations. Although less detailed, this can be seen as an addition to the work of Bachmann which compared the experiment with simulations for a standard p^+ beam according to the baseline design, see Tab.2.1 on page 9.[73]

Furthermore, in numerical simulations a p^+ bunch radial structure develops depending on the transverse beam size. These structures are shown in the transverse beam profiles after SM and resembles a band structure. This phenomenon is further enhanced with increased p^+ beam size.

6.1   Longitudinal Wakefields

The transverse wakefields are responsible for the SM of the proton beam. The longitudinal wakefields then arise due to this SM. Using numerical simulations, we can study the dependence of these longitudinal wakefields on the initial transverse p^+ bunch size. In Fig.6.1, we show for beams with transverse sizes of $\sigma_{\perp,i} = (100 \text{ to } 1000)\,\mu\text{m}$ the maximum longitudinal wakefields in the bunch as a function of the bunch position in the plasma. The vertical red dashed line indicates the end of the plasma source in the experiment. The plasma density is set to $1 \times 10^{20}\,1/\text{m}^3$ and the p^+ bunch has a length of $\sigma_z = 7\,\text{cm}$. Note that this chosen density corresponds to a density seven times lower than used for electron acceleration experiments. However, this density is often chosen for general plasma experiments and therefore all experimental results presented here were carried out at this density.
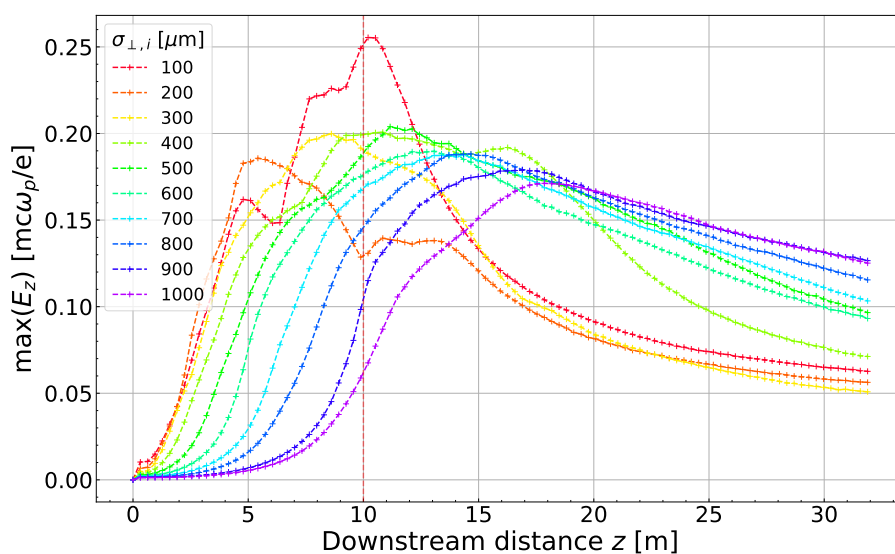
Figure 6.1: Maximum longitudinal wakefield E_z in the p^+ bunch as a function of the distance the bunch travelled in the plasma. Proton beams with initial transverse sizes $\sigma_{\perp,i} = (100 \text{ to } 1000)\,\mu\text{m}$ are plotted. The vertical red dashed line at $z = 10\,\text{m}$ indicates the end of the plasma source in the experiment. Parameter set **S-Set1** defined in Tab.4.1 is used.

We see that the longitudinal wakefields start growing later in the plasma the larger the initial transverse beam size is. The position at which the maximum longitudinal wakefield amplitude is reached is called the saturation point; after this point the wakefields start decaying. The decay is in general weaker the larger the initial beam is. The distance at which saturation is reached and the maximum wakefield amplitude also depend on the initial beam size. We see that a beam with $\sigma_{\perp,i} = 560\,\mu\text{m}$ would only reach saturation after the plasma source in the experiment. Such a beam is considered in the experiment (see next sections).

For the $\sigma_{\perp,i} = 100\,\mu\text{m}$ beam a first peak at $z \simeq 5\,\text{m}$ is reached. The wakefield growth then continues after a short phase of decaying. A similar, but less distinct, decay-rise phenomenon can also be identified for the $\sigma_{\perp,i} = 200\,\mu\text{m}$ beam. When the micro-bunch structure of such a small beam is considered at $z = 10\,\text{m}$ then two regions from where the transverse wakefields started growing can be observed. This is probably linked to the non-monotonic decay of the wakefields after a first pre-saturation. These phenomena

could be due to a phase shift of the transverse wakefields during the propagation in the plasma. A more detailed investigation of whether this phenomenon is also present in the micro-bunch structure in the experiment was not carried out.

Corrigendum   Also, the simulated beam with $\sigma_{\perp,i} = 500\,\mu m$ reaches the strongest longitudinal wakefields at the saturation point (when the $\sigma_{\perp,i} = 100\,\mu m$ is ignored). The plasma skin depth for the chosen plasma density is with $\sim 530\,\mu m$ similar to the transverse beam size of $500\,\mu m$. In simulations with other plasma densities and therefore other plasma skin depths a similar effect was found; in general, a beam with a transverse size similar to the plasma skin depth reaches the highest longitudinal field strength at saturation. Smaller beams can reach even higher field strength. However, the field growth before saturation is then often no longer monotonic.

6.2   Experimental Results of Self-Modulation Instability Studies

This section is dedicated to some of the key results of this work. As seen in the theory section (3.3) the growth rate of the bunch envelope during self-modulation mainly depends on the p^+ beam radius via its charge density, as long as the total population is kept constant. The proton bunch population in the here presented experimental results is kept constant at $(2.83 \pm 0.03) \cdot 10^{11}\ p^+$.

The unseeded self-modulation (SM) behaviour of three beams with increasing sizes are compared below. The measured transverse beam sizes in the y-direction at the vapour source entrance (iris) are: $\sim150\,\mu m$, $\sim330\,\mu m$ and $\sim560\,\mu m$. Throughout this chapter the y-direction will be focused on, since the streak camera profiles the beam along the y-axis.

Plasma OFF Case   Plasma OFF denotes the case when no laser pulse was sent into the vapour source to ionise the plasma. This means the vapour source can be considered as drift space. With plasma OFF the p^+ cannot self-modulate and is therefore always unmodulated. In the plasma ON case, both is possible; SM can happen but does not have to.
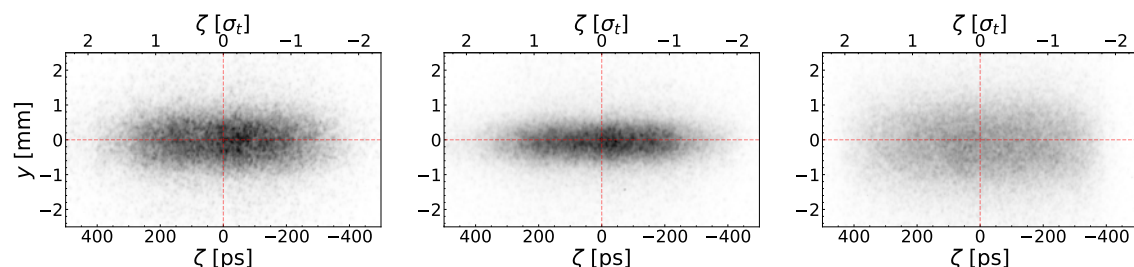

Figure 6.2: Time-resolved (ζ, y) images of three different sizes of unmodulated p^+ bunches after travelling $\sim13.5\,m$ in drift space from the iris to the streak camera. Sizes *at iris* $\sigma_{y,i}$ from left to right: $\sim150\,\mu m$, $\sim330\,\mu m$, $\sim560\,\mu m$. Note that the colour-scales of the three sub-figures are independent and should not be compared.

The appearance of the plasma OFF bunch on the streak camera ($\sim3.5\,m$ after the

vapour source exit and $\sim 13.5\,\text{m}$ after entrance) is shown in Fig.6.2. Note that the coordinate $\zeta = z/c - t$ is given in picoseconds and in units of the longitudinal bunch (beam) size σ_t, both with respect to bunch centre. The p^+ bunch is travelling from left to right. Therefore $\zeta < 0$ denotes a position in front of the bunch centre. The same convention is chosen in numerical simulations.

Already from visual inspection it is clear that the right-hand plot ($\sigma_{y,i} \sim 560\,\mu\text{m}$) shows the largest beam. Although the other two beam sizes appear reversed in comparison to their size at the iris after propagation of $\sim 13.5\,\text{m}$ in drift space, this can be explained using the beam size characterisation done in chapter 2 with results in Tab.2.3. We know that due to the higher beam divergence along the y-axis of the $\sigma_{y,i} \sim 150\,\mu\text{m}$ beam, after travelling $\sim 13.5\,\text{m}$ in drift space it will be larger than the initially $\sigma_{y,i} \sim 330\,\mu\text{m}$ sized beam. The bunch length and width given by the streak camera are noted down in Tab.6.1.

		Trans. Beam sizes at iris		
Parameter	**Unit**	**150 µm**	**330 µm**	**560 µm**
Bunch duration σ_t	ps	213	215	232
Bunch size $\sigma_{y,streak}$	mm	642	465	919
Bunch size $\sigma_{y,charact}$	mm	(540 ± 40)	(450 ± 30)	(925 ± 50)

Table 6.1: Proton bunch duration $\sigma_t = \sigma_z/c$ and transverse size $\sigma_{y,streak}$ determination at the streak camera, as well as estimated size $\sigma_{y,charact}$ from the beam characterisation (see chapter 2).

For the two p^+ beams of larger size $\sigma_{y,i}$ at the iris ($330\,\mu\text{m}$ and $560\,\mu\text{m}$), a good agreement between calculation from the beam characterisation and the measurement at the streak camera is found. For the standard (baseline design) beam of $150\,\mu\text{m}$ transverse size this is not the case. The reason for this may lie in in the fact that the beam characterisation was performed on a different day than the plasma experiments. A different day has been chosen because the same-day characterisation showed inconclusive results for the standard beam – no explanation for this could be found (see section 2.4.1). However, even if we use this (inconclusive) characterisation data acquired on the same day the difference persists and becomes even bigger, while the beam size at the iris is measured being larger ($\sim 240\,\mu\text{m}$).

In the end it was therefore decided to use the well-established standard beam characterisation which was also confirmed in previous studies. The fact that the real SMI results may be based on a larger beam size than assumed is less problematic than the converse. This is because then the difference in the growth rate of the smallest and largest considered beam, which we intend to show, would even be larger.

6.2.1   Absolute Bunch Envelope Growth Rate

A first qualitative measure of the SMI growth is found by considering the *bunch* envelope (not beam envelope) after the bunch has travelled through $10\,\text{m}$ of plasma. To be clear, when talking about the bunch envelope in this context, the structure of the bunch itself at $\zeta = z/c - t$ at the fixed position of the streak camera $z = z_{streak}$ is considered, rather than the properties of the entire bunch moving some distance Δz. The bunch envelope

we intend to measure is the defocused part of the bunch, which is often denoted as the *halo*. However, on a 1 ns time window streak image one is not able to distinguish the alternating focused and defocused regions; what remains is a time-resolved structure that can be described as a function of ζ.

This bunch envelope is found for each time slice of the time-resolved image. In particular the y-axis values $r_{y,+}(\zeta)$ and $r_{y,-}(\zeta)$ for which:

- For the upper half-plot $(y > r_0)$ 20% of the upper-half cumulative signal lays above,

- For the lower half-plot $(y < r_0)$ 20% of the lower-half cumulative signal lays beneath,

are found.

Mathematically this is defined similarly to a quintile, by finding $r_{y,+}(\zeta)$ and $r_{y,-}(\zeta)$ such that:

$$\int_{r_0(\zeta)}^{r_{y,+}(\zeta)} dy\, S(y) = q = 0.8$$
$$\int_{r_{y,-}(\zeta)}^{r_0(\zeta)} dy\, S(y) = q = 0.8 \tag{6.1}$$

where the reference position $r_0(\zeta)$ is re-determined for each time slice and $S(y)$ denotes the signal at position y.[1] Mathematically the reference position $r_0(\zeta)$ corresponds to the median of the cumulative sum:

$$\int_{-\infty}^{r_0(\zeta)} dy\, S(y) = \int_{r_0(\zeta)}^{\infty} dy\, S(y) \tag{6.2}$$

In what follows we shall call $r_y(\zeta) = \{r_{y,-}(\zeta), r_{y,+}(\zeta)\}$ the 80 % bunch envelope. This bunch envelope can be seen as a simplified measure of the bunch *halo*, while the bunch *core* can be defined as the radial extent of the micro-bunch train.

However, at the ends of the time-resolved images the values of $r_{y,+}(\zeta)$ and $r_{y,-}(\zeta)$ become misleading, and would imply the bunch is diverging. This effect is not physical and appears due to the decreasing signal-to-noise ratio at the extremities. Without any signal the lines would be found such that 20% of the pixels lay above the upper, and 20% would lay beneath the lower line given by $r_y(\zeta)$. In Fig.6.3 the raw results of this procedure applied to streak camera images can be considered for all three beam sizes.

The larger the initial beam radius, the later in the bunch the SMI process seems to start. Strictly speaking, no precise statement can be made about the exact starting point of SMI from 1 ns windowed images. This is because, according to Eq.(3.21), the growth of the bunch envelope in the linear regime of SMI is similar to the exponential of the growth rate $\Gamma(\zeta, z, \dots)$. Therefore, SMI can start long before it becomes experimentally visible on a 1 ns window image. Only when the "explosive" exponential behaviour begins, does

---

[1]One may argue that since $S(y)$ is not continuous a discrete definition should be used. However, $S(y)$ can be integrated piece-wise since for each pixel a Riemann sum can be taken. The continuous definition is therefore valid.
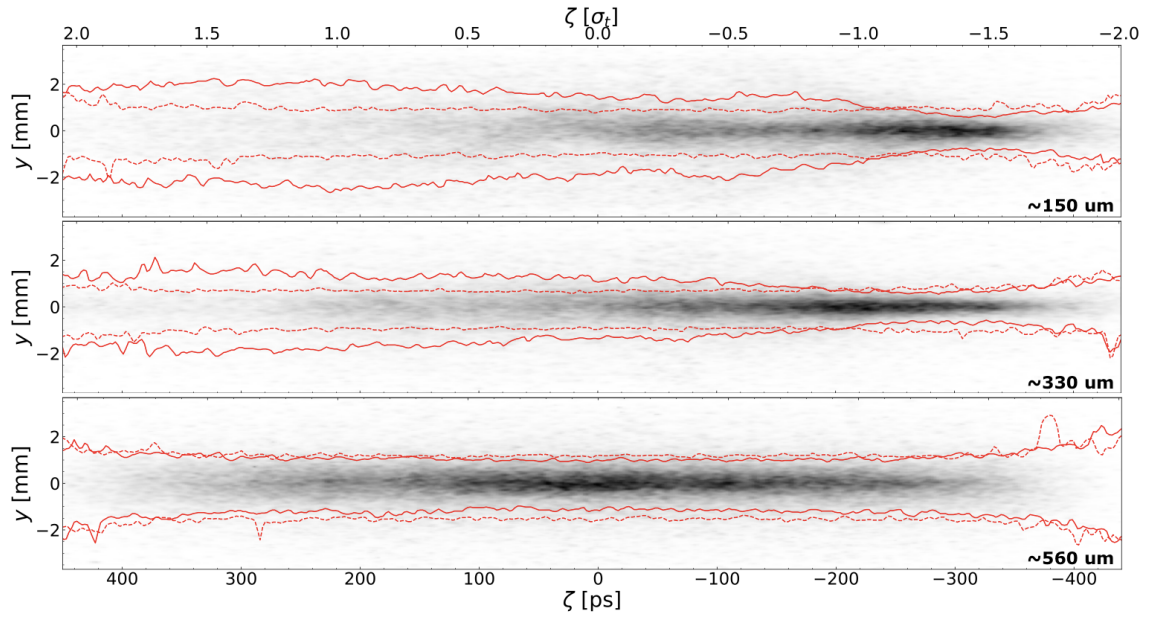
Figure 6.3: Time-resolved (ζ, y) images of p^+ bunches of beam sizes at iris (top to bottom) of $\sim150\,\mu m$, $\sim330\,\mu m$ and $\sim560\,\mu m$. The RIF is positioned at $(-2.72$ to $-2.61)\,\sigma_t$. The solid red lines show the $80\,\%$ bunch envelope of a plasma ON and the red dashed lines the $80\,\%$ bunch envelope of a plasma OFF bunch. The bunch spread in the front is non-physical and due to a low signal-to-noise ratio. Each image has its own colour-scale.

the bunch envelope change move into the measurable range. Also, in the establishment regime of SMI, multiple self-modulation phases may be superimposed until eventually the "strongest" SM phase wins over the others and starts dominating the SM process. In this regime of strongest-phase competition, the plasma will already be out of its equilibrium and unstable. Therefore, SMI has already started without unique SM being visible. After a while the strongest phase will control the phase of SM and the feedback process between transverse wakefields and SM is established, thus the micro-bunches start appearing.

Besides the delayed "visible" starting point of SMI, the $80\,\%$ bunch envelopes of the different beam sizes also differ in their spread over time. In Fig.6.4 the bunch envelopes of the three different beams are compared.
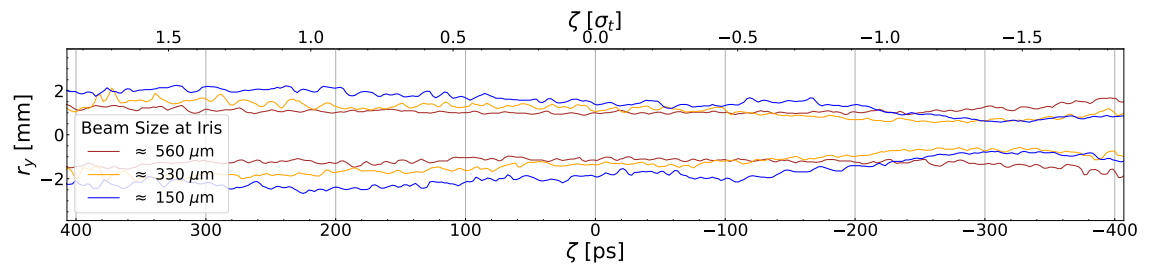
Figure 6.4: Condensed $80\,\%$ bunch envelope results of Fig.6.3. The bunch centre is at $\zeta = 0$, the RIF is $(-2.72$ to $-2.61)\,\sigma_t$ ahead the centre.

6.2.2 Relative Bunch Envelope Growth Rate

The presentation of the raw bunch envelope curves above does not reveal all physics of interest. In particular the relative growth of the $80\,\%$ bunch envelope lines with respect to

the initial beam size remains to be discussed but also adiabatic focusing can be highlighted more.

Adiabatic Focusing Adiabatic focusing can be seen in Fig.6.3 when comparing the plasma ON (solid red line) and plasma OFF (red dashed line) bunch with each other. For the time slices ζ where the plamsa ON bunch has a smaller envelope than in the plasma OFF one, the bunch is in an adiabatic focusing regime as described in section 3.6. To make adiabatic focusing more obvious, and also to compare the three beams on one plot, the 80 % bunch envelope r_y for all three beam sizes is dynamically normalised to its ζ-slice corresponding 80 % bunch envelope extent of the plasma OFF bunch $r_{off}(\zeta)$. Mathematically this corresponds to the fraction $\frac{r_y(\zeta)}{r_{off}(\zeta)}$ where r_y is now the average of $r_{y,+}$ and $|r_{y,-}|$.

The result of this operation is shown in the upper part of Fig.6.5. This procedure has the advantage that whatever the plasma OFF bunch size, a direct comparison between the plasma ON (SM possible) and plasma OFF case is available. For all beam sizes the plasma OFF case is the straight line $r_y/r_{off} = 1$.

Now we see that for all beam sizes the front of the bunch falls below the line $r_y/r_{off} = 1$. This means that this region is dominated by adiabatic focusing. Similar results were also obtained by Verra *et al.* in the framework of electron seeded self-modulation (e-SSM).[5]

For the two smaller beam sizes SMI gains the upper hand in the region $-1.4 < \zeta[\sigma_t] < -1.1$ and a widening of the bunch envelope (halo) becomes visible. However, for the 560 μm beam, adiabatic focusing remains the dominating force along the entire presented area ($-1.8 < \zeta[\sigma_t] < 1.8$). In general, the larger the beam at the iris, the later, if at all, the SMI provides the dominant transverse force. Qualitatively this trend is in accordance with theoretical predictions.
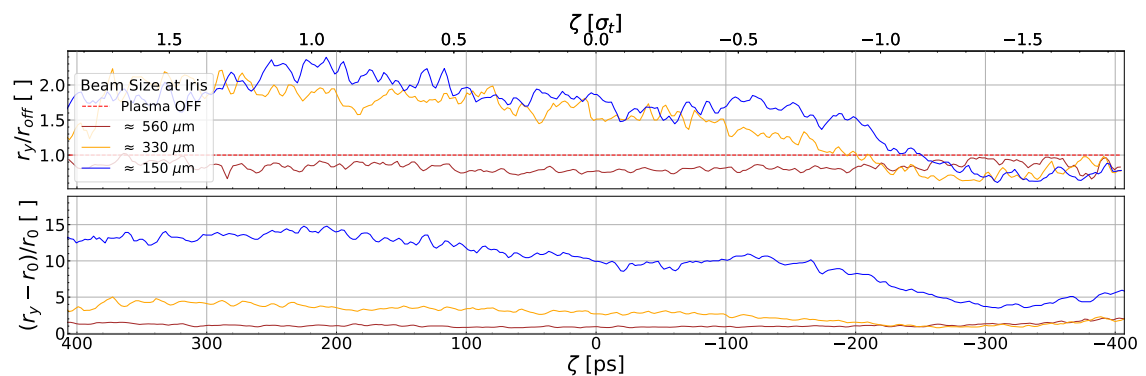

Figure 6.5: Top plot: bunch envelope dynamically normalised to the time-slice corresponding bunch envelope of the plasma OFF bunch. For all beam sizes $\sigma_{y,i}$, $r_y/r_{off} = 1$ correspond to the relative extent of a plasma OFF bunch. Bottom plot: bunch envelope normalised to the beam size $\sigma_{y,i}$ at the plasma entrance (iris).

Results Relative to Beam Size at Plasma Entrance Again, a normalisation of r_y is done, however this time with respect to a single number – the beam size at the plasma entrance (iris). The underlying idea is to obtain a measure comparing the relative bunch envelope growth with respect to the transverse beam size before the bunch entered the

plasma; see bottom plot of Fig.6.5. In the above introduced approach (top plot) the beam divergence can mislead us, since we compare the bunch profile of a bunch travelling in a drift space to one travelling in a plasma. This means one bunch is affected by a complex combination of multiple forces and the other one travels through drift space.

The approach in the previous paragraph is indeed mainly useful to determine the region dominated by adiabatic focusing, but not to make a statement in what way a change in initial beam size affects SM. Again, the reason for this is that the three beams not only differ in beam size $\sigma_{y,i}$ but also in angular divergence when they enter the plasma. This leads to the overlapping of the 330 μm and 560 μm curves seen in the top plot. Both plots have their raison d'être. However, while the first can only characterise adiabatic focusing, the second compares the divergence of bunch envelopes with respect to the beam size at iris.

It must be stressed that when normalising with the beam size at iris, the beam divergence is completely ignored. It has been shown in numerical simulations that a higher divergence at the same beam size inhibits SMI more.[2] This can be explained by the idea that it is more difficult to focus a beam which is stronger diverging.

The relative growth is on the bottom plot of Fig.6.5 now easily distinguishable. The larger the beam size at the iris, the lower the relative growth. In addition, the larger the beam size, the later the growth starts. This can again be interpreted as that the SMI arises not only weaker but possibly also later in the bunch.

Corrigendum   After submission of this thesis the presentation of the results on Fig.6.5 were reconsidered for the thesis defence. At the defence a third approach was presented which seems to be the best of the three in annulling the effect of the natural beam divergence. In this new approach the 80% bunch envelope of the plasma ON case is subtracted by the plasma OFF case. The results is shown in Fig.6.6
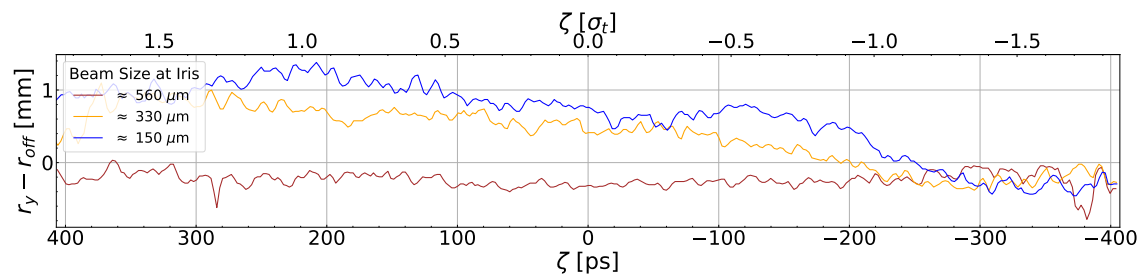

Figure 6.6: In this third approach instead of a normalisation, the plasma OFF case is dynamically subtracted at each time slice ζ from the plasma ON case.

At the plasma exit the 80% bunch envelope of the plasma ON case is a superposition of the beam divergence and the forces imposed by the transverse wakefields. The streak camera images show a cut of the $y\zeta$ – plane. The final position y_f of a proton in each slice ζ slice at plasma exit can be written as:

$$y_f = y_0 + v_{y,0}T + \iint\limits_{0}^{T} dt\, W_y(y,t) \tag{6.3}$$

---

[2]Based on *private communication, July, 2022* with *Dr John Farmer* about unpubl. studies showing this.

where y_0 is y coordinate at the plasma entrance, T the time to travel through the plasma source and $W_y(y,t)$ the transverse wakefield in y direction. The first and second term of Eq.(6.3) are independent of the situation in the plasma source. Indeed the distribution of the particle position and momentum at the plasma entrance is defined by the statistical beam properties. However, the third term is only non-zero when the plasma is ON. The 80% bunch envelope is a statistical measure per slice of the radial extent of the bunch. Calculating $r_y - r_{off}$ seem to be the best way to isolate the effect of the plasma wakefield with the data we have at hand. But, it has to be used with caution. Caution is necessary since we assume the individual Eq.(6.3) to be approximately true in a statistical regime without knowing the exact distributions of all three contributing terms. A comparison of the three proton beam envelopes reconstructed from the beam characterisation data is shown in Fig.A.3 in the appendix.

The conclusion about the self-modulation growth rate is not changed by this new approach.

6.2.3   Micro-Bunch Structure of a 560 µm Beam through SMI

In the framework of this thesis for the first time ever at AWAKE the micro-bunch structure of a beam having more than twice the transverse size of a baseline design beam is observed. In the previous section it was shown that compared to smaller beams the growth rate of a $\sigma_{y,i} \sim 560$ µm beam under SMI is very small. Now, we will take a look at smaller streak camera images with smaller time windows.

In front of the bunch centre of a beam with $\sigma_{y,i} \sim 560$ µm no micro-bunch structure is visible, and therefore, no SM happens as is proved in Fig.6.7 (two top plots). A total of thirty-two events are shown from which the eight of each row share the same time window. We explain the absence of SM ahead of the bunch centre by the reduced charge density of this larger beam. For SMI growing from noise, the transverse wakefields have different phases which compete against each other until eventually one phase wins. Our results indicate that with reduced charge density this process takes longer and therefore the micro-bunch structure appears later in the bunch.

Nevertheless, it would be wrong to think that no SM happens at all. Indeed after the bunch centre the first micro-bunches start appearing, see Fig.6.7 third plot. This means that later in the bunch on the 210 ps windowed streak images SM due to SMI occurs, while in the 1 ns window in the same time slice a clear adiabatic focusing can be detected. It is not surprising that these two phenomena overlap, but what should be emphasised is that depending on the time scale considered, one or the other stands out. Some events show a clear micro-bunch structure already at $\sim$25 ps while for others it can take about 200 ps longer. This is because in the SMI regime the SM arise from noise, so there is from shot-to-shot neither phase nor amplitude reproducibility.

6.2.4   Discussion

The SMI growth rate was measured via the radial extent of the bunch. This approach revealed satisfying results and is also consistent with the approach used in [5] to show the
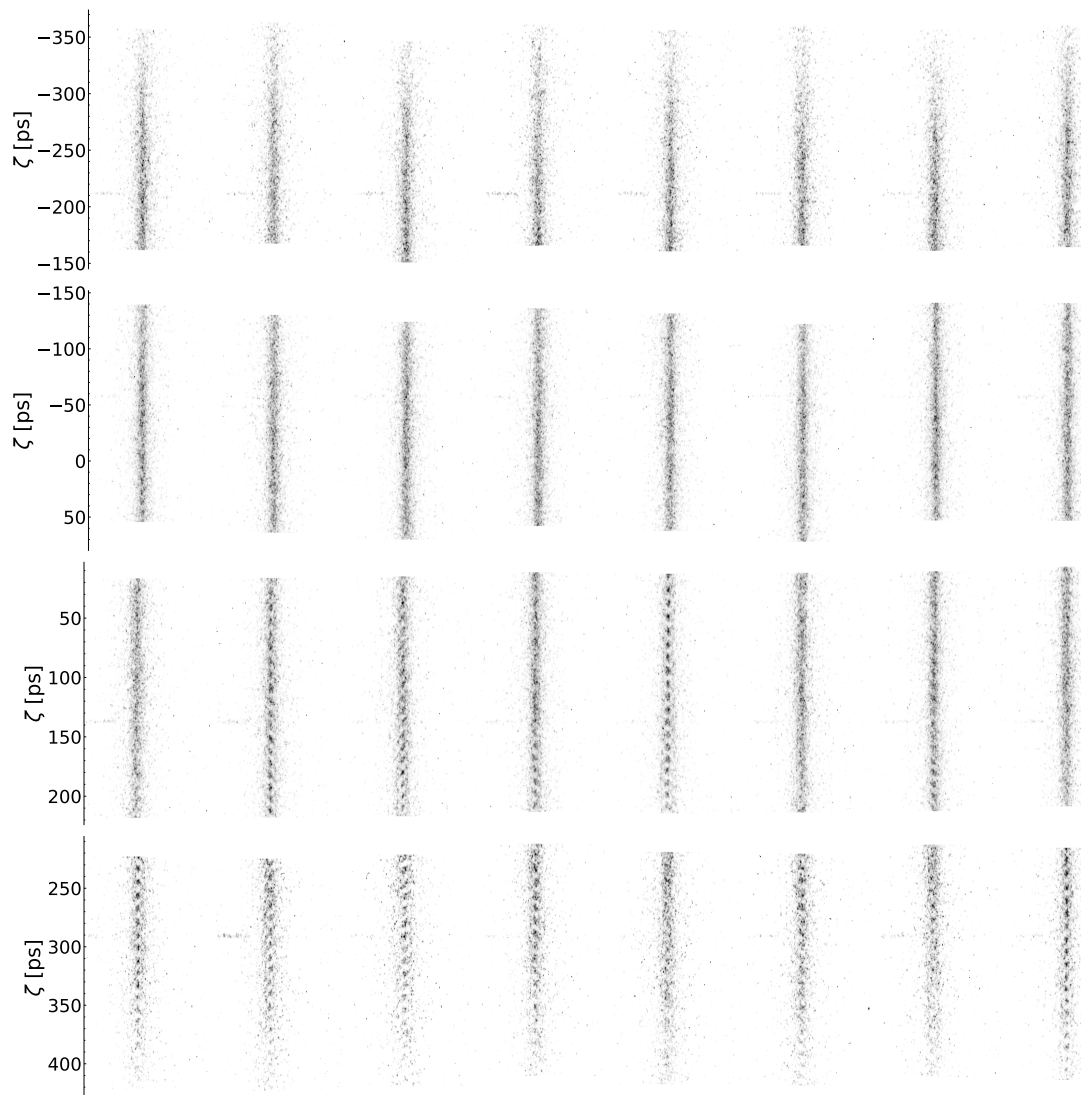
Figure 6.7: Time-resolved (y, ζ) images of p^+ bunches of $\sigma_{y,i} \sim 560\,\mu\text{m}$ transverse size at the iris. The RIF is positioned at $-2.6\sigma_t$. Horizontal rows present eight individual events. First row: range $\sim(-1.6$ to $-0.68)\,\sigma_t$. Second row range $\sim(-0.68$ to $0.23)\,\sigma_t$. Third row: range $\sim(0.11$ to $0.92)\,\sigma_t$. Fourth row: range $\sim(1.94$ to $2.03)\,\sigma_t$. The bunch duration is $\sigma_t \sim 219\,\text{ps}$. The colour-scale is logarithmic. *Note that images along one column are all from different events.*

dependence of growth rate on the p^+ bunch charge density. However, it is important to note that the bunch envelope curves do not correspond to the maximum radial halo extent as defined by r_m in the linear theory section 3.3. This is not only because several assumptions of the theory are invalid in the experiments, but also because the 80 % envelope does not represent the maximum extent.

Regarding Run 2c we have demonstrated that the SMI growth rate decreases with increasing beam size, which is due to the reduced charge density when the bunch population is kept constant. It is also qualitatively demonstrated that for a beam with a size of $\sigma_{y,t} \sim 560\,\mu\text{m}$ self-modulation in the front part of the bunch ($\zeta > 0$) is not observed. To make a qualitative statement about the SM probability, it is suggested to repeat these experiments over several hundred events.

Recall that for today's standard (baseline design) p^+ beam it is assumed that the

bunch part in front of the RIF will grow from (180 to 200) µm to about (490 to 540) µm when arriving at the second vapour source in Run 2c.

Two risks have been identified regarding Run 2c: Firstly, if a reduction of the beam emittance is considered in the future, the beam would expand less during the 11 m long propagation to the second vapour source. This means that the beam size at the entrance of the second vapour source could be smaller than expected in this work and as a consequence SM could still occur in front of the RIF. Whether RIF seeding is possible for Run 2c will therefore also depend on the future standard beam parameters. Secondly, our measurements were performed with a slightly larger beam ($\sigma_{y,t} \sim 560$ µm) than is expected to be present for Run 2c.

Recall as well that the waist positions of the beams used here are close to the plasma entrance and that the divergence of the beam is much smaller than will be the case in Run 2c. This is because in Run 2c the waist position should be at the entrance of the first and not the second vapour source. It has been shown in numerical simulations that this additional divergence further inhibits SMI.[3]

In summary, RIF seeding can be considered as a possible seeding variant for Run 2c until further notice.

6.3 Experimental Results of Seeded Self-Modulation Studies

From the studies of unseeded self-modulation, we now move to seeded self-modulation (SSM). The p^+ beams with sizes of 330 µm and 560 µm at the iris are studied. In the case where the self-modulation (SM) process is seeded it was shown that phase reproducibility for a standard beam of the baseline design can be achieved, see Tab.2.1 on page 9.[3] However, the physical process of seeding may well depend on the initial bunch parameters, especially on the charge density where the relativistic ionisation front (RIF) is positioned. For a standard beam a SSM to SMI transition region is found for RIF positions (-2 to $-1.8)\sigma_t$ (i.e., in front) of the beam.[35] For the two larger beams no systematic RIF scan has been executed in this work. Nevertheless, for the 560 µm beam, we considered two different RIF positions. Some of the results will be compared to numerical simulations.
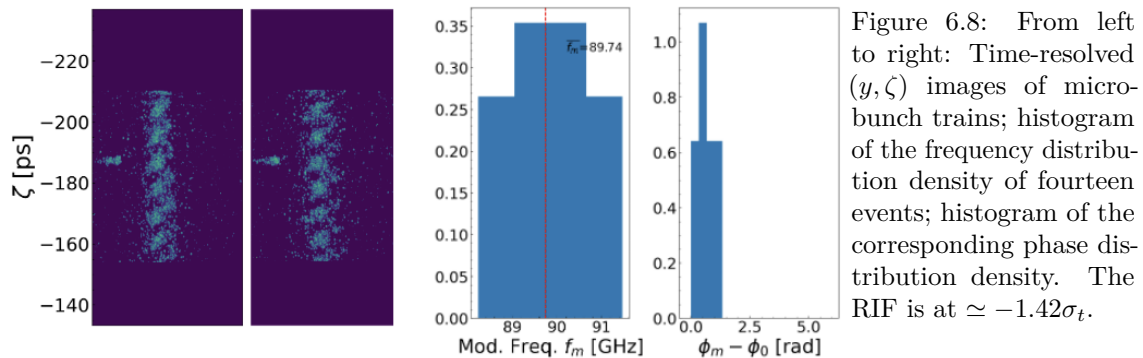
6.3.1 Phase Reproducibility

For both larger beams SM-phase reproducibility is confirmed by applying a *Discrete Fourier Transform* (DFT), as explained in section 5.3.2.

SSM of the 330 µm Beam   For the beam having a size of 330 µm at the iris measurements were taken with RIF$\simeq -1.42\sigma_t$ and a bunch length of 232 ps. To prove the phase reproducibility expected from SSM a streak camera window of 73 ps is chosen. The average SM-frequency is (89.74 ± 0.86) GHz, which implies by using Eq.(3.17) a plasma density of 9.99×10^{19} m^{-3} (the vapour source is set to hold a constant value of 1.0×10^{20} m^{-3}). The phase shows over fourteen events a standard deviation of 0.35 rad. The phase is

---

[3]Based on *private communication, July, 2022* with *Dr John Farmer* about unpubl. studies showing this.

taken modulo 2π and then subtracted by the smallest phase of the array, such that the phase difference we are interested in can be plotted. In Fig.6.8 on the left hand side two time-resolved images are shown as a waterfall plot. The marker is visible on both plots as a horizontal line on the left side of the micro-bunch trains (see chapter 5). The DFT is applied to fourteen time-resolved images in order to find the modulation frequency and phase of each micro-bunch train (Fig.6.8).

Figure 6.8: From left to right: Time-resolved (y, ζ) images of micro-bunch trains; histogram of the frequency distribution density of fourteen events; histogram of the corresponding phase distribution density. The RIF is at $\simeq -1.42\sigma_t$.

SSM of the 560 µm Beam

Experimental results show for RIF$\simeq -1.6\sigma_t$ over eight events SM appearing but almost no phase reproducibility (standard deviation of 1.44 rad). This might have unidentified technical reasons.[4] However, Fig.6.9 would also speak in favour of hosing (see section 3.5) which deforms the micro-bunch train in a way that the phase can no longer be identified. Take for example image three and eight on the waterfall plot (in Fig.6.9) as low-hosing examples while image seven shows strong hosing.
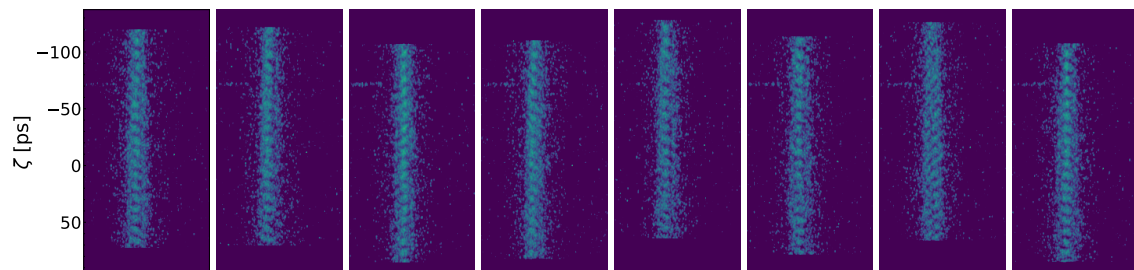
Figure 6.9: Time-resolved (y, ζ) images of a seeded p^+ bunch of $\sim$560 µm transverse size at the iris. The RIF is positioned at $-1.6\sigma_t$. Eight individual events with individual logarithmic colour-scale are presented.

A more symmetric micro-bunch train is found when moving the RIF to $\simeq -0.75\sigma_t$. In this framework phase reproducibility can be well proven over eleven events. Looking at a 73 ps window the average SM-frequency is (89.88 ± 0.96) Ghz. This implies by using Eq.(3.17) a plasma density of $1.002 \times 10^{20}\,\mathrm{m}^{-3}$. The phase shows a standard deviation of 0.84 rad.

In case of a 210 ps window (Fig.6.10) the average SM-frequency over eleven events is (88.5 ± 4.1) Ghz. This implies by using Eq.(3.17) a plasma density of $9.7 \times 10^{19}\,\mathrm{m}^{-3}$

---

[4]For this RIF position no 73 ps windowed time-resolved images are available. Phase identification can, however, also be done with 210 ps windowed images.

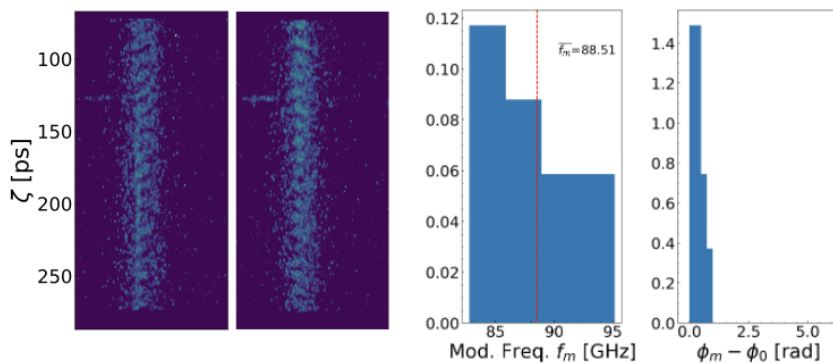(about $3\,\%$ less). The phase shows a standard deviation of $0.26\,\mathrm{rad}$.

Figure 6.10: From left to right: Time-resolved (y,ζ) images of micro-bunch trains; histogram of the frequency distribution over eleven events; histogram of the corresponding phase distribution. The RIF is at $\simeq -0.75\sigma_t$.

6.3.2   Comparing Experiment and Simulation

For the comparison of results from the experiment and simulation the focus lies on the two new larger beams. The standard beam shall not be shown here repeatedly with RIF$= 1.4\sigma_t$, as studies of time-resolved images for the seeded have been performed previously.[74–78] We compare the results from the streak camera for three window sizes of time-resolved images and from simulations $\sim$1 ns, 210 ps and 73 ps. The post-processing approaches applied on the simulation output vary depending on whether $\sim$1 ns, 210 ps or 73 ps images are compared.

The output of the simulations consists of the set of simulated macro-particles with their associated coordinates (in 2D), their momenta (in 3D), their weights and some other parameters not relevant here. The standard processing, i.e., conversion into Cartesian coordinates, possible down or up sampling as well as propagation in drift space to the virtual streak camera position is described in section 4.4. For comparison with the streak camera images, they are in addition binned in such a way that the 2D bin size corresponds along the temporal and spatial axes to the pixel size of the streak camera image.

As described in section 5.1, during the data acquisition process of the streak camera an integration of the three dimensional signal $(\zeta,\,y,\,x)$ along the spatial axis x takes place to finally get a 2D image $(\zeta,\,y)$. The integration range is physically given by the slit-width of the camera. Integration over the same range of $20\,\mu\mathrm{m}$ is also applied to the simulations.

The post-processing described in what follows is used to compare 210 ps and 73 ps windowed images. The binning can be considered as convolution to adjust the resolution. In the case of the $\sim$1 ns window, however, it turns out that this is not sufficient to make a comparison, because while in the simulations after binning the micro-bunch train is visible, this is not the case on the streak images. From this it can be concluded that the limiting resolution of the streak camera system is not the camera pixel resolution. Since this mismatching shows up along the temporal axis, one might think that the delta-like photon emission of the OTR screen is not sharp enough and thus smearing occurs. However, this is contradicted by the fact that for shorter time windows the micro-bunches can be resolved. So the streak camera itself remains as the limiting factor, probably due to a limitation of the sweep time (see section 5.1).

To account for this additional smearing, the temporal binning (ζ) is reduced by a

factor of six for comparison with a ~1 ns streak window image. This is approximately the factor for which the micro-bunch structure is no longer visible.

Results   First we compare the ~1 ns time window of a beam with transverse size of $\sigma_{y,i} = 330\,\mu\text{m}$ at the plasma entrance. In Fig.6.11a the simulation results with and without additional resolution reduction are shown. Here the 90 % bunch envelope introduced in section 6.2.1 is shown as a red line. For the simulations, the particles lost during the simulation could be taken into account in the normalisation. With the argumentation that lost particles cannot be taken into account in the experiment, we refrain from doing so.

The time-resolved streak camera image is shown in Fig.6.11b; the 80 % bunch envelope is plotted as well. In simulations and in the experiment the RIF is at $\simeq -1.4\sigma_t$. The simulation parameters correspond to S-Set2 in Tab.4.1, so they were adapted to the parameter space of the experiment. The bunch envelope has been chosen to have a similar extent at the envelope's tightest ζ coordinate.

In both experiment and low-resolution simulation images the maximum transverse extent given by the bunch envelope is reached in the range $(-100 \text{ to } -80)\,\text{ps}$ in front of the centre. However, while in simulations (Fig.6.11a) the envelope around the bunch centre becomes smaller again, in the experiment it remains straight or even continues growing around the bunch centre.

(a) Simulation
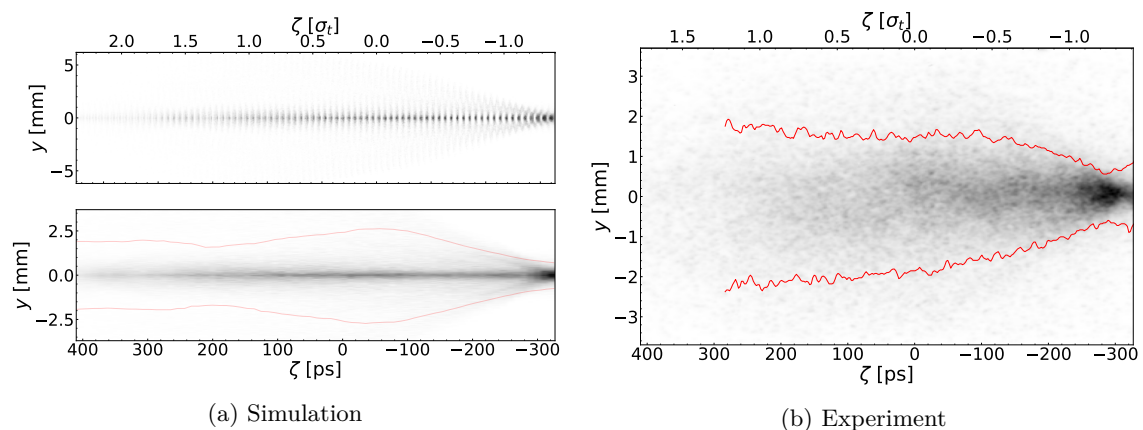
(b) Experiment

Figure 6.11: Comparing 1 ns windowed images (ζ, y) of a bunch seeded at RIF$\simeq -1.4\,\sigma_t$, of beam size ~330 μm at the iris. For simulations the **S-Set2** parameters are used. The 80 % (experiment) and 90 % (simulation) bunch envelopes are plotted as a red line. Figure 6.11a shows the top plot binning according to the streak camera resolution, and the bottom plot additional ζ resolution reduction, to better imitate the streak camera image in Fig.6.11b.

More scientifically satisfying results are found for images of shorter time windows. In Fig.6.12, a 210 ps window was chosen with the largest beam at hand ($\sigma_{y,i} = 560\,\mu\text{m}$). We show in Fig.6.12a the simulation result and in Fig.6.12b the streak camera image. The bunch envelopes are no longer plotted, but straight lines at $y = 0.5$ are shown to give a reference to the core part of the micro-bunch train. We see that the extent of the core parts between simulations and experiment are comparable, although the rear part of the bunch is considered. The divergent sections of the micro-bunch train are more clearly visible in the simulation. This is in accordance with the findings later on in section 6.4.2, where it is shown that the core part is less emphasised in the experiment than it is in the simulations.

The parameter space specified by the experiment was also adopted for these simulations (S-Set2). A summary of the parameters used to run the simulations is provided in Tab.4.1.
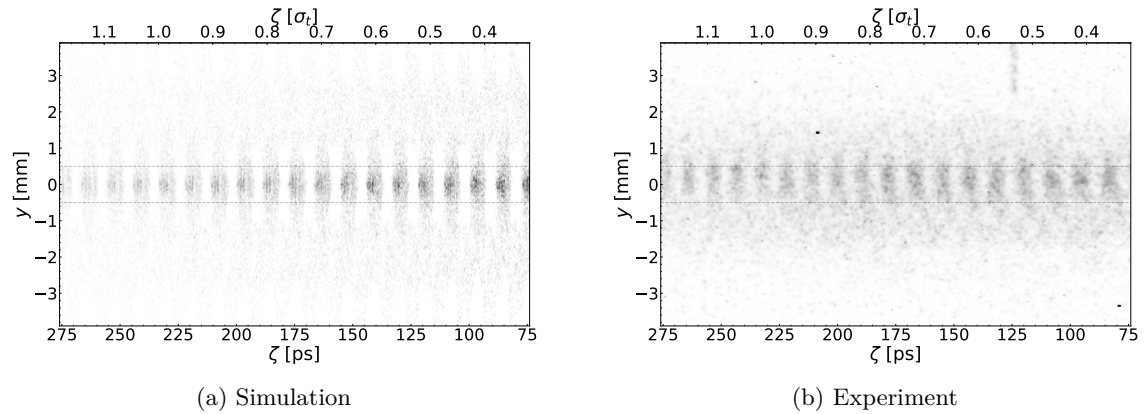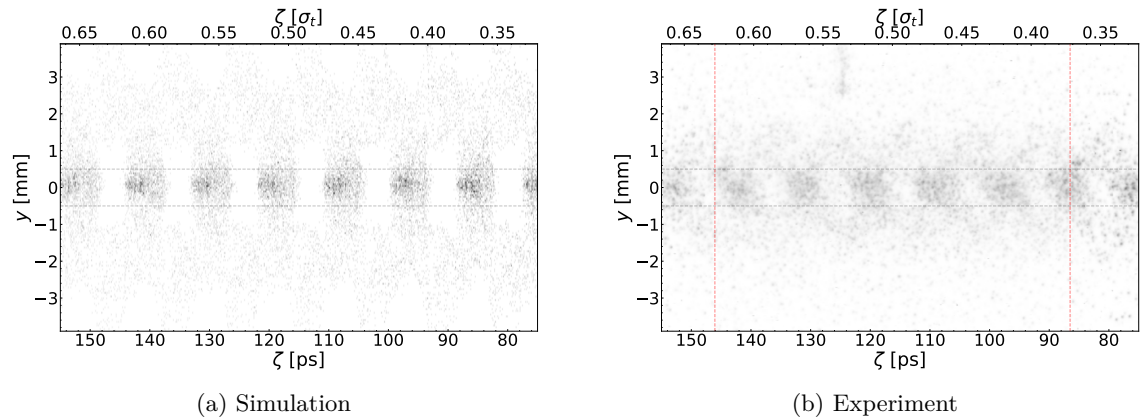

(a) Simulation

(b) Experiment

Figure 6.12: Time-resolved (ζ, y) images of p^+ bunchs of $\sim560\,\mu$m transverse size at the iris. The RIF is positioned at $-0.75\,\sigma_t$. For simulations the **S-Set2** parameters are used.

The last comparison shows a 73 ps time window (Fig.6.13). In Fig.6.13a the simulation and in Fig.6.13b the result from the experiment is shown. Again, the agreement of the core extent is satisfactory. Because the streak camera image is a superposition of several slightly shifted but aligned individual images, the red vertical lines indicate in which range at least 80% of all images are averaged. The average is weighted as described in chapter 5.

(a) Simulation

(b) Experiment

Figure 6.13: Time-resolved images of p^+ bunch of $\sim560\,\mu$m transverse size at the iris. The RIF is positioned at $-0.75\sigma_t$. 80 % image density is indicated by red lines. For simulations the **S-Set2** parameters are used.

6.3.3 Discussion

For the $\sigma_{y,i} \sim 330\,\mu$m beam, as expected phase reproducibility has been verified for a seeding at RIF$\simeq -1.4\sigma_t$ – the determined frequency corresponds to the theoretical expectations.

For the $\sigma_{y,i} \sim 560\,\mu$m beam, no reproducibility was detected with seeding at RIF$\simeq -1.6\sigma_t$. Recall in this context that for the standard beam (with size $\sigma_{y,i} \sim 150\,\mu$m), successful reproducibility up to seeding of at least RIF$\simeq -1.8\sigma_t$ was found for a bunch population of $3 \times 10^{11}\,p^+$ and a similar bunch length (duration). This is an indication that the SSM – SMI transition region depends on the transverse beam size via the local charge density in the region of seeding. This would mean that if the charge density is below a

certain configuration-specific threshold, no reproducibility is achieved by seeding. This can be explained by the fact that the wakefields arising abruptly by seeding are weaker due to the reduced charge density.

On the other hand, visual inspection of the analysed micro-bunch trains also reveals problematic hosing in some cases, which can affect the Discrete Fourier Transform used to verify reproducibility. It is an open question as to whether hosing is increased by increasing the beam size. By shifting the RIF to $-0.75\sigma_t$ in front of the bunch centre, we obtain reproducibility of the micro-bunch train. This demonstrates that seeding of a beam with a size of $\sigma_{y,i} \sim 560\,\mu\mathrm{m}$ is in principle possible.

In comparison with the numerical simulations we find the following: the bunch envelopes do not match satisfactorily for a 1 ns time-window. This is probably due to the resolution of the experimental 1 ns window images. Additionally, in the experimental results a distinction between the core and the halo part of the bunch is much less significant, whereas in the simulated images the core clearly stands out.

If smaller streak camera time windows are used (210 ps and 73 ps) the agreement is more satisfactory. This can be attributed to the higher temporal resolution. The radial extent of the micro-bunch train agrees in simulation and experiment. However, an analysis of the projection onto the y- and ζ-axis is intentionally omitted because it is unclear how a satisfactory normalisation should be done at a ζ far away from RIF.

In summary, our results imply, but do not prove a dependence of the SSM – SMI transition region on the beam size via the bunch's charge density. They also show that the micro-structure of a $\sigma_{y,i} \sim 560\,\mu\mathrm{m}$ beam is qualitatively comparable in experiment and simulation.

6.4 Focus on Simulation Results

6.4.1 Phase Space and Bunch Propagation

Numerical quasi-static particles in cell simulations bring the advantage that in the output the positions and momenta of each particle are well known. We can therefore have a look at the phase space of a $\sigma_{\perp,i} = \sigma_{x,i} = \sigma_{y,i} = 560\,\mu\mathrm{m}$ beam before entering the plasma, when leaving the plasma and after travelling in drift space to reach the "virtual" streak camera.

In Fig.6.14a and 6.14b exactly these three phase spaces are shown. On both plots the phase space distribution of the bunch before entering the plasma is plotted in red. After propagation in the 10 m long plasma, the bunch takes up a much larger part of the phase space. Above all, the order of magnitude of transverse momentum gained by individual particles of the bunch due to SSM (the momentum spread goes from 15.95 GeV/c before the plasma to 75.7 GeV/c after plasma) becomes clear.

The transverse position range also increases, but in a smaller order of magnitude than for the momenta: the standard deviation of the projected transverse position distribution goes from 560 µm before the plasma to 910 µm after plasma, in the case where no plasma is

present it would go to $687\,\mu m$.[5] Furthermore, Fig.6.14b shows how the phase space changes before the bunch reaches the streak camera in the experiment. Note that the propagation distance to the image station to IS1 is shorter $(2\,m)$ and to IS2 longer $(10.14\,m)$.
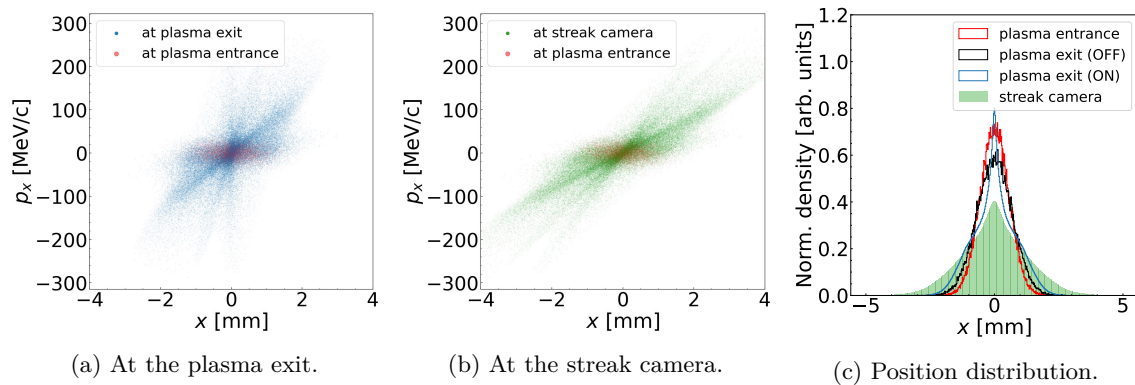

(a) At the plasma exit.   (b) At the streak camera.   (c) Position distribution.

Figure 6.14: Phase space and position distribution of a simulated p^+ bunch with $\epsilon_n = 9.5$ mm mrad and $\sigma_{y,i} = 560\,\mu m$ undergoing SSM in a 10 m long plasma or travelling the same distance in a drift space. Parameter set defined in **S-Set2** is used.

In Fig.6.14c the beam size at plasma entrance, at the plasma exit (plasma ON and OFF), and at the "virtual" streak camera when the plasma is ON are plotted. Comparing the shape before and after plasma it can be seen that the beam is no longer Gaussian after SSM (blue histogram). Indeed the core (small peak at $x = 0$ mm) shows a higher particle density than a Gaussian beam would. On the other hand, the winglets of the Gaussian also show a higher density, this is the halo of the SSM micro-bunch train. At the streak camera this is effect is already much less present (green histogram), because of the divergence of the beam after SSM. The black line acts as reference how the bunch would look like if there were no plasma (plasma OFF) in the vapour source.

To conclude, the bunch shows a higher standard deviation in position after undergoing SSM, but when looking at the position distribution along the x-axis it becomes clear that the bunch no longer takes a Gaussian shape, but a particular core-halo distribution. All parameters were set according to S-Set2 in Tab.4.1, i.e., in particular that $\epsilon_{n,y} = 9.5$ mm mrad and $\sigma_{y,i} = 560\,\mu m$.

6.4.2 Transverse Profile after Seeded Self-Modulation

Another possibility to compare the experiment and the simulations are the two image stations. In the experiment the two image stations, IS1 and IS2 take accumulated transverse bunch profile. As previously done, about 10 individual events are superimposed. Again, we will focus on the largest beam of $\sigma_{y,i} = 560\,\mu m$ for the analysis. For the simulations, the parameter space defined in S-Set2 in Tab.4.1 applies. The simulation output is propagated in a drift space to the position of the "virtual" image stations as has already been discussed. It is important to note that in the numeric simulation results the part of the bunch in front of the RIF is not mimicked.

---

[5]Note that these simulations and calculations are based on a simulated bunch of larger normalised emittance than used for MADX simulations. Simulation parameters are based on the parameters found by the beam characterisation, see Tab.2.3 on page 20.

It turns out that it is sensible to reduce the colour-range of the simulated images by about 40 % for a good comparison. By this the core appears saturated, but the structure around the core becomes more clearly visible. A similar result could have been achieved by masking the core. Fig.6.15a shows the result including the projections along the two Cartesian axes (x, y). The experimental image of IS1 is shown in Fig.6.15b including projections.
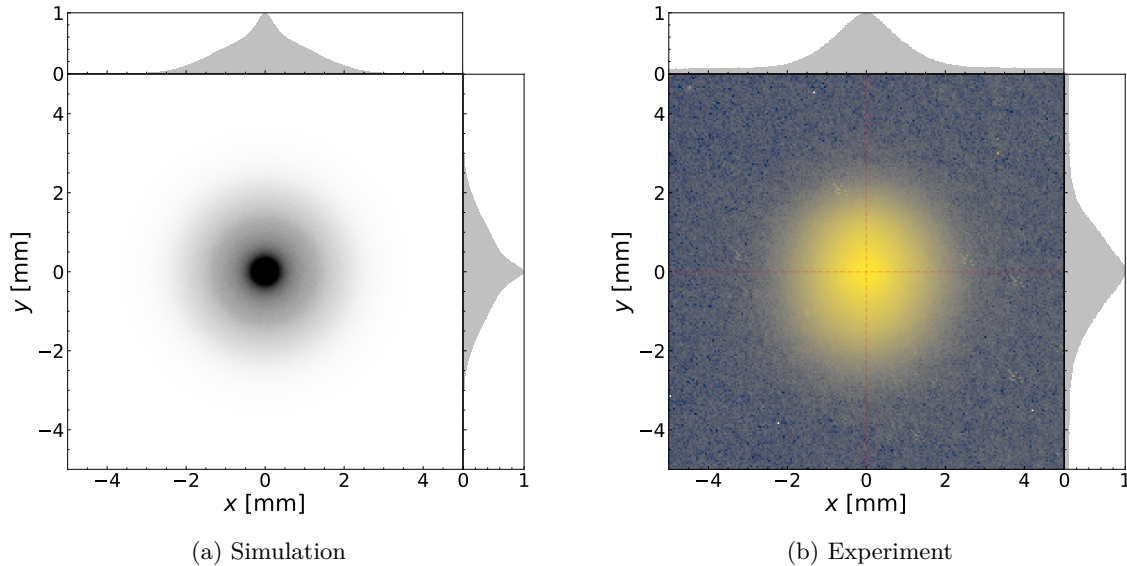

(a) Simulation   (b) Experiment

Figure 6.15: Transverse bunch projection at IS1. For simulations **S-Set2** is used.

A closer look at the projection shows that the core part (in the nearest neighbourhood of $x = y = 0$) is sharpened in the simulation, which is not the case in the experiment. It is assumed that this "core smearing" in the experiment is caused by hosing. Note that this sharpening also does not occur on single event images (see Fig.A.7). It is therefore unlikely that the difference in profile are due to position jittering. A third reason could lie in the fact that for simulations the part of the bunch in front of the RIF is not taken into account. This part will propagate like in the plasma OFF case through that vapour cell as it would be a drift space and keeps therefore its approximately Gaussian profile. Superimposing this Gaussian profile would lead to a smoothing of the sharp profile, but not extinguish the peak.

The radial spread of the visible bunches in the experiment and the simulation is around 2 mm.

The boundary between core and halo is in general difficult to define, especially in the experiment. In the experiment the HALO cameras masks the centre, to make the weaker signal outside a radius of about 1.5 mm visible. It would, however, be wrong to assume that the halo only starts from a radius of 1.5 mm upwards. The simulation results in Fig.6.15a implies namely that the core has a radius of less than 0.5 mm and the range from approximately (0.5 to 2) mm already shows the halo structure.

The situation on IS2 is shown in Fig.6.16. Here the colour-scale of the simulation was intentionally not adjusted because the core sharpening is weaker with the additional propagation distance. It can be guessed that the bunch profiles again have a similar radial

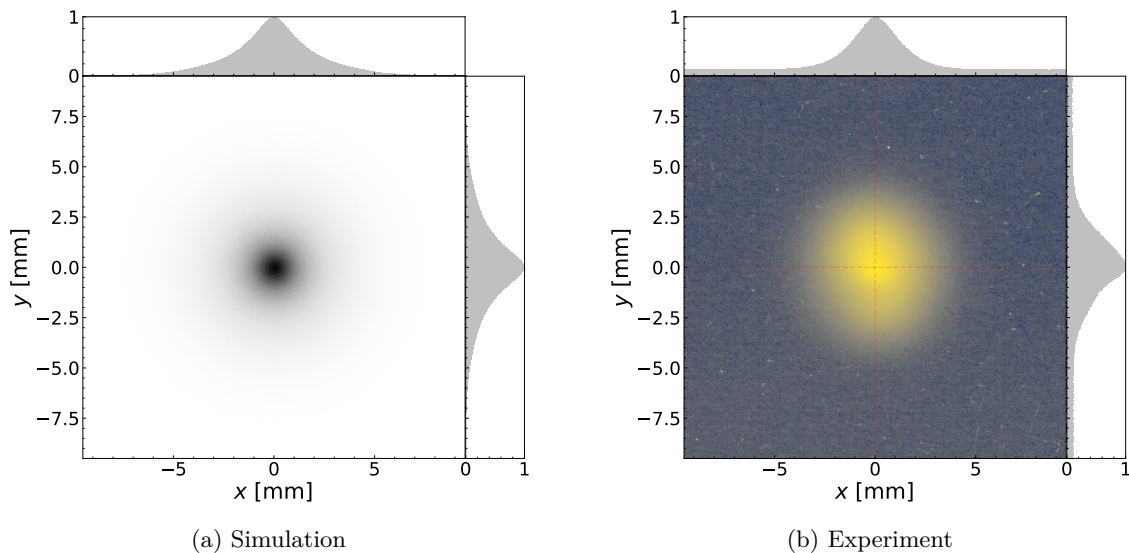(a) Simulation

(b) Experiment

Figure 6.16: Transverse bunch projection at IS2. For simulations **S-Set2** is used.

spread. However, the core part overshadows a more detailed analysis. In summary, it can be said that a comparison is only of limited use. Another phenomenon, however, deserves closer examination. In Fig.6.15a a kind of band structure can be seen in the halo. This will be examined in more detail in the following section.

6.4.3   Band Structured Transverse Profile after Self-Modulation

To compare the weakly visible band structure in Fig.6.15a it turned out to be useful to introduce the radial density ρ_{rad} function known from statistical physics.[79, 80] However, some adjustments are made, since we have no particular interest in comparing the local density to the overall averaged particle density. At this stage we are actually interested in the qualitative distribution of the density, and not in absolute values.

The radial density is in the general case implicitly defined as:

$$N = 2\pi \int_0^R dr\, r\rho_{rad} \tag{6.4}$$

where N is the number of total particles in the circle with radius R

In the specific case when taking the weights of each macro-particle into account $\rho_{rad,i}$ is given in each radial shell i by:

$$\rho_{rad}(r_i) = \frac{1}{2\pi r_i} \sum_{n=1}^{N_i} w_n \tag{6.5}$$

where N_i is the total number of macro-particles in radial shell i of radius r_i. For each particle in the shell, w_n is the corresponding weight. In addition, ρ_{rad} is normalised before plotting in such a way that the integral of the samples over the histogram range is equal to one.

As can be seen later on, small radial density changes are hard to identify when plotting

the radial density function. It is actually easier to see these changes when considering the probability of finding one macro-particle in a small radial shell $[r + dr]$. In detail we define the radial probability as:

$$P_R = 2\pi \int_{R-\delta r}^{R+\delta r} dr \; r\rho(r) \tag{6.6}$$

Adapting to a discrete calculation means for a radial shell r_i:

$$P_R(r_i) = 2\pi r_i \rho(r_i) \tag{6.7}$$

The radial probability P_R is normalised in the same way as the radial density.

Applying Eq.(6.5) and (6.7) to the numeric simulation results of the beam with $\sigma_{\perp,i} = 560\,\mu m$ (S-Set2), Fig.6.17 is produced. In this figure the normalised radial probability is plotted as a histogram and the normalised radial density as lines. This is done at three positions; at the plasma exit and at "virtual" IS1 (2 m after exit) and IS2 (10.14 m after exit). The grey curve serves as reference by showing the radial probability corresponding to a normal distributed beam of $\sigma_\perp = 0.9\,mm = 900\,\mu m$ which is approximately equal to the standard deviation of the particle distribution.
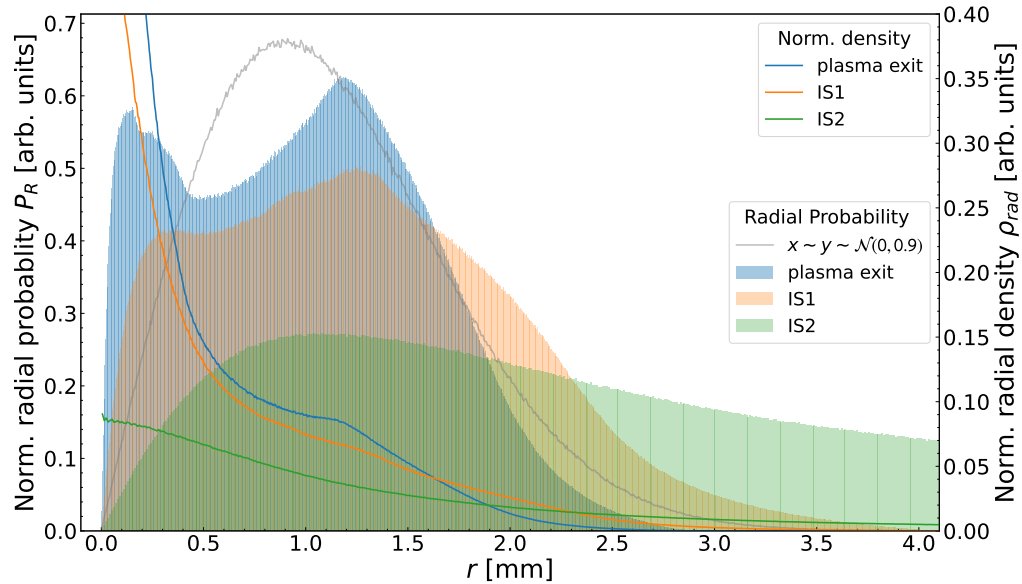
Figure 6.17: Normalised radial probability and density plotted at the plasma exit and after propagation to IS1 and IS2. The grey curve shows as a reference the radial probability a of bi-Gaussian distributed beam with $\sigma_\perp = 900\,\mu m$. Parameter space of the simulation according to **S-Set2** with beam size of $\sigma_{\perp,i} = 560\,\mu m$.

Let us focus on the plots showing the distribution at the plasma exit, since the structure is not yet smoothed out by further propagation. When considering the probability density P_R of the simulated beam two local maxima should interest us. The first at about $0.15\,mm$ is due to the core of the beam. Recall that this peak does not denote the radius of highest proton density, but the radius at which the probability to find a particle is the highest. The particle density peaks as expected closer to $r = 0$. The second peak of interest in P_R is found at a radius of $\simeq 1.2\,mm$. This is where we visually see some sort of simple band-like structure in Fig.6.15a.

The further the beam propagates after quitting the plasma source, the more it spreads

out, since the forces induced by adiabatic focusing which held the beam together are no longer present. Also, the focusing force on the core particles in the bunch core due to SMI stops acting once the beam leaves the plasma. This spread means that in the case of hosing-free SSM on the IS2 camera, no distinction can be made between core and halo (see green histogram and line on Fig.6.17).

Transverse Beam Size Scans   To investigate the band structure faintly visible in Fig.6.15 in more detail, the baseline design parameters of AWAKE are used for further investigation; this means that the plasma density is increased to $7 \times 10^{20}\, 1/\mathrm{m}^3$. In addition, we simulate a 12 cm long bunch. The seeding was set to $-1\sigma_t$ ahead of the bunch centre and the simulation window was extended to a total length of $2\sigma_t$. The beam is observed directly after propagation through 10 m of plasma and is not propagated further to the image station position of the experiment. See Tab.4.1 S-Set3 for the parameter space in use.
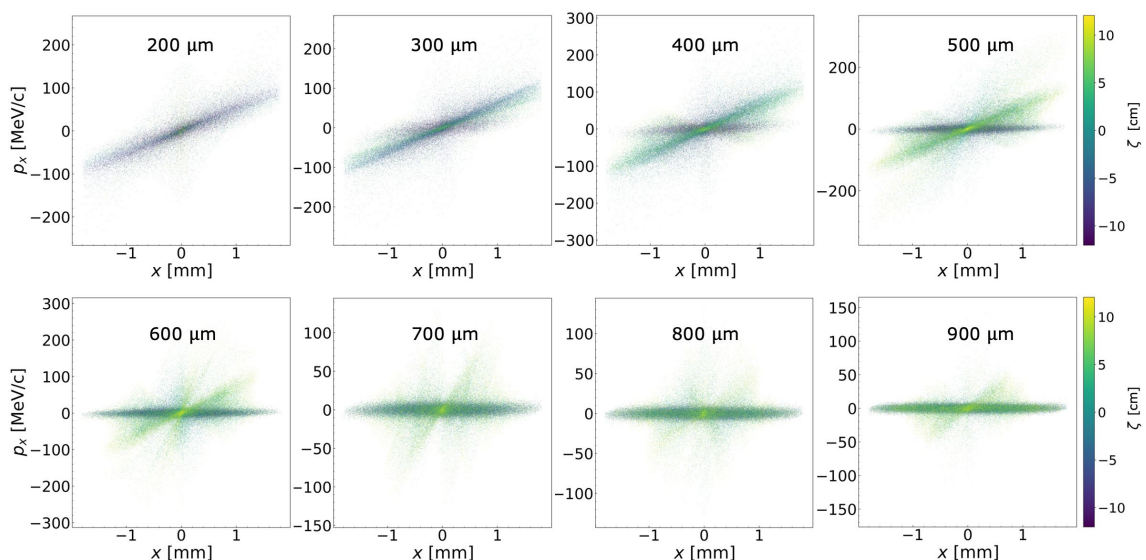
Figure 6.18: Phase space of proton beam after travelling through 10 m of plasma for initial transverse beam sizes $\sigma_{\perp,i} = (200 \text{ to } 900)\,\mu\mathrm{m}$. The weighted macro-particles are colour-coded by their position inside the bunch: from violet (front of bunch) to yellow (back of bunch). The parameter set **S-Set3** was used.

In Fig.6.18 we present the phase space of eight such simulations with beam sizes $\sigma_{\perp,i} = (200 \text{ to } 900)\,\mu\mathrm{m}$. For the 200 μm beam size we can see that the defocusing momentum increases linearly with the position; the further the particles are away from the axes the larger the momentum. The particles further back in the bunch experience on average stronger wakefields and are therefore carried further out. This linearity between defocusing momentum and radius also implies that the transverse wakefields are only strong locally around the core. For larger beams, with $\sigma_{\perp} = (400 \text{ to } 900)\,\mu\mathrm{m}$, off-axis particles appear that have a focusing momentum ($x > 0, p_x < 0$ or $x < 0, p_x > 0$). This means that particles originally in a defocusing regime have fallen back into a focusing regime. This may be due to a phase shift of the wakefields along the plasma.

In Fig.6.19 the full transverse projections for all eight beam sizes are plotted. The colour-scale is linear but individual for all plots. In all figures the maximum of the colour-scale is set to the value at a radius of 0.05 mm. This helps again to make the halo structure
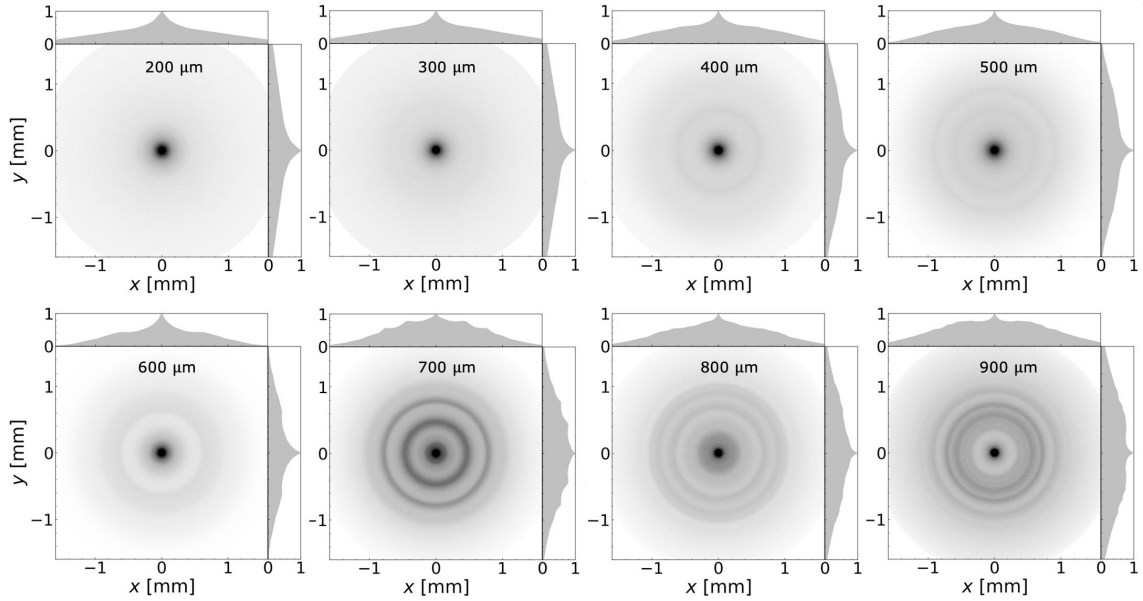
Figure 6.19: Full transverse projections for initial transverse beam sizes $\sigma_{\perp,i} = (200 \text{ to } 900)\,\mu\text{m}$. The parameter set **S-Set3** was used.
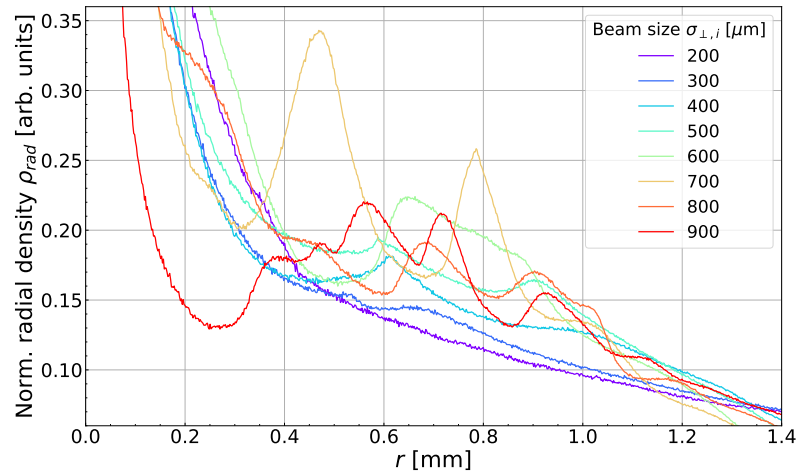

Figure 6.20: Normalised radial densities for initial transverse beam sizes from $(200 \text{ to } 900)\,\mu\text{m}$. The parameter set **S-Set3** was used.

better visible. The x- and y-projections show for all beam sizes a clear peak in the centre where the core is found. The further the beam size grows the more complicated the radial structure becomes – more rings start appearing. In Fig.6.20 the normalised radial density is plotted to make this more clear. Up to an initial transverse beam size of $400\,\mu\text{m}$ only one clear peak occurs. For larger beams multiple peaks show up and each corresponds to one ring or band in Fig.6.19. The peak values tend to decrease with the radius.

By considering a cut in the $y\zeta$ – plane a sort of filaments become visible. In Fig.6.21 this is shown for the beam of $600\,\mu\text{m}$ initial beam size.[6]

Discussion These band-like structures which become more significant the larger the beam size grows are observed for the first time here. They have not been previously

---

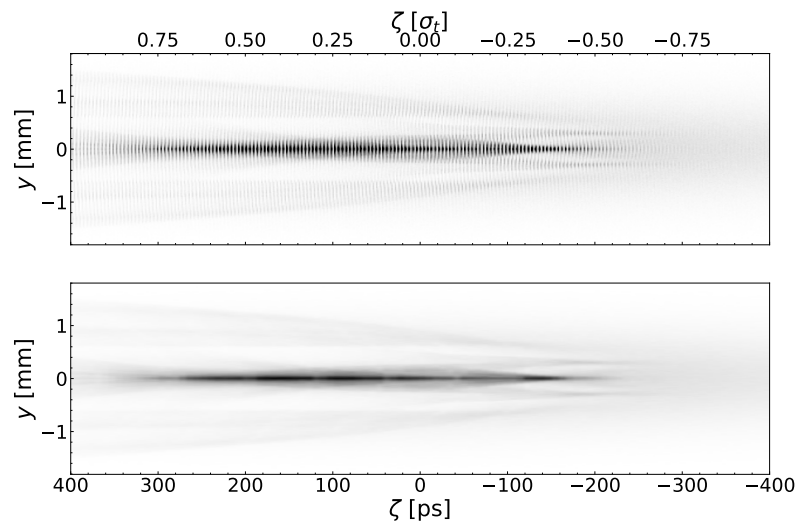[6]Presented at the Master's thesis defence and here added as a corrigendum.

Figure 6.21: Cut through the bunch centre: $y\zeta$ – plane of two different resolutions. The initial transverse beam size is $\sigma_{\perp,i} = 600\,\mu m$. The parameter set **S-Set3** was used.

described and it is proposed to study them further to understand why they occur. One reason for their appearance could lay in a phase shift of the transverse wakefield along the plasma for certain regions inside the bunch. This could lead to accumulations of first defocused but later focused particles at a given radius. However, such a phase shift would also affect, or even destroy the micro-bunch train. The "filamentation" visible in Fig.6.21 could come from an higher order mode of the two stream instability, which is not seen for a beam size similar to the plasma skin depth. In the here presented simulations the plasma skin depth is $\sim 200\,\mu m$ while the proton beam has a transverse size of $600\,\mu m$. Therefore, the beam is three times larger than the skin depth, and higher order modes could develop on a length scale that is not shielded by the plasma skin depth.[78]

We have also seen that these ring structures weaken when the bunch travels after the plasma through drift space. This is one reason why we do not necessarily expect this structure to be visible in the experiment. Furthermore, it was shown that the transverse projections of the bunch appears much smoother in the experiment. And it is already difficult to identify the core on the CORE cameras. This may be due to the propagation from the plasma exit to the diagnostics or other reasons which cannot be specified at the moment.

---

[7]Presented at the Master's thesis defence and here added as a corrigendum.

[8]When performing 3D simulations a spoke-like structure appears in the halo in addition to the rings. These simulations were performed with *qv3d* by *Dr John Farmer* after this thesis was submitted. The results were presented during the defence and are attached in the appendix (see Fig.A.6).

7 Conclusion

In this Master's thesis I first presented and explained in detail the beam characterisation code that I had previously begun developing, but which I constantly improved during the thesis. The code is used at AWAKE for a fast characterisation of the proton beam on daily basis before the plasma experiments start. I performed and presented the analysis of the three beams studied in the framework of this thesis. This characterisation helps to better describe the proton beam used in the experiment and to find the parameter space for numeric simulations. The three transverse proton beam sizes at the plasma entrance of interest in this thesis are $150\,\mu\mathrm{m}$, $330\,\mu\mathrm{m}$ and $560\,\mu\mathrm{m}$. The experiments we performed can be split into two categories; experiments where the transverse wakefields are unseeded and experiments where relativistic ionisation front (RIF) seeding was applied. The proton bunch had in both cases a length of about $6.7\,\mathrm{cm}$. The plasma density was set to $1 \times 10^{20}\,\mathrm{m}^{-3}$.

For the unseeded case, I studied the $80\,\%$ bunch envelope of the three transverse beam sizes ($150\,\mu\mathrm{m}$, $330\,\mu\mathrm{m}$ and $560\,\mu\mathrm{m}$) on $1\,\mathrm{ns}$ windowed time-resolved streak camera images. For all three beam sizes the regions where adiabatic focusing is dominant along the bunch were identified. I showed the relative bunch envelope growth along the proton bunch of all three beams with respect to their transverse size at the plasma entrance. This gives a measure of the self-modulation growth rate along the proton bunch and I demonstrated that the self-modulation growth rate decreases with increasing initial transverse beam size. Since the bunch population was kept constant for these measurements this indicates a dependence of the self-modulation growth rate on the bunch charge density. For the beam with a transverse size of $560\,\mu\mathrm{m}$ no micro-bunch structure ahead of the bunch centre was observed. This demonstrates that RIF seeding could be suitable for the future AWAKE Run 2c.

In the seeded case phase reproducibility was demonstrated in this thesis for a proton bunch of a transverse size of $330\,\mu\mathrm{m}$ and a RIF seeding at $\simeq -1.42\sigma_t$ ahead of the bunch centre, and for a $560\,\mu\mathrm{m}$ size bunch and seeding at $\simeq -0.75\sigma_t$ ahead of the centre. In the seeded case for a beam of $560\,\mu\mathrm{m}$ transverse size a good qualitative agreement between micro-bunch structure obtained by streak camera measurements and numerical simulations was obtained. In simulations I showed that the saturation point of the longitudinal wakefield is shifted further away from the plasma entrance when the initial transverse bunch size is widened. Here beam sizes from $(100 \text{ to } 1000)\,\mu\mathrm{m}$ are presented. Furthermore, I found in the transverse projections of a $12\,\mathrm{cm}$ long bunch at a plasma density of $7 \times 10^{20}\,\mathrm{m}^{-3}$ a previously unseen radial ring structure that depends on the initial transverse beam size. Once the origin of these rings is understood they could serve as a future self-modulation diagnostic.
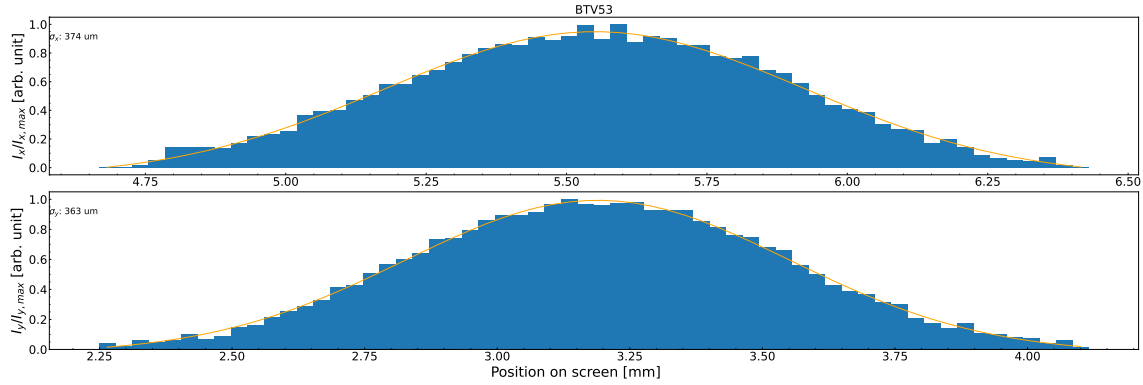
A Appendix

A.1 Proton Beam Characterisation

Effect of Secondary Particles
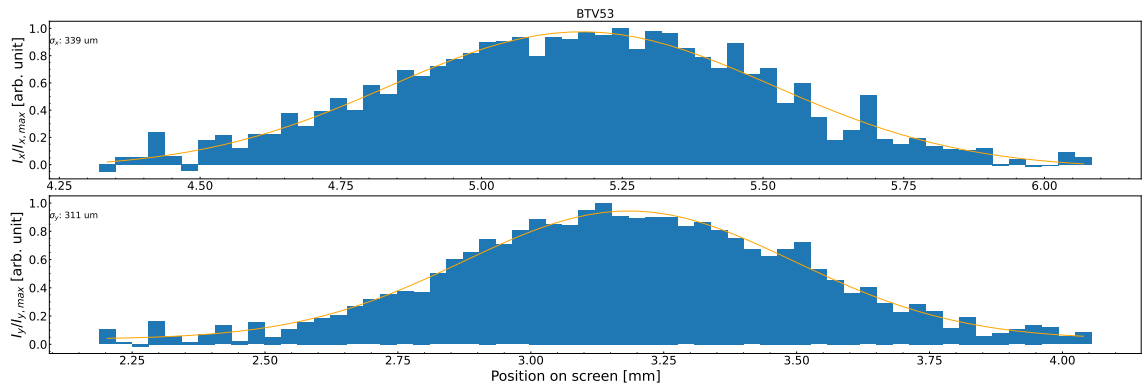
(a) Previous screen IN.

(b) Previous screen OUT.

Figure A.1: Example of data quality. Data for a beam size measurement at BTV53. Projections along both transverse axes when the next upstream screen is present (a) or not (b). Sources of noise are secondary particles produced when the beam crosses the previous screen.
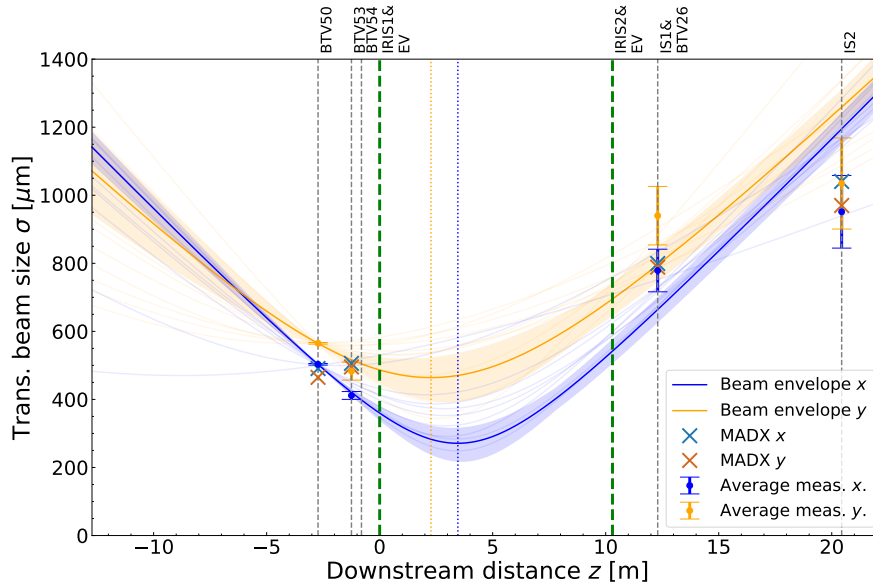
Additional Proton Beam Envelope Plots

Figure A.2: Proton beam envelope of a beam with transverse target beam size $\sigma_{x,y} = 500\,\mu\text{m}$ at the iris. Probably nonphysical measurement on BTV53. Blue and yellow main lines show the beam envelope based on average trans. size measurements in x and y; points denotes average beam size measured at cameras with standard deviation given by error bars; semi-transparent lines show envelopes of individual events; semi-transparent areas obtained by cross-fitting (described in 2.3); dotted vertical lines show the waist position; crosses denotes simulated values by MADX.

Comparison of the Three Beam Envelopes of the Three Different Sized Proton Beams
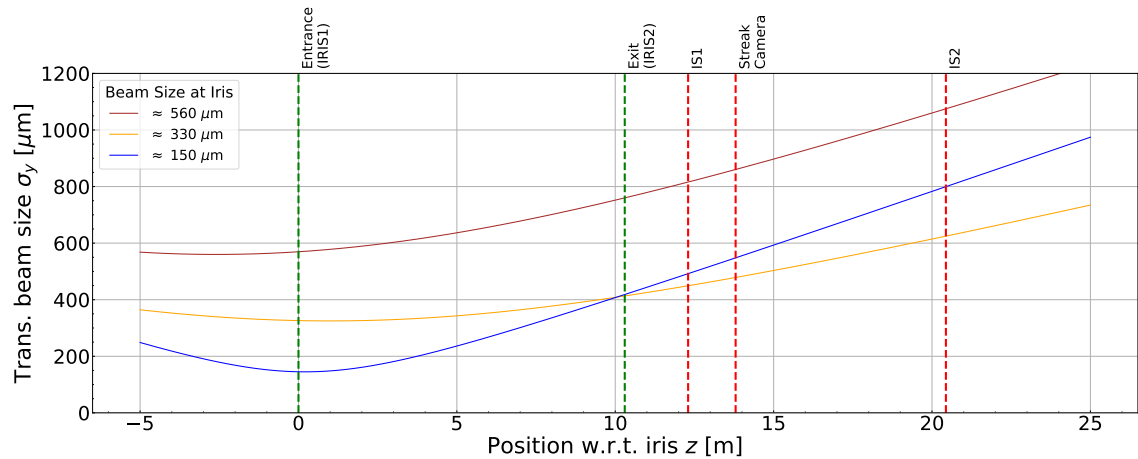

Figure A.3: Average beam envelopes reconstructed from the proton beam characterisation. The three beams of different transverse beam size that are considered in the plasma experiments are shown.

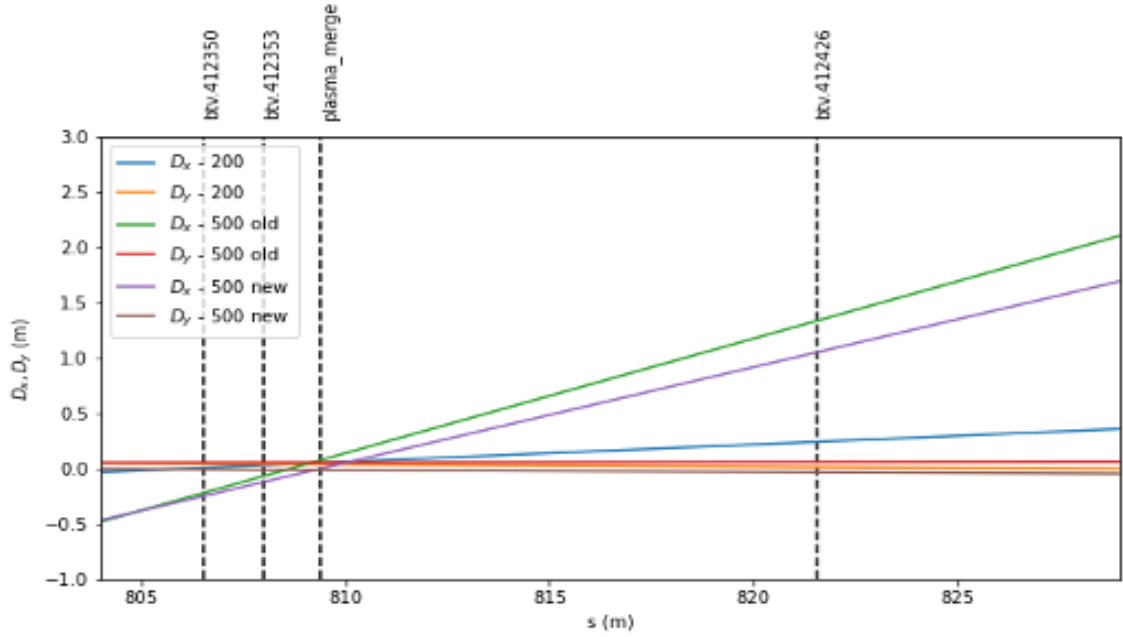## Comparison of the Dispersion of the Three Different Sized Proton Beams

Figure A.4: Dispersion along the x- and y-axis for the baseline design beam (200), for the $330\,\mu m$ large beam ($500\ old$) and the largest beam with $560\,\mu m$ transverse size ($500\ new$). Figure provided by *Dr Vittorio Bencini* in *private communication, 3rd Aug 2022*.

A.2   Simulations

Additional Convergence and Reproducibility Studies

Reproducibility Study for S-Set2
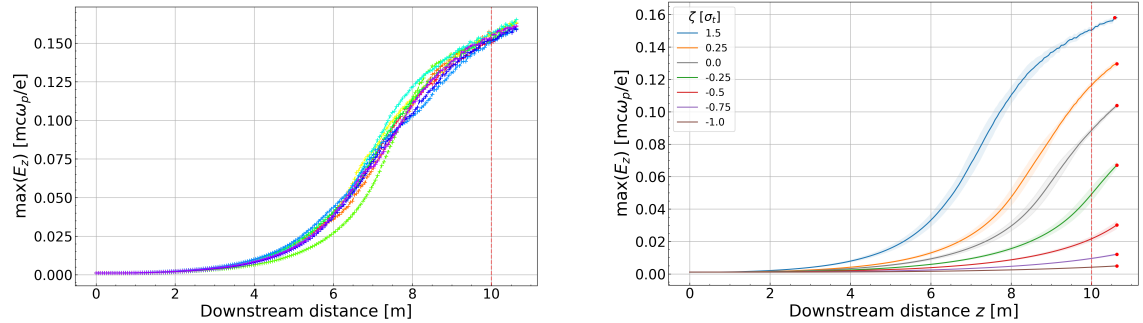
(a) Overall electrical field maxima in simulation window as a function of the downstream distance for nine identical simulations.

(b) Mean electrical field maxima in six slices of interest in the simulation window. Shaded envelopes represent the standard deviation over nine simulations. Slice position σ_t with respect to the center of the beam.

Figure A.5: Extended reproducibility study for a **S-Set 2** beam with $700\,\mu m$ transverse beam size at iris and number of macro-particles $N = 1 \times 10^8$.

Simulation Setup

Lcode Configurations

Units used in Lcode. Multiplying the output by the unit given brings the results back to the SI-standard. The units used are all related to the plasma frequency, see Eq.(3.17): ω_p the plasma angular frequency, k_p the plasma wave-number, c the speed of light, the electron mass m and the unperturbed plasma density n_0.

Group	Unit
Times	$\omega_p^{-1} = (k_p c)^{-1}$
Lengths	$c\omega_p^{-1} = k_p^{-1}$
Velocities	c
Momenta	mc
Angular momenta	$mc^2\omega_p^{-1}$
Masses	m
Number densities	n_0
Charge densities	en_0
Charges	e
Fields	$E_0 \equiv mc\omega_p/e$

Table A.1: Units used in Lcode.

Table A.2 shows general options used for Lcode simulations. An extensive description of all options is presented in [64].

Option	Value
rigid-beam [1]	no
beam-substepping-energy[2]	0
plasma-model	P [3]
plasma-particles-per-cell	10
plasma-profile	1 [4]
plasma-width	4.98
plasma-temperature	0
ion-model	y[5]
ion-mass	157000

Table A.2: General simulation options and settings used for the simulations in this work. The upper part concerns the charged particle beam (proton beam) and the lower the plasma handling. Descriptions in the footnote are taken from [64].

---

[1]Do not calculate beam evolution in time.

[2]The threshold of reducing the time-step for beam particles.

[3]f=fluid: The fluid model. It is the fastest one, but works only for the initially uniform plasma with immobile ions. Neither wave-breaking, nor near-wall plasma perturbations are allowed, P=newparticles: New kinetic model.

[4]1: uniform up to the walls, 2: stepwise uniform up to r_p, zero at $r > r_p$, 3: Gaussian, 4: arbitrary, 5: channel, 6: sub-channel.

[5]Y=mobile: Half of plasma macro-particles are single-charged mobile ions initially located at the same positions as plasma electrons, y=background: Ions are immobile background charge, n=absent: No ions, plasma electrons are initially at rest.

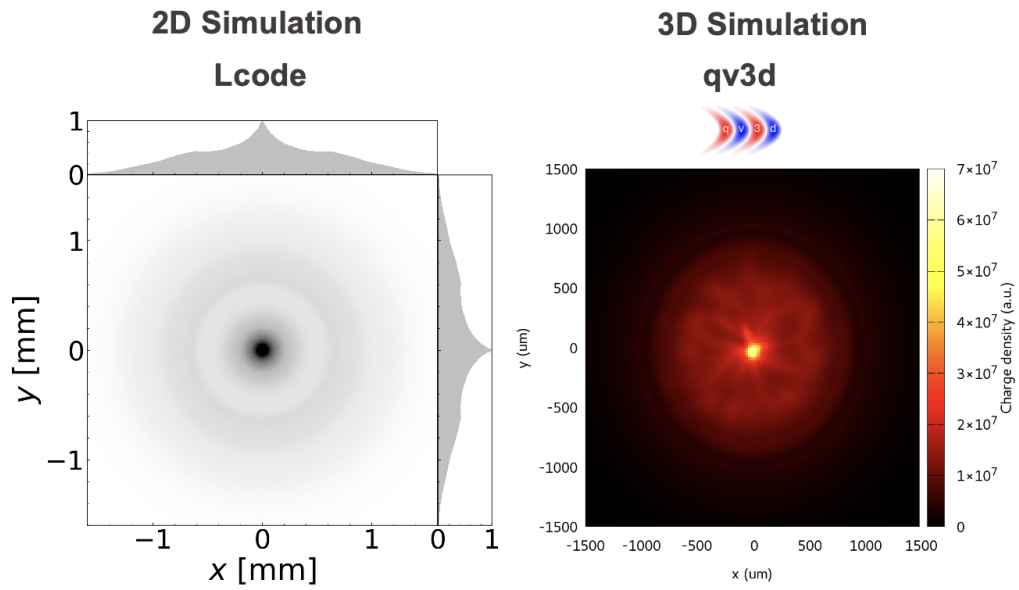## Proton Beam Projections in Simulations

Figure A.6: Additional results after submitting this thesis. Result of a 3D simulation with the code *qv3d* by *Dr John Farmer*. Post-processing and parameters space similar to the 2D case. Presented is a beam of $\sigma_{\perp,i} = 600\,\mu\text{m}$ with parameters according to **S-Set 3**. A spoke like structure appears in the 3D simulations. The outer-end of the spokes show some sort of ring also visible in the 2D simulations.

A.3 Plasma Experiment Results
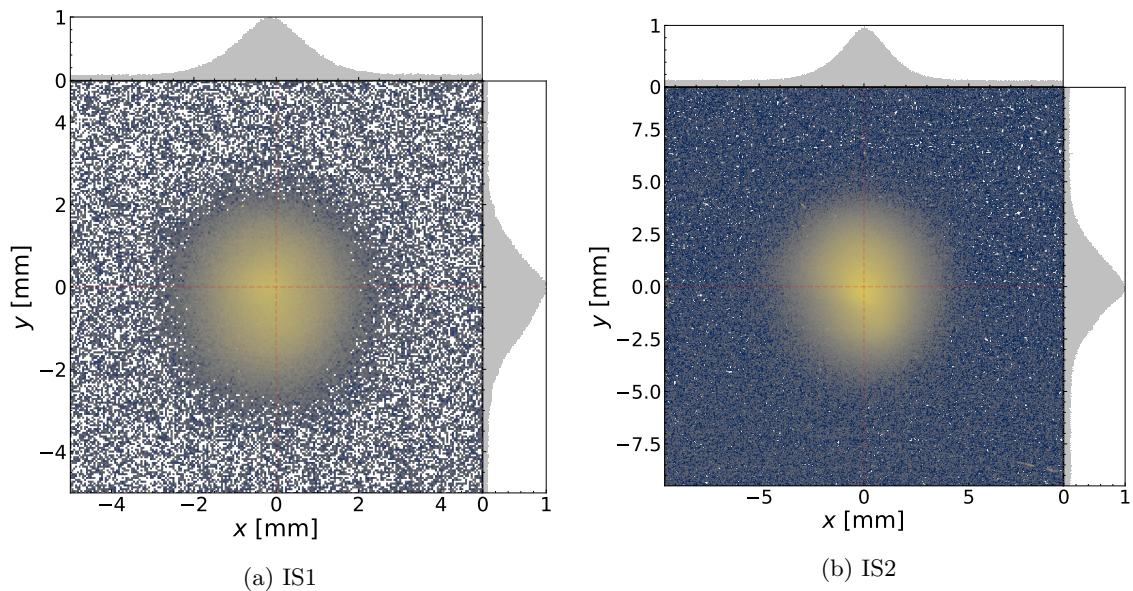
Single Event Seen by IS1 and IS2

(a) IS1

(b) IS2

Figure A.7: Single event image of the two image stations of a beam of width $560\,\mu\text{m}$ at the iris.

B Mathematics

B.1   Statistics

Linear Transformation

Assume an arbitrary distribution needs to be transformed by a linear function $g(x) = a + bx$ for $b > 0$. F_X denotes the cumulative distribution function for the original random variable X and F_Y for the random variable Y, then:

$$
\begin{aligned}
F_Y(y) = \mathbb{P}(Y \le y) &= \mathbb{P}(a + bX \le y) \\
&= \mathbb{P}\left(X \le \frac{y-a}{b} \right) \\
&= F_X\left(\frac{y-a}{b} \right)
\end{aligned}
\tag{B.1}
$$

The case $b < 0$ is similar but needs to be treated separately up to this point. Taking now the derivative to find the probability density function f_Y with $b \ne 0$:

$$
f_Y(y) = \frac{1}{|b|} f_X\left(\frac{y-a}{b} \right)
\tag{B.2}
$$

Following this procedure in the case of a normal distribution one finds that:

$$
\begin{aligned}
\mathbb{E}[Y] &= a + b\mathbb{E}[X] \\
\sigma_Y &= |b|\sigma_X
\end{aligned}
\tag{B.3}
$$

Where $\mathbb{E}$ denotes the expectation value which can be seen as the mean and σ the standard deviation.[81]

B.2   Gaussian Fitting

Basic Gaussian Function

The basic Gaussian function is defined as:

$$
H + Ae^{\frac{-(x-x_0)^2}{2\sigma^2}}
\tag{B.4}
$$

where H is the pedestal, A the amplitude, x_0 the mean and σ the standard deviation.

Scipy's Curve Fit Method

When fitting a Gaussian curve $g(x)$ to a discrete function $y_0 = f(x_0)$, it is sensible to choose the following initial parameters:

$$
\begin{aligned}
H &= \min(y) \\
A &= \max(y) \\
x_0 &= \frac{\sum_i x_i y_i}{\sum_i y_i} \\
\sigma &= \sqrt{\frac{\sum_i y_i (x_i - x_0)^2}{\sum_i y_i}}
\end{aligned}
\tag{B.5}
$$

where the transition to the common estimator of a Gaussian distribution can be made by considering y_i as a weight. Note that a pedestal $H \neq 0$ can heavily bias the mean and standard deviation. This is why it is not sufficient to determine these two parameters only with estimators.

B.3 Vector Formulas

$$
\nabla \wedge (\nabla \wedge \boldsymbol{a}) = \nabla(\nabla \cdot \boldsymbol{a}) - \nabla^2 a
\tag{B.6}
$$

$$
\nabla(\boldsymbol{a} \cdot \boldsymbol{b}) = (\boldsymbol{a} \cdot \nabla)\boldsymbol{b} + (\boldsymbol{b} \cdot \nabla)\boldsymbol{a} + \boldsymbol{a} \wedge (\nabla \wedge \boldsymbol{b}) + \boldsymbol{b} \wedge (\nabla \wedge \boldsymbol{a})
\tag{B.7}
$$

$$
\nabla \cdot (\boldsymbol{a} \wedge \boldsymbol{b}) = \boldsymbol{b} \cdot (\nabla \wedge \boldsymbol{a}) - \boldsymbol{a} \cdot (\nabla \wedge \boldsymbol{b})
\tag{B.8}
$$

$$
\nabla \wedge (\boldsymbol{a} \wedge \boldsymbol{b}) = \boldsymbol{a}(\nabla \cdot \boldsymbol{b}) - \boldsymbol{b}(\nabla \cdot \boldsymbol{a}) + (\boldsymbol{b} \cdot \nabla)\boldsymbol{a} - (\boldsymbol{a} \cdot \nabla)\boldsymbol{b}
\tag{B.9}
$$

B.4   List of Symbols

Definitions deviating from this table are noted in the text.

Symbol	Description
Basic symbols	
γ	Lorentz factor
β_{rel}, β	Relativistic beta factor
c	Speed of light
e	Elementary charge
m	Electron mass
m_b	Proton mass
Electromagnetism	
$\boldsymbol{E}$	Electric field
$\boldsymbol{B}$	Magnetic field
ρ	(Theoretical) charge density
$\boldsymbol{J}$	Current density
μ_0	Magnetic permeability of the vacuum
ε_0	Electric permittivity of the vacuum
Proton beam or bunch description	
z	Downstream position
$z_{x,0}$, $z_{y,0}$	Proton beam waist position
$\sigma_{x,0}$, $\sigma_{y,0}$	Transversal beam size at beam waist
$\sigma_{x,i}$, $\sigma_{y,i}$	Transversal beam size at beam iris
$\sigma_{\perp,i}$	Transversal beam size at beam iris if $\sigma_{x,i} = \sigma_{y,i}$
ς_x, ς_y	Beam divergence
ϵ_x, ϵ_y	Beam emittance
$\epsilon_{n,x}$, $\epsilon_{n,y}$	Normalised beam emittance
$\sigma_x(z)$, $\sigma_y(z)$	Beam size at downstream position z
$\beta_{x,0}$	Beta function at the beam waist
n_b	Beam density
σ_z	Bunch length
$\sigma_t = \sigma_z/c$	Bunch duration
Plasma physics	
ω_p	Plasma angular frequency
f_p	Plasma frequency
k_p	Plasma wave-number
λ_p	Plasma wavelength
n_0	Plasma (electron) density
n_{ion}	Plasma ion density
Coordinates on the scale of the bunch (laboratory frame)	
$\zeta = z/c - t$	Time on the timescale of the proton bunch (used in our results)
$\zeta = z - ct$	Position inside proton bunch (sometimes used in the theory)
Others	
ρ_{rad}	Radial density
P_R	Radial probability

Table B.1: Definition of symbols.

Bibliography

[1] E. Gschwendtner *et al.*, "Awake, the advanced proton driven plasma wakefield acceleration experiment at cern", *Nuclear Instruments and Methods in Physics Research, Section A: Accelerators, Spectrometers, Detectors and Associated Equipment*, vol. 829, pp. 76–82, Dec. 2015. DOI: 10.1016/j.nima.2016.02.026. [Online]. Available: http://arxiv.org/abs/1512.05498%20http://dx.doi.org/10.1016/j.nima.2016.02.026.

[2] A. Caldwell, K. Lotov, A. Pukhov, and F. Simon, "Proton-driven plasma-wakefield acceleration", *Nature Physics*, p. 24, 2009. DOI: 10.1038/NPHYS1248. [Online]. Available: www.nature.com/naturephysics.

[3] A. Ahuja *et al.*, "Acceleration of electrons in the plasma wakefield of a proton bunch", *Nature*, 2018. DOI: 10.1038/s41586-018-0485-4. [Online]. Available: https://doi.org/10.1038/s41586-018-0485-4.

[4] E. Gschwendtner *et al.*, "The awake run 2 programme and beyond", 2022.

[5] L. Verra *et al.*, "Controlled growth of the self-modulation of a relativistic proton bunch in plasma", *Physical Review Letters*, vol. 129, p. 024 802, 2 Jul. 2022, ISSN: 0031-9007. DOI: 10.1103/PhysRevLett.129.024802. [Online]. Available: https://journals.aps.org/prl/abstract/10.1103/PhysRevLett.129.024802.

[6] L. Verra, G. Z. della Porta, K. J. Moon, A. M. Bachmann, E. Gschwendtner, and P. Muggli, "Seeding of proton bunch self-modulation by an electron bunch in plasma", *47th EPS Conference on Plasma Physics, EPS 2021*, vol. 2021-June, pp. 745–748, Jun. 2021. DOI: 10.48550/arxiv.2106.12414. [Online]. Available: https://arxiv.org/abs/2106.12414v1.

[7] G. Zevi *et al.*, "Preparation for electron-seeding of proton bunch self-modulation in awake", *Proceedings of IPAC2021*, pp. 1761–1764, 2021. DOI: 10.18429/JACoW-IPAC2021-TUPAB160.

[8] E. Gschwendtner, D. Cooke, S. Doebert, S. Mazzoni, and J. Pucek, "Awake at clear (awake run 2)", CERN, Mar. 2021.

[9] "Facts and figures about the lhc | cern". (Jun. 2022), [Online]. Available: https://home.cern/resources/faqs/facts-and-figures-about-lhc.

[10] "Final budget of the organization for the sixty-seventh financial year", [Online]. Available: https://cds.cern.ch/record/2747877/files/English.pdf.

[11] "2019 cern electrical power consumption", 2020. [Online]. Available: https://en.web.cern.ch/sites/default/files/docs/ElectricityFlyer2019_v4.pdf.

[12] "Energy management | hse unit at cern". (Jun. 2022), [Online]. Available: https://hse.cern/content/energy-management.

[13] CMS-Collaboration, "Observation of a new boson at a mass of 125 gev with the cms experiment at the lhc", *Physics Letters B*, vol. 716, pp. 30–61, 1 Sep. 2012, ISSN: 0370-2693. DOI: 10.1016/J.PHYSLETB.2012.08.021.

[14] ATLAS-Collaboration, "Observation of a new particle in the search for the standard model higgs boson with the atlas detector at the lhc", *Phys.Lett.B*, vol. 716, pp. 1–29, 1 Sep. 2012, ISSN: 03702693. DOI: 10.1016/J.PHYSLETB.2012.08.020.

[15] T. R. S. A. of Sciences, "Press release: the nobel prize in physics 2013", 2013. [Online]. Available: www.ulb.ac.be/sciences/physth/people_FEnglert.html.

[16] "Facts and figures about the lhc | cern". (Jun. 2022), [Online]. Available: https://home.cern/resources/faqs/facts-and-figures-about-lhc.

[17] "The third run of the large hadron collider has successfully started | cern". (Jul. 2022), [Online]. Available: https://home.cern/news/news/cern/third-run-large-hadron-collider-has-successfully-started.

[18] R. Assmann *et al.*, "Proton-driven plasma wakefield acceleration: a path to the future of high-energy particle physics", *Plasma Physics and Controlled Fusion*, vol. 56, p. 084 013, 8 Aug. 2014, ISSN: 0741-3335. DOI: 10.1088/0741-3335/56/8/084013. [Online]. Available: https://iopscience.iop.org/article/10.1088/0741-3335/56/8/084013.

[19] S. Wyler, "Proton beam characterisation of the advanced wakefield experiment awake, specialistion work report", EPFL, Jan. 2022.

[20] G. I. P. Budker, "Cern symposium on high energy accelerators and pion physics : cern, geneva, switzerland 11 - 23 jun 1956", E. Regenstreif, Ed., CERN, Jun. 1956, pp. 68–75. DOI: 10.5170/CERN-1956-025. [Online]. Available: https://cds.cern.ch/record/107802.

[21] T. Tajima and J. M. Dawson, "Laser electron accelerator", *Physical Review Letters*, vol. 43, p. 267, 4 Jul. 1979, ISSN: 00319007. DOI: 10.1103/PhysRevLett.43.267. [Online]. Available: https://journals.aps.org/prl/abstract/10.1103/PhysRevLett.43.267.

[22] R. D. Ruth, A. W. Chao, P. L. Morton, and P. B. Wilson, "A plasma wake field accelerator?", *Particle Accelerators*, vol. 17, pp. 171–189, 1985.

[23] I. Blumenfeld *et al.*, "Energy doubling of 42 gev electrons in a metre-scale plasma wakefield accelerator", *Nature 2006 445:7129*, vol. 445, pp. 741–744, 7129 Feb. 2007, ISSN: 1476-4687. DOI: 10.1038/nature05538. [Online]. Available: https://www.nature.com/articles/nature05538.

[24] N. Kumar, A. Pukhov, and K. Lotov, "Self-modulation instability of a long proton bunch in plasmas", *Physical Review Letters*, vol. 104, p. 255 003, 25 Jun. 2010, ISSN: 00319007. DOI: 10.1103/PHYSREVLETT.104.255003/FIGURES/4/MEDIUM. [Online]. Available: https://journals.aps.org/prl/abstract/10.1103/PhysRevLett.104.255003.

[25] "Cern neutrinos to gran sasso | cern". (Jun. 2022), [Online]. Available: https://home.cern/science/accelerators/cern-neutrinos-gran-sasso.

[26] J. S. Schmidt *et al.*, "Awake proton beam commissioning", IPAC2017, 2017, ISBN: 9783954501823.

[27] E. Gschwendtner *et al.*, "Awake, the advanced proton driven plasma wakefield acceleration experiment at cern", *Nuclear Instruments and Methods in Physics Research Section A: Accelerators, Spectrometers, Detectors and Associated Equipment*, vol. 829, pp. 76–82, Sep. 2016, ISSN: 0168-9002. DOI: 10.1016/J.NIMA.2016.02.026.

[28] K. Pepitone *et al.*, "The electron accelerators for the awake experiment at cern— baseline and future developments", *Nuclear Inst. and Methods in Physics Research, A*, vol. 909, pp. 102–106, 2018. DOI: 10.1016/j.nima.2018.02.044. [Online]. Available: https://doi.org/10.1016/j.nima.2018.02.044.

[29] P. Muggli *et al.*, "Awake readiness for the study of the seeded self-modulation of a 400 gev proton bunch the awake collaboration", 2017.

[30] K. V. Lotov *et al.*, "Electron trapping and acceleration by the plasma wakefield of a self-modulating proton beam", *Physics of Plasmas*, vol. 21, p. 123 116, 12 Dec. 2014, ISSN: 1070-664X. DOI: 10.1063/1.4904365. [Online]. Available: https://aip.scitation.org/doi/abs/10.1063/1.4904365.

[31] A. A. Gorn, P. V. Tuev, A. V. Petrenko, A. P. Sosedkin, and K. V. Lotov, "Response of narrow cylindrical plasmas to dense charged particle beams", *Physics of Plasmas*, vol. 25, p. 063 108, 6 Jun. 2018, ISSN: 1070-664X. DOI: 10.1063/1.5039803. [Online]. Available: https://aip.scitation.org/doi/abs/10.1063/1.5039803.

[32] C. B. Schroeder, C. Benedetti, E. Esarey, F. J. Grüner, and W. P. Leemans, "Growth and phase velocity of self-modulated beam-driven plasma waves", *Physical Review Letters*, vol. 107, p. 145 002, 14 Sep. 2011, ISSN: 00319007. DOI: 10.1103/PHYSREVLETT.107.145002/FIGURES/2/MEDIUM. [Online]. Available: https://journals.aps.org/prl/abstract/10.1103/PhysRevLett.107.145002.

[33] A. Pukhov *et al.*, "Phase velocity and particle injection in a self-modulated proton-driven plasma wakefield accelerator", *Physical Review Letters*, vol. 107, p. 145 003, 14 Sep. 2011, ISSN: 00319007. DOI: 10.1103/PHYSREVLETT.107.145003/FIGURES/4/MEDIUM. [Online]. Available: https://journals.aps.org/prl/abstract/10.1103/PhysRevLett.107.145003.

[34] M. Bergamaschi, P. Muggli, J. Pucek, R. Speroni, and W. Design, "Vapor source update for run2 awake collaboration meeting", CERN, MPP Munich, Sep. 2021.

[35] F. Batsch *et al.*, "Transition between instability and seeded self-modulation of a relativistic particle bunch in plasma", *Physical Review Letters*, vol. 126, p. 164 802, 16 Apr. 2021, ISSN: 10797114. DOI: 10.1103/PHYSREVLETT.126.164802/FIGURES/4/MEDIUM. [Online]. Available: https://journals.aps.org/prl/abstract/10.1103/PhysRevLett.126.164802.

[36] V. Hafych *et al.*, "Analysis of proton bunch parameters in the awake experiment", Sep. 2021. [Online]. Available: https://arxiv.org/abs/2109.12893v1.

[37] J. S. Schmidt *et al.*, "Commissioning preparation of the awake proton beam line", IPAC, 2016, ISBN: 9783954501472. DOI: 10.1016/j.nima.2016.02.026. [Online]. Available: http://www.JACoW.org.

[38] S. Mazzoni *et al.*, "Beam instrumentation developments for the advanced proton driven plasma wakefield acceleration experi-ment at cern", IPAC, 2017, ISBN: 9783954501823.

[39] V. L. Ginzburg and I. M. Frank, "Radiation of a uniformly moving electron due to its transition from one medium into another", *J. Phys. (USSR)*, vol. 9, pp. 353–362, 1945.

[40] J. D. Jackson, *J.D.Jackson - Classical Electrodynamics (1999)*, 3rd ed. John Wiley and Sons, Inc, ISBN: 0-471-30932-X.

[41] V. L. Ginzburg, "Transition radiation and transition scattering", *Physica Scripta*, vol. 2, pp. 182–191, 1 1982.

[42] M. Bergamaschi, "Development of a combined transition and diffraction radiation station for non-invasive beam size monitoring on linear accelerators", 2018.

[43] S. Gundacker, R. M. Turtos, E. Auffray, and P. Lecoq, "Precise rise and decay time measurements of inorganic scintillators by means of x-ray and 511 kev excitation", *Nuclear Inst. and Methods in Physics Research*, vol. 891, pp. 42–52, 2018. DOI: 10.1016/j.nima.2018.02.074. [Online]. Available: https://doi.org/10.1016/j.nima.2018.02.074.

[44] S. Burger, M. Turner, B. Biskup, S. Mazzoni, and G. Switzerland, "Jacow : scintillation and otr screen characterization with a 440 gev/c proton beam in air at the cern hiradmat facility", MOPG78, 2017. DOI: 10.18429/JACOW-IBIC2016-MOPG78. [Online]. Available: https://cds.cern.ch/record/2313941.

[45] M. Turner, B. Biskup, S. Burger, E. Gschwendtner, S. Mazzoni, and A. Petrenko, "The two-screen measurement setup to indirectly measure proton beam self-modulation in awake", *Nuclear Instruments and Methods in Physics Research Section A: Accelerators, Spectrometers, Detectors and Associated Equipment*, vol. 854, pp. 100–106, May 2017, ISSN: 0168-9002. DOI: 10.1016/J.NIMA.2017.02.064.

[46] M. Turner, V. Clerc, I. Gorgisyan, E. Gschwendtner, S. Mazzoni, and A. Petrenko, "Upgrade of the two-screen measurement setup in the awake experiment", *Journal of Physics: Conference Series*, vol. 874, 1 Jul. 2017, ISSN: 17426596. DOI: 10.1088/1742-6596/874/1/012031.

[47] "Eos open storage at cern". (Jun. 2022), [Online]. Available: https://eos-web.web.cern.ch/eos-web/.

[48] S. A. and G. M. J. E., "Soothing and differentiation of data by simplified least squares procedures", *Anal. Chem*, vol. 36, pp. 1627–1639, 1964.

[49] R. W. Schafer, "What is a savitzky-golay filter?", *IEEE Signal Processing Magazine*, vol. 28, pp. 111–117, 4 2011, ISSN: 10535888. DOI: 10.1109/MSP.2011.941097.

[50] J. Penedones, "Classical electrodynamics, lecture notes (phys-324)", EPFL, 2019, pp. 1–4.

[51] H. Wiedemann, *Partide Accelerator Physics I, Basic Principles and Linear Beam Dynamics*, Fourth Edition. Springer, 2003, pp. 37–38, ISBN: 978-3-540-00672-5. DOI: 10.1007/978-3-662-05034-7. [Online]. Available: http://www.springer.de/phys/.

[52] S. Alberti, "Introduction à la physique des plasmas, lecture notes (phys-325)", EPFL, PH, SPC, 2017. [Online]. Available: https://edu.epfl.ch/coursebook/fr/introduction-a-la-physique-des-plasmas-PHYS-325.

[53] F. F. Chen, "Introduction to plasma physics and controlled fusion", *Introduction to Plasma Physics and Controlled Fusion*, 2016. DOI: 10.1007/978-3-319-22309-4.

[54] K. V. Lotov and P. V. Tuev, "Plasma wakefield acceleration beyond the dephasing limit with 400 gev proton driver", *Plasma Phys.Control.Fusion*, vol. 63, 12 Dec. 2021, ISSN: 13616587. DOI: [10.1088/1361-6587/AC349A](10.1088/1361-6587/AC349A).

[55] K. Moon and M. Chung, "Numerical studies of self modulation instability in the beam-driven plasma wakefield experiments*", 2016.

[56] D. H. Whittum, "Transverse two-stream instability of a beam with a bennett profile", *Physics of Plasmas*, vol. 4, p. 1154, 4 Sep. 1998, ISSN: 1070-664X. DOI: [10.1063/1.872202](10.1063/1.872202). [Online]. Available: https://aip.scitation.org/doi/abs/10.1063/1.872202.

[57] J. Vieira, W. B. Mori, and P. Muggli, "Hosing instability suppression in self-modulated plasma wakefields", *Physical Review Letters*, vol. 112, p. 205 001, 20 May 2014, ISSN: 10797114. DOI: 10.1103/PHYSREVLETT.112.205001/FIGURES/3/MEDIUM. [Online]. Available: https://journals.aps.org/prl/abstract/10.1103/PhysRevLett.112.205001.

[58] P. Chen, K. Oide, A. M. Sessler, and S. S. Yu, "Plasma-based adiabatic focusing", *Physical Review Letters*, vol. 64, 11 1990.

[59] A. Petrenko, "Awake simulations: codes, computing resources, physics problems", 2018.

[60] A. Sosedkin and K. Lotov, "Lcode: a parallel quasistatic code for computationally heavy problems of plasma wakefield acceleration", Nov. 2015. DOI: 10.1016/j.nima.2015.12.032. [Online]. Available: http://arxiv.org/abs/1511.04193%20http://dx.doi.org/10.1016/j.nima.2015.12.032.

[61] A. Pukhov, "Particle-in-cell codes for plasma-based particle acceleration", *CERN Yellow Reports*, vol. 1, pp. 181–181, Feb. 2016, ISSN: 0007-8328. DOI: 10.5170/CERN-2016-001.181. [Online]. Available: https://e-publishing.cern.ch/index.php/CYR/article/view/220.

[62] ——, "Three-dimensional electromagnetic relativistic particle-in-cell code vlpl (virtual laser plasma lab)", *Journal of Plasma Physics*, vol. 61, pp. 425–433, 3 Apr. 1999, ISSN: 1469-7807. DOI: [10.1017/S0022377899007515](10.1017/S0022377899007515). [Online]. Available: https://www.cambridge.org/core/journals/journal-of-plasma-physics/article/abs/threedimensional-electromagnetic-relativistic-particleincell-code-vlpl-virtual-laser-plasma-lab/7FBA476D599E2F19DFEA3F0F2F84FFAB.

[63] J. Fl, L. D. Landau, and E. M. Lifshitz, *Landau Lifshitz The Classical Theory of Fields*, 3rd ed. PERGAMON PRESS.

[64] K. V. Lotov and A. P. Sosedkin, "Lcode user manual", Budker Institute of Nuclear Physics of SB RAS, 2022. [Online]. Available: https://lcode.info/site-files/manual.pdf.

[65] K. V. Lotov, "Blowout regimes of plasma wakefield acceleration", *Physical Review E - Statistical Physics, Plasmas, Fluids, and Related Interdisciplinary Topics*, vol. 69, p. 13, 4 2004, ISSN: 1063651X. DOI: 10.1103/PHYSREVE.69.046405.

[66] K. V. Lotov, A. Pukhov, and A. Caldwell, "Effect of plasma inhomogeneity on plasma wakefield acceleration driven by long bunches", *Physics of Plasmas*, vol. 20, 1 Jan. 2013, ISSN: 1070664X. DOI: [10.1063/1.4773905](10.1063/1.4773905).

[67] J. Buon, "Beam phase space and emittance", Feb. 1992. DOI: 10.5170/CERN-1994-001.89. [Online]. Available: https://cds.cern.ch/record/242313.

[68]   *Guide to Streak Cameras.* HAMAMATSU PHOTONICS K.K., Systems Division, 2008.

[69]   K. Rieger, A. Caldwell, O. Reimann, and P. Muggli, "Ghz modulation detection using a streak camera: suitability of streak cameras in the awake experiment", *Review of Scientific Instruments*, vol. 88, p. 025 110, 2 Feb. 2017, ISSN: 0034-6748. DOI: 10.1063/1.4975380. [Online]. Available: https://aip.scitation.org/doi/abs/10.1063/1.4975380.

[70]   F. Lindsten, "A remark on zero-padding for increased frequency resolution", 2010.

[71]   "Understanding ffts and windowing overview", National Instruments. [Online]. Available: https://download.ni.com/evaluation/pxi/Understanding%5C%20FFTs%5C%20and%5C%20Windowing.pdf.

[72]   R. B. Blackman and J. W. Tukey, "The measurement of power spectra from the point of view of communications engineering — part i", *Bell System Technical Journal*, vol. 37, pp. 185–282, 1 1958, ISSN: 15387305. DOI: 10.1002/J.1538-7305.1958.TB03874.X.

[73]   A.-M. Bachmann, "Self-modulation development of a proton bunch in plasma", Technical University of Munich, 2021, pp. 72–75. [Online]. Available: https://mediatum.ub.tum.de/doc/1595621/1595621.pdf.

[74]   P. I. M. Guzmán *et al.*, "Simulation and experimental study of proton bunch self-modulation in plasma with linear density gradients", *Physical Review Accelerators and Beams*, vol. 24, p. 101 301, 10 Oct. 2021, ISSN: 24699888. DOI: 10.1103/PHYSREVACCELBEAMS.24.101301/FIGURES/11/MEDIUM. [Online]. Available: https://journals.aps.org/prab/abstract/10.1103/PhysRevAccelBeams.24.101301.

[75]   J. Chappell *et al.*, "Experimental study of extended timescale dynamics of a plasma wakefield driven by a self-modulated proton bunch", *Physical Review Accelerators and Beams*, vol. 24, p. 011 301, 1 Jan. 2021, ISSN: 24699888. DOI: 10.1103/PHYSREVACCELBEAMS.24.011301/FIGURES/9/MEDIUM. [Online]. Available: https://journals.aps.org/prab/abstract/10.1103/PhysRevAccelBeams.24.011301.

[76]   F. Braunmüller *et al.*, "Proton bunch self-modulation in plasma with density gradient", *Physical Review Letters*, vol. 125, p. 264 801, 26 Dec. 2020, ISSN: 10797114. DOI: 10.1103/PHYSREVLETT.125.264801/FIGURES/4/MEDIUM. [Online]. Available: https://journals.aps.org/prl/abstract/10.1103/PhysRevLett.125.264801.

[77]   M. Turner *et al.*, "Experimental study of wakefields driven by a self-modulating proton bunch in plasma", *Physical Review Accelerators and Beams*, vol. 23, p. 081 302, 8 Aug. 2020, ISSN: 24699888. DOI: 10.1103/PHYSREVACCELBEAMS.23.081302/FIGURES/4/MEDIUM. [Online]. Available: https://journals.aps.org/prab/abstract/10.1103/PhysRevAccelBeams.23.081302.

[78]   E. Adli *et al.*, "Experimental observation of proton bunch modulation in a plasma at varying plasma densities", *Physical Review Letters*, vol. 122, p. 054 802, 5 Feb. 2019, ISSN: 10797114. DOI: 10.1103/PHYSREVLETT.122.054802/FIGURES/4/MEDIUM. [Online]. Available: https://journals.aps.org/prl/abstract/10.1103/PhysRevLett.122.054802.

[79]   B. Widom, *The liquid state.* Cambridge University Press, Jun. 2012, pp. 101–132. DOI: 10.1017/cbo9780511815836.008.

[80] B. Widom, *The non-ideal gas.* Cambridge University Press, Jun. 2012, pp. 81–100. DOI: 10.1017/cbo9780511815836.007.

[81] L. Meier, M. Maathuis, H. Künsch, P. Bühlmann, and M. Kalisch, "Statistik und wahrscheinlichkeitsrechnung", ETHZ.